Study of the electromagnetic interactions between radar equipment under integrated and compact mature : design and validation

Thtreswar Beeharry

Université Paris Nanterre
200 av. de la République
92001 Nanterre Cedex
www.parisnanterre.fr

Membre de l'université Paris Lumières

École doctorale 139 :
Connaissance, langage, modélisation
Laboratoire Energétique Mécanique Electromagnétisme

Thtreswar Beeharry

Study of electromagnetic interactions between radar equipment under integrated and compact mature: Design and validation.

Thèse présentée et soutenue publiquement le 31/01/2019
en vue de l'obtention du doctorat de Electronique, optronique et systèmes de l'Université Paris Nanterre
sous la direction de Mme Habiba Ouslimani (Université Paris Nanterre)

Jury * **:**

Rapporteur : Présidente de jury:	Madame Damienne Bajon	Professeur, ISAE-SUPAERO
Rapporteur :	Mr Jean-Marc Ribero	Professeur, Université de Nice-Sophia Antipolis
Examinateur :	Mr Philippe Pouliguen	HDR, Directeur Scientifique DGA/DS/MRIS
Examinateur :	Pierre Sabouroux	Maitre de conférences, HDR, Aix Marseille-Institut Fresnel
Examinateur:	Kamardine Selemani	Docteur, Constructions Mécaniques de Normandie
Examinateur:	David Lautru	Professeur, Université Paris Nanterre
Directrice de thèse:	Habiba Ouslimani	Professeur, Université Paris Nanterre

Acknowledgements

I would like to thank all poeple who contributed in some way to achieve the works described in this thesis. First of all, I would like to thank professor Habiba Ouslimani, Director of the thesis, who has been more than a mentor and a supervisor for me during the 3 years of hard work. Apart from trusting me and giving me the opportunity to work with the Electromagnetism group of LEME, she gave me intellectual freedom in my work, always supporting my attendance to conferences and always ready to give me new challenges and ideas of research.

Secondly, I would like to thank our industrial partner Constructions Mécaniques de Normandie (CMN) who put their faith on our research group. I am grateful to all members of Systems departement including Kamardine, Selemani Sami Bellez and Stéphanie Thérache of CMN for welcoming me in their group.

I would also like to thank to Riad Yiahiaoui of Howard University, USA, a friend and previous researcher of the Electromagnetism group of LEME who helped me a lot during the first year of the thesis.

I would like to exrpress my gratitude to professor Sergei Tetryakov, for allowing me to have a research visit with his research group at the Department of Electronics and Nanoengineering of Aalto University, Finland. Our work on cylindrcal absorbers would not have been possble without him and Ana Diaz Rubio, Viktar Asadchy, researchers of Department of Electronics and Nanoengineering of Aalto University and Costas Valagiannopoulos, associate professor at Nazarbayev University, Kazakhstan.

Finally, I would like to acknowledge friends and family who supported me during my time thesis. First and foremost I would like to thank my Mother, Krishnachandanee Beeharry, my father, Motilal Beeharry, without whom nothing would have been possible. Thank you for your sacrifices and letting me leave Mauritius for my studies mom and dad. My deepest love to my two sisters Omuntee and Reena. I would like to thank my uncle Roy Ramphul for giving me the opportunity to come to Paris for my studies. Finally, a special thank to my love, Marine who has been supporting me during the 3 years without whom everything would have been very difficult.

Contents

List of Figures

List of Tables

Abbreviations

EW	**E**lectromagnetic **W**ave
EMC	**E**lectromagnetic **C**ompability
LPI	**L**ow **P**robability **I**ntercept
MM	**M**etamaterial
FSS	**F**requency **S**elective **S**urfaces
TLM	**T**ransmission **L**ine **M**odel
RCS	**R**adar **C**ross **S**ection
EMI	**E**lectromagnetic **I**nterference
TE	**T**ransverse **E**lectric *Throughout the thesis we consider a plane wave with E-field along y axis and H-field along x axis for TE mode.*
TM	**T**ransverse **M**agnetic *Throughout the thesis we consider a plane wave with E-field along x axis and H-field along y axis for TM mode.*
UUSR	**U**nderligned **U** **S**hape **R**esonator
HMSR	**H**alf **M**oon **S**hape **R**esonator
RSR	**R**ing **S**hape **R**esonator
RAM	**R**adar **A**bsorbing **M**aterial

Dedicated to

my parents
Motilal & Krischnachandanee BEEHARRY

Chapter 1

INTRODUCTION

1.1 Context

The works presented in this thesis is a fruit of 3 years of research on how to reduce electromagnetic interference in radomes of military vessels. The company, Constructions Mécaniques de Normandie (CMN) and the University of Paris Nanterre (UPN) have decided to put their respective skills together in the aim of reducing interference in radomes. CMN is a shipyard Company and has built more than 700 highly sophisticated military and civil vessels in aluminium, steel and advanced composite materials. The Electromagnetism pole of the LEME laboratory of UPN has a huge experience in R&D in metamaterials, antennas, electromagnetic absorbers and surface waves.

1.2 Motivation

Modern military ships are nowadays heavily equipped with antennas and radars dedicated to communication and combat systems. As a result, the arrangement and positioning of antennas and radars are difficult from an Electromagnetic Waves (EW) propagation point of view. Can appear problems of shadow zones, mismatch of antennas with their generator, strong values of radar signature and so on. All these are in fact Electromagnetic Compatibility (EMC) problems. The radomes of ships are the seat of all these phenomena. The experience of CMN, and actual needs suggest that the study of EMC problems inside radomes of military vessels and broadband devices for defense applications in general are urgent. Due to these needs, CMN has partnered Paris Nanterre UPN through the

National Research and Technology Association (ANRT) to build this doctoral program. This thesis aims to firstly, identify, the antennas, radars and regions that are affected by EMC problems and to identify the sources. In a second time the possible solutions will be discussed and put in place. Figure 1.1 is taken as an example depicting the different regions of a vessel where antennas and radars are positioned.

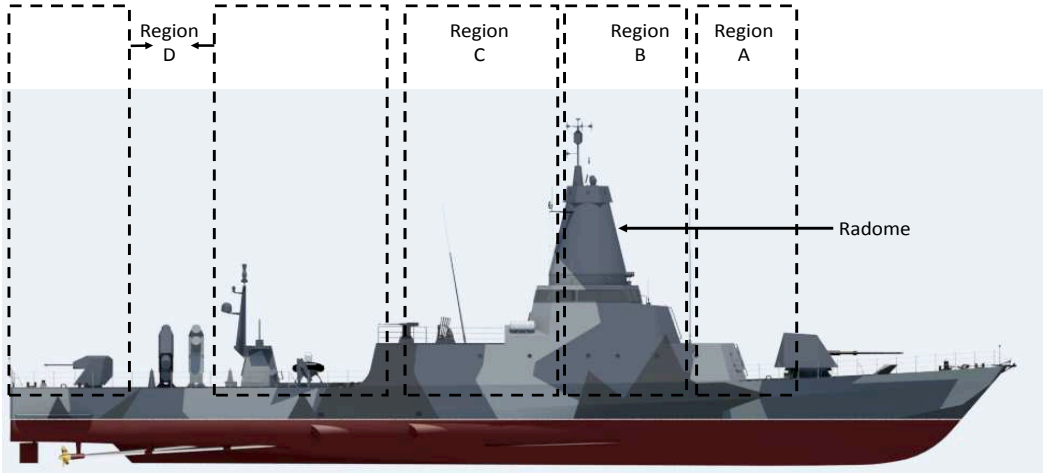

FIGURE 1.1: Profile view of the Combattante FS56. Regions A, B, C and D are regions where antennas and radars are placed.

The tables below are the lists of different antennas and radars placed in these regions and their respective frequency ranges.

Antenna or Radar	**Frequency range**
HF COM Rx Whip 0.65 m	1.6 - 30 MHz
TV Antenna Mark 32	0.1 - 2.5 MHz and 40 - 860 MHz
Satcom Fleet Braodband 500	1.625 - 1.66 GHz
RESM Thales Vigile LW	2 - 20 GHz

TABLE 1.1: Antennas and radars placed in Region A.

Antenna or Radar	**Frequency range**
HF COM Tx/Rx Whip 8m	1.6 - 30 MHz
VHF AIS Saab R5 Solid	162 MHz

TABLE 1.2: Antennas and radars placed in Region B.

Antenna or Radar	**Frequency range**
Navigation Radar 6ft	9.38 - 9.44 GHz
VARIANT 2D Surveillance radar + IFF	1.03 - 1.09 GHz
VHF GMDSS Tx/Rx	156 MHz
IFF Transponder	1.09 GHz
CESM Thales Altesse	Confidential
RESM Thales Vigile LW	Confidential
Inmarsat mini-C GMDSS	1.6 MHz
CESM AIS VHF	162 MHz

TABLE 1.3: Antennas and radars placed in Region C.

Antenna or Radar	**Frequency range**
VHF GMDSS Rx	156 MHz
DGPS	1.6 MHz
GPS AIS	161.975 MHz
HF GMDSS Tx/Rx Whip 8m	1.6 - 30 MHz
HF GMDSS Rx Whip 5m	1.6 - 30 MHz
VHF PR4G	30 - 88 MHz

TABLE 1.4: Antennas and radars placed in Region D.

Tables 1.1-1.4 show that military vessels can contain communication devices working in large frequency range. In this thesis, we will study EMC problems inside radomes only (Region B). A radome is an impermeable structure, having more or less spherical shape, which is put around a radar to protect it from bad weather and also not make the orientation of the antennas and radars visible. Various materials can be used for construction; for example rigid radomes are most often made of fiberglass, and others which are flexible are made of treated fabrics such as polytetrafluoroethylene. In most cases, radomes must be electromagnetically transparent and are patented (therefore, not much is known about the materials that have been used). Radomes are not only used for ground radars but also on ships and aircraft. Their shape can therefore vary according to use, especially on aircraft where they must have an aerodynamic shape. Figure 1.2 is a simple representation of a radome inside which different antennas and radars placed.

The metallic ducts which is part of the radome reflects back EW towards its emitter antenna or radar. In what follows, the effects of this phenomenon is discussed using two examples that have been studied by our industrial partner, CMN.

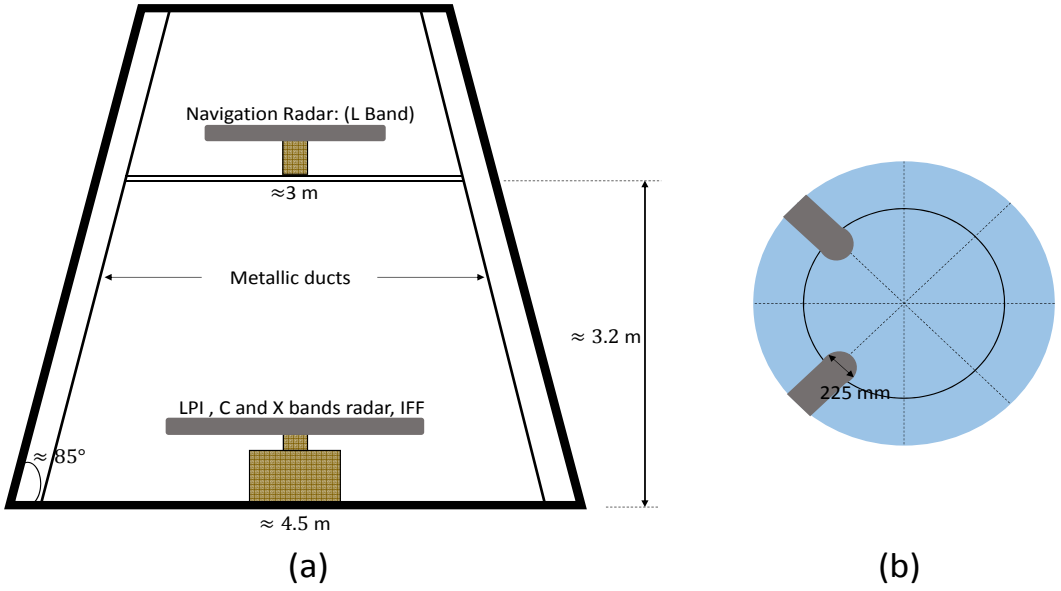

FIGURE 1.2: Profile view of the representation of a radome. Top view of the radome. Some approximate dimensions are also given.

1.2.1 Performance of the LPI inside a radome in the presence of metallic ducts

The Low Probability Intercept (LPI) is an antenna that operates at very low power. As a result, its detection sensitivity is extremely low. The presence of a radome around the LPI can cause a reflection of the signal that desensitizes the antenna. Such antennas have a power limit of reflection that they can accept. The performance of the LPI inside a radome on the 9.9 GHz - 10.4 GHz band is studied.

The desensitization of the LPI is intimately related to the self-coupling factor of the LPI, that is, the ratio between received signal (reflection caused by the radome and the metallic ducts) and the transmitted power by the LPI. Figure 1.3 depicts the coupling simulation results when the LPI points forward and when it points towards the metallic ducts for elevations until 10°. The detailed values of the coupling are not given as they are confidential. The simulations have been performed using Ship EDF software.

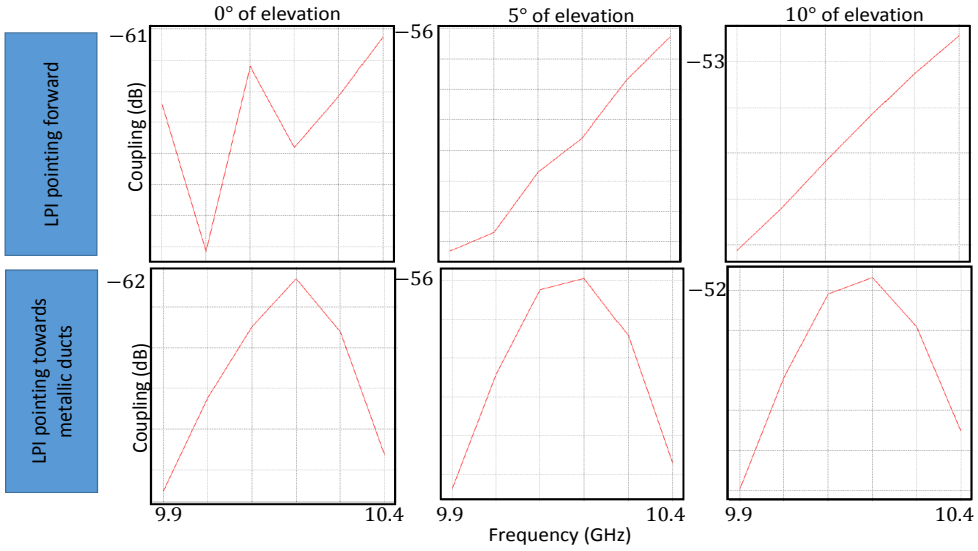

FIGURE 1.3: Self coupling of the LPI when it points forward and when it points towards the metallic ducts. Simulations have been done for 0°, 5° and 10° of elevations.

When the LPI points in the forward direction, for an elevation of 0°, the worst self coupling is of -61.8 dB in the frequency range of 9.9 - 10.4 GHz. The worst self coupling for 5° is of -56.7 dB and -52.7 dB for 10°.

Similarly, when the LPI points in the forward direction, for an elevation of 0°, the worst self coupling is of -62.2 dB in the frequency range of 9.9 - 10.4 GHz. The worst self coupling for 5° is of -56 dB and -51.8 dB for 10°.

Table 1.5 is a summary of the simulations performed. The level of self coupling depending on different configurations, as well as the necessary level for the proper functioning of the LPI are shown.

Max. allowed coupling for well functioning of different modes (dB)				Min. Coupling provoking saturation of LPI (dB)		
Full power, high resolution	Full power, low resolution	Medium power, high resolution	Medium power, low resolution	Full power	Medium power	Low power
-69	-57	-63	-51	-51	-44	-37

TABLE 1.5: Maximum allowed coupling for well functioning of different modes and minimum coupling that provokes the saturation of the LPI.

In the presented scenario, by taking into account the different maximum coupling for elevations until 10°, the LPI can operate in Medium Power, low Resolution Mode. For this mode, studies have shown that the path loss of the LPI is of 55.2% (in all directions). Thus we have shown that reflections can indirectly cause path loss of the LPI.

1.2.2 Performance of the IFF inside a radome in the presence of metallic ducts

The IFF radar is a used for identification based on a system of question/answer system. Its functioning being complex and results being very confidential, some simple simulation results are given in order to have an idea of the effects of metallic ducts. For this case, simulations have been performed when the radar is pointing towards 180° (no metallic duct) and 135° (presence of metallic duct. This scenario is illustrated in Figure 1.4 .

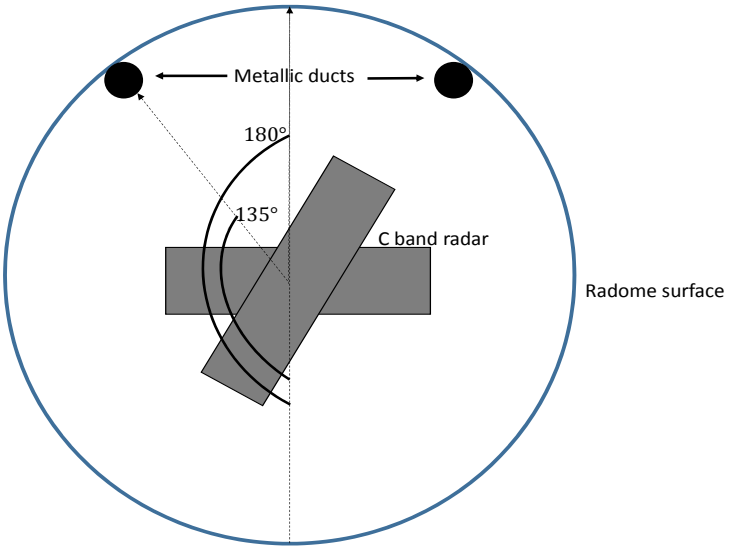

FIGURE 1.4: Illustration of the IFF radar inside the radome in the presence of the metallic ducts.

Three different scenarios exist in the identification system. First is 'Must' respond, second is 'May' respond and the third is 'Not allowed' to respond. The IFF uses to antennas and the selection of the different scenarios are made by making the subtraction of the gain of the two antennas. According to the constructor and some standards, some levels are fixed corresponding to the three cases. Due to confidentiality, the detailed values are not given but an example is given in Figure 1.5. In Figure 1.5 , the subtraction of the gains of the two antennas are plotted with respect to the azimuth angle.

Without entering in detailed observations, the most important observation that can be made is that when the radar points towards the metallic duct, some lobes, having a value which is more than the 'May respond' level, are found around 220°. This can be due to the side lobes of the antenna pointing towards the second metallic duct and also because of diffraction of the EW from the first to the second metallic duct. This case can lead to misinterpretations and detection of wrong targets as shown Figure 1.6.

In some cases, if one target is found at 135° and the another target is found at 220°, the position of the target found at 220° can be misinterpreted to the one found at 135°. These results show that refelctions can cause detection of wrong targets.

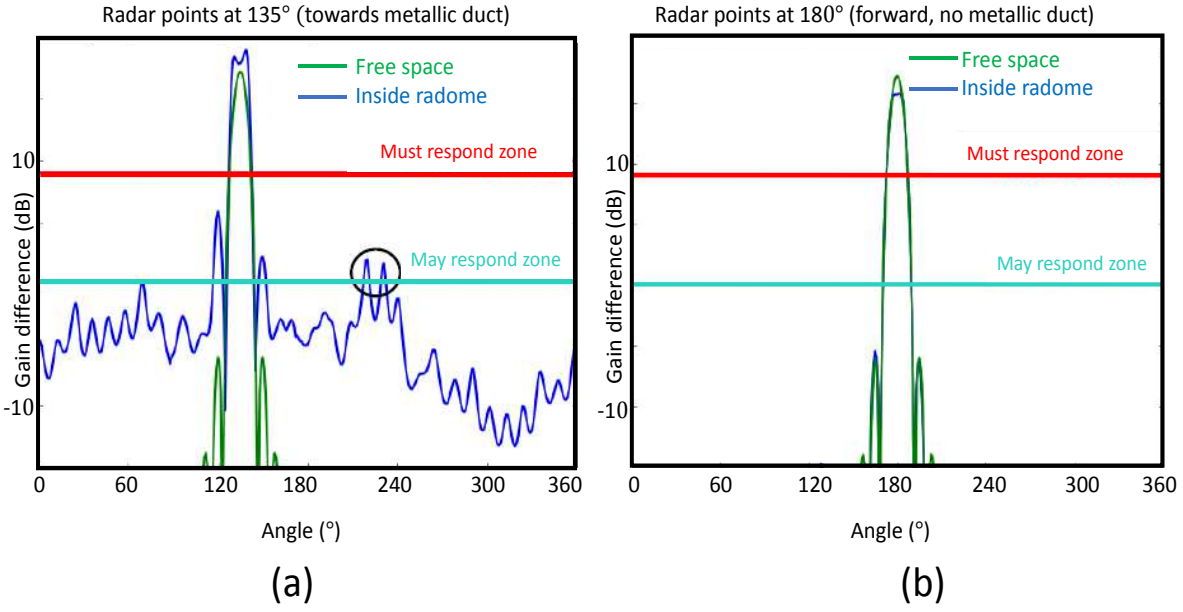

FIGURE 1.5: The gain difference vs azimuth angle when the IFF points: (a) towards the metallic duct and (b) when it points forward. The blue curves represent the scenario when the antenna is inside the radome (with the metallic duct) and the green curves represent simulations in free space (without radome and metallic ducts).

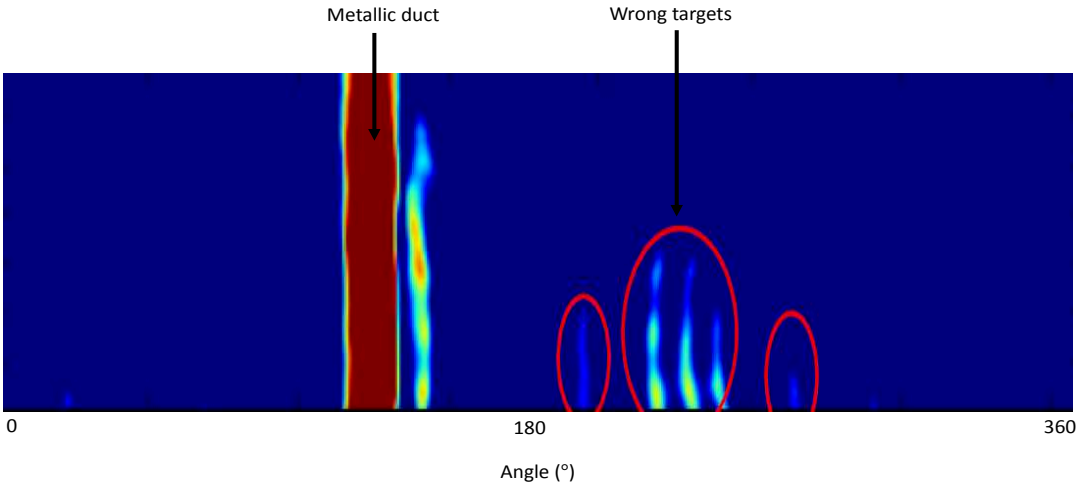

FIGURE 1.6: Detection of wrong targets.

1.2.3 Objectives

By using two confidential internal studies made by the systems department of CMN, it has been shown that the metallic ducts can cause EMC problems inside radomes such as path loss, and detection of wrong targets. Other studies (not shown in this thesis) have shown that the metallic ducts can cause saturation of antenna and radars, false echoes and shadow zones. The objective of this thesis is to propose solutions to face EMC problems caused by the reflexion of EW towards the sources. In order to reduce the reflections electromagnetic radar absorbers are studied and designed. The frequency range of interest is the 1 - 10 GHz band. For practical reasons, broadband radar absorbers are of our interest. During the thesis, all the absorbers that have been developed are based on Metamaterials (MM) and Frequency Selective Surfaces (FSS). The reasons behind this choice is given in Chapter 2. The chapter-wise plan of the thesis is as follows:

- Background Theory

First, in Chapter 2, a background theory on conventional flat broadband radar absorbers, Metamaterials (MM) and Frequency Selective Surfaces (FSS) is described. For the flat conventional broadband absorbers, two cases are considered: Magneto-dielectric absorbers and resistive sheet based absorbers. The advantages and drawbacks of both type of absorbers are also given. As far as MM and FSS are concerned, a very brief description, some applications and three examples of MM based absorbers are described. Then, by using the equivalent Transmission Line Model (TLM) , the design of perfect absorbers by impedance matching is described in detail for normal and oblique incidences for both Transverse Electric (TE) and Transverse Magnetic (TM) polarizations. Then, a subsection is dedicated on how to judge the performance of broadband radar absorbers. Throughout the thesis, the performance of all the absorbers that have been studied are judged upon the description of this subsection. Another subsection is dedicated for some basic informations about monostatic Radar Cross Section (RCS).

- Theoretical analysis for systematic design of FSS based broadband radar absorbers

After some theoretical analysis of the Transmission Line Model (TLM) of absorbers, two approaches for designing the physical model of FSS based radar absorbers are presented. The first consists of metallic square loops associated with lumped resistors printed on a grounded dielectric substrate and the second one deals with resistive square loops deposited

on top of a grounded dielectric substrate. The required dimensions of flexible absorbers in some low frequency bands are also given in order to show the versatility of the approach. The monostatic RCS of the proposed strcuture has also been simulated at some frequencies in the absorption band. This work has been published in Progress In Electromagnetics Research C and entitled 'Theoretical Analysis for Systematic Design of Flexible Broadband Radar Absorbers Using the Least-Square Method'.

- A single layer broadband radar absorber

In Chapter 4, our work on a single layer, FSS based broadband radar absorber is presented. Our contribution and the challenge of this work is to achieve broadband absorption using a very thin single layer dielectric and it is achieved by rotating the resonating element by 45°. An original optimized Underlined U shape Resonator (UUSR) has been developed for the resonating element which provides a broadband co-polarization absorption. First, the main lines of methodology about how the final structure is obtained, has been described. In order to understand the absorption mechanism, a general TLM of an absorber and the three near unity absorption peaks have been used to study the electric and magnetic fields. The physical insight of how the three near unity absorption peaks are achieved has also been discussed. After fabricating the structure, the measurements were found to be in good agreement with the simulation results. The RCS of the radar absorber has been calculated for the three near unity absorption peak frequencies and it has been shown that the proposed structure considerably reduces the co-polarization RCS when compared to a planar conducting plate. This work has been published in mdpi Materials journal and entitled 'A co-polarization broadband radar absorber for RCS reduction'.

- A dual layer broadband radar absorber

A thin dual-layer broadband radar absorber based on FSS is described in chapter 5. The proposed structure consists of periodically arranged metallic patterns printed on two dielectric substrates separated by an optimized air gap. First, the main lines of methodology about how the final structure is obtained, has been described. In order to understand the absorption mechanism, the three near unity absorption peaks have been used to study the power loss density, electric and magnetic fields. The physical insight of how the three near unity absorption peaks are achieved has also been discussed. After fabricating the structure, the measurements were found to be in good agreement with the simulation results. As in our work on single layer absorber described in Chapter 4, the resonator of the first

layer is rotated by 45°. The monostatic RCS of the proposed full structure is shown at the three near unity absorption peaks. This work has been published in Nature Scientific Reports and is entitled 'A dual layer broadband radar absorber to minimize electromagnetic interference in radomes'.

- Total scattering reduction from cylindrical bodies

All radar absorbers presented in Chapters 2, 3, 4 and 5 are suitable for planar stuctures. In Chapter 3, we have designed a flexible radar absorber for non planar structures. Nevertheless, if used for a cylindrical target, the radius of the target must be very big when compared to the free space wavelength. If the cylindrical target's radius is comparable or smaller compared to the wevelength, then radar absorbers designed for planar targets are not suitable. When a metallic cylindrical body is illuminated by an EW, the latter will scatter EW in all directions around the body. The amplitudes of the scattered fields depends on the radius of the cylindrical body. Depending on the applications, the scattered EM fields can be more or less critical. A way of reducing scattering from cylindrical targets is explained in detail in Chapter 6.

- General Conclusion and future works

Finally, in the last chapter, a general conclusion on the whole thesis is given. Ongoing and future works of all the developped radar absorerbers are also discussed. A comparison of our developped absorbers with other absorbers found in the literature is also given.

- Appendices

A long summury of the thesis in french is given in Appendix A. The list of publications is given in Appendix B.

Chapter 2

BACKGROUND THEORY ON RADAR ABSORBERS AND METAMATERIALS

2.1 Conventional flat broadband radar absorbers

In stealth applications, mainly for military purposes, an absorber must be as thin as possible and the reflection must be very small in a wide frequency range. It must also be noted that often military applications does not require absorption for a wide range of oblique incidence.

2.1.1 Magneto-dielectric absorbers

First, let us consider a flat metallic plate as a target on top of which we must put an absorbing layer. We assume the absorbing layer to be magneto-dielectric as illustrated in Figure 2.1.

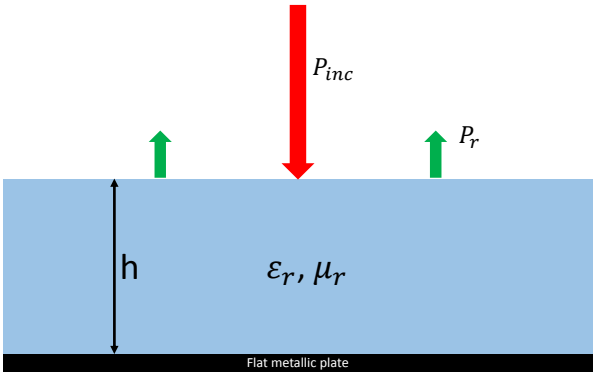

FIGURE 2.1: Illustration of magneto-dielectric layer of thickness, h, placed on top of a flat metallic plate. P_{inc} represents the incident power and P_r represents the reflected power.

As described in [1], the input impedance of the grounded magneto-dielectric layer illuminated by a linearly polarized TEM wave is given by:

$$Z_{in} = j\eta_0\sqrt{\frac{\mu_r}{\epsilon_r}}tan(k_0h\sqrt{\epsilon_r\mu_r}), \tag{2.1}$$

where h is the thickness of the magneto-dielectric layer, $k_0 = \omega\sqrt{\epsilon_0\mu_0}$ and $\eta_0 = \sqrt{\mu_0/\epsilon_0}$.

The reflection coefficient of the grounded magneto-dielectric absorber is given by:

$$R = \frac{Z_{in} - \eta_0}{Z_{in} + \eta_0} = \frac{j\sqrt{\mu_r}tan(k_0h\sqrt{\epsilon_r\mu_r}) - \sqrt{\epsilon_r}}{j\sqrt{\mu_r}tan(k_0h\sqrt{\epsilon_r\mu_r}) + \sqrt{\epsilon_r}} \tag{2.2}$$

For an electrically thin ($k_0h|\sqrt{\epsilon_r\mu_r}| << 1$) magneto-dielectric absorber, the tangent function in Equation 2.2 can be approximated and the reflection coefficient can be written as:

$$R \approx \frac{jk_0h\sqrt{\epsilon_r}\mu_r - \sqrt{\epsilon_r}}{jk_0h\sqrt{\epsilon_r}\mu_r + \sqrt{\epsilon_r}} = \frac{jk_0\mu_rh - 1}{jk_0\mu_rh + 1} \tag{2.3}$$

From Equation 2.3, it can be seen that the permittivity (ϵ_r) of the magneto-dielectric absorber does not affect the reflection coefficient. This is due to the fact that the tangential electric field is zero on the metal surface and the absorbing layer being electrically thin, the electric field remains very small on the whole structure.

The permeability (μ_r) of the magneto-dielectric layer being complex, it can be written in the form: $\mu_r = \mu'_r - j\mu''_r$. Thus the absolute value of the reflection coefficient takes the following form:

$$|R|^2 = \frac{(1 - k_0 h\mu''_r)^2 + (k_0 h\mu'_r)^2}{1 + k_0 h\mu''_r)^2 + (k_0 h\mu'_r)^2} \tag{2.4}$$

In order the nullify the reflection in Equation 2.4, the two criterion must be obeyed:

$$\mu''_r = \frac{1}{k_0 h} \qquad and \qquad \mu'_r << \frac{1}{k_0 h} \tag{2.5}$$

The propagation constant, k_0, depending on the frequency, μ''_r must be frequency dispersive and the μ'_r must be much smaller than μ''_r in the whole required frequency band for small reflection. Such materials can be realized [2] but the frequency range is limited. Also, these materials loose their magnetic properties with increasing frequency. Furthermore magnetic materials such as ferrite are heavy and expensive.

If the case of magnetic materials is dropped, meaning that the permittivy of the layer placed on top of the flat mateallic plate is non magnetic ($\mu_r = 1$), then Equation 2.3 can be simplified to:

$$R = \frac{jtan(k_0 nh) - n}{jtan(k_0 nh) + n}, \tag{2.6}$$

where $n = \sqrt{\epsilon_r}$ is the complex refractive index of the layer. By using Equation 2.6, for a given thickness of the dielectric layer, a color map can be plotted to find the complex value of the refractive index that gives zero reflection at a particular frequency. Figure 2.2 represents the color maps for zero reflection at normal incidence at 3 GHz for dielectric thicknesses of $\lambda/10$, $\lambda/8$, $\lambda/6$ and $\lambda/4$. λ is the wavelength in free space at 3 GHz.

For $\lambda/10$ of dieletric thickness, the permittivity must be of $6.6744 - j3.127$, for $\lambda/8$ thick dielectric the permittivity must be of $4.384 - j2.4738$, for $\lambda/6$ thick dielectric the permittivity must be of $2.6325 - j1.8468$ and finally, for $\lambda/4$ thick dielectric the permittivity must be of $1.392 - j1.1938$. Table 2.1 recapitulates the dielectric properties needed according to their thicknesses for perfect absorption at normal incidence for 3 GHz.

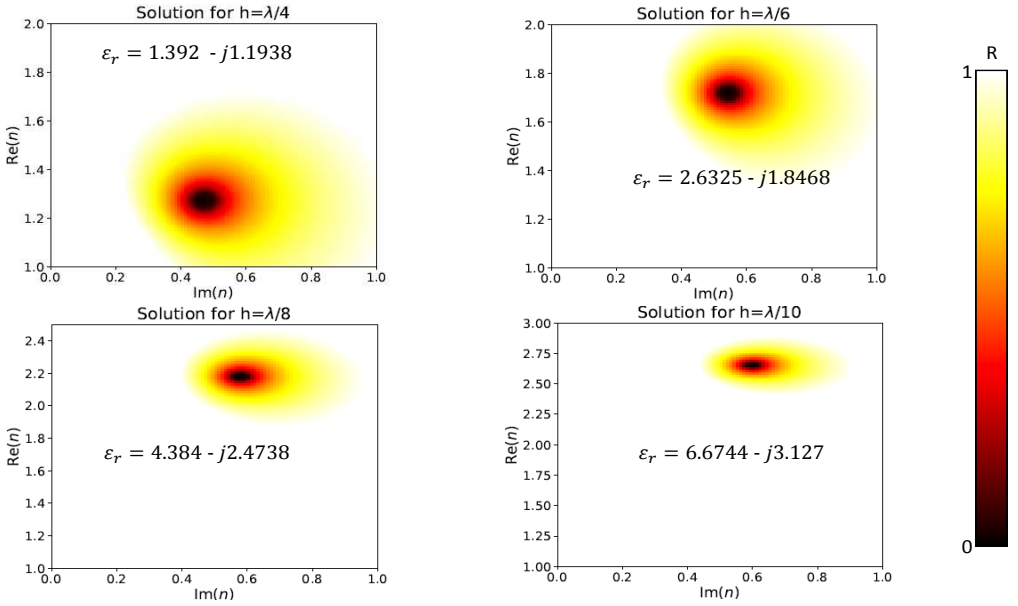

FIGURE 2.2: Color map for zero reflection for normal incidence of different thicknesses of dielectric. The x axes represent the imaginary part of refractive index and the y axes represent the real part of refractive index. As $n = \sqrt{\epsilon_r}$, the corresponding ϵ_r is also given for each thickness.

Parameter	$\lambda/10$	$\lambda/8$	$\lambda/6$	$\lambda/4$
$\epsilon_r^{'}$	6.6744	4.384	2.6325	1.392
$\epsilon_r^{''}$	3.127	2.4738	1.8468	1.1939
$tan\delta = \epsilon_r^{''}/\epsilon_r^{'}$	0.4685	0.5642	0.7	0.8576

TABLE 2.1: Dielectric properties needed according to their thicknesses for perfect absorption at normal incidence for 3 GHz.

Now that the required permittivities of the dielectric layer for different thicknesses have been calculated for zero reflection at 3 GHz, the absorption rate of the corresponding absorbers can be simulated and plotted. The absorption rate is given by:

$$A = 1 - |R|^2 - |T|^2, \tag{2.7}$$

where R and T are the reflexion and transmission coefficients. In our case the dielectric layer being placed on top of a metallic plate, the transmission coefficient will be zero. The simulation was done using commercial CST Design Studio Suite 2017. Periodic boundary conditions were applied in the numerical model in order to mimic a 2D infinite structure. Floquet ports were used for the excitation and the period of the structure was equal to

$\lambda/10$. An illumination of linearly polarized normally incident TE wave is considered. The analytical absorption rates were calculated using Equations 2.6 and 2.7. An excellent agreement was found between the analytical model and simulated CST results as shown in Figure 2.3.

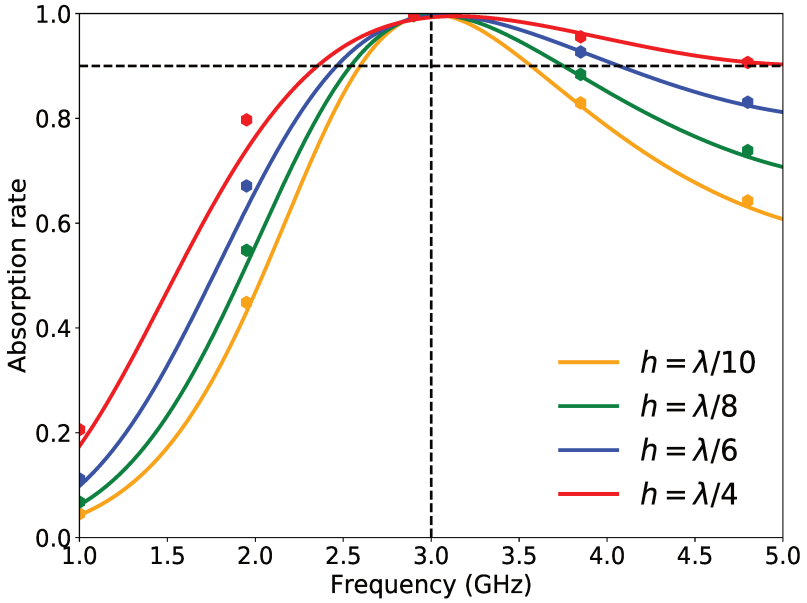

FIGURE 2.3: Absorption rate for different thicknesses of dielectric. The continuous curves are simulated absorption rates and the circles are their corresponding analytical absorption rates.

Several observations can be made by the absorption rates of Figure 2.3. Firstly, for both simulated (continuous curves) and analytical (circles), unity absorptions are obtained (zero reflexion) at 3 GHz, for all the thicknesses of dielectric as their corresponding permittivities have been calculated to have zero reflexion at 3 GHz. This observation validates our color map design plan. Secondly, with increasing thickness the 90% absorption band increases but the 90% absorption bandwidth remains around 1.6 GHz. Finally, for $\lambda/4 = 25$ mm thick dielectric, the absorption band is broadened. This is due to the fact that the material is very lossy and also due to the big thickness of the dielectric material. The advantage of the presented broadband $\lambda/4$ thick dielectric absorber is its exceptional 90% absorption bandwidth. This two main drawbacks of such absorber is their bulkiness and these specific values of permittivity of the dielectrics are not easily available.

2.1.2 Resistive sheet based absorbers

As it has been stressed in the magneto-dielectric absorber subsection, the thickness and the permittivity of the dielectric can be a problem for designing broadband absorbers. One solution to use easily available dielectrics is to put a resistive sheet on top of a $\lambda_m/4$ thick grounded dielectric represented in Figure 2.4. λ_m is the wavelength in the dielectric material. Such absorbers are called Salisbury screens [3, 4, 5]. Using multilayers of resistive sheets placed on top of $\lambda_m/4$ thick dielectrics is called Jaumann absorbers [6, 7, 8].

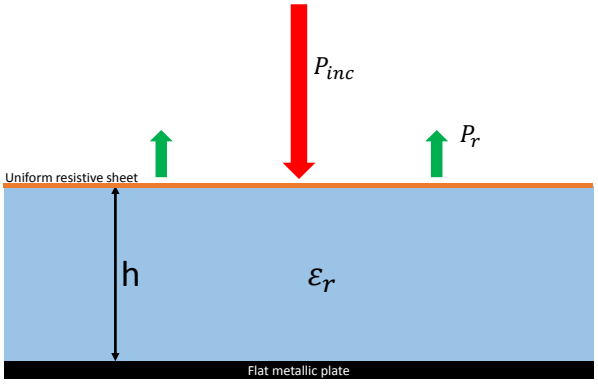

FIGURE 2.4: Illustration of a uniform resistive sheet placed placed on top of a grounded flat dielectric.

In the example below, the absorption rate for different values of resistive sheet of a Salisbury screen type absorber is plotted in Figure 2.5. The same simulation parameters (boundary condition, incident wave) have been used as in the Magno-dieletric absorbers sub section. The center frequency is chosen to be 5 GHz and for this example, the dielectric permittivity is of 1 (air). Hence, the resistive sheet is placed at $\lambda_m/4 = 15$ mm above the flat metallic plate.

It can be observed in Figure 2.5 that when the resistance of the resistive sheet is between 350 - 400 Ω/sq, near unity absorption is obtained at 5 GHz. For the absorber of 350 Ω/sq resistive, the 90% absorption bandwidth is in the range of 3 - 7 GHz. In this example, air has been used for the dielectric spacer. In fact any dielectric can be used (FR4, Rogers...) for compact and rigid designs. The thickness ($\lambda_m/4$) and the resistive sheet value must then be adjusted. With the Salisbury screen or Jaumann absorber, any easily available dielectric can be used but these two type of absorbers remain bulky due to their ($\lambda_m/4$) thicknesses.

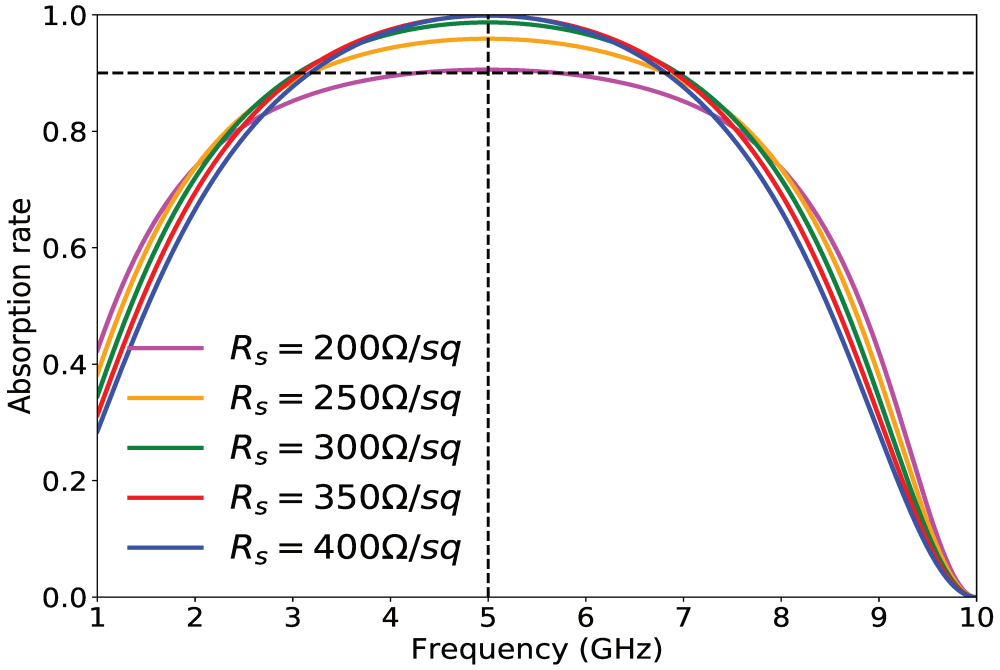

FIGURE 2.5: Absorption rate a a Salisbury screen for different values of resistive sheet.

2.1.3 Conclusion

For magneto-dieletric radar absorbers using a magnetic material, the imaginary part of its permeability must de frequency dispersive and must be much bigger than its real part in the whole working frequency range for absorption. Such materials are realizable but the absorption frequency range is limited. Moreover magnetic materials are very expensive. If non magnetic materials are used, by proper optimization of the permittivity, extremely broadband absorption can be obtained. The main drawback of this type of absorber is the that dielectrics having the exact required permittivity are not always commercially available and also due to their $\lambda/4$ thickness, they are generally bulky and heavy. Concerning resistive sheet based absorbers, by taking the example of a Salisbury screen, it has been shown that by fixing the permittivity of the dielectric and the thickness at $\lambda_m/4$, broadband absorption can be obtained. Such absorbers (Jaumann, Salisbury screen) are known to be bulky.

2.2 Metamaterials and Frequency Selective Surfaces

2.2.1 Brief description and applications

Unlike conventional materials, which exhibit their electromagnetic properties from their constituent atoms, Metamaterials (MM) exhibit their electromagnetic properties from their constituent unit cells [9]. MM are engineered to have properties that have not yet been found by conventional materials. They are engineered by assembling multiple elements fashioned from composite materials such as metals or plastics. The whole structure of a MM is usually made by repeating the unit cells at scales (periods) that are smaller than the wavelengths. MM do not derive their properties the base materials, but from their newly designed structures. MM can provide electric and magnetic properties that are not available in conventional materials found in the nature such as negative refractive index [10, 11, 12, 13], extreme anisotropy [14, 15, 16, 17, 18], extreme chilarity [19, 20, 21, 22, 23], continuously variable properties throughout the material [24, 25, 26, 27], magnetism at optical frequencies [28, 29, 30, 31] and so on. Their precise shape, geometry, size, orientation and arrangement gives them their smart properties capable to manipulate electromagnetic waves [32, 33, 34, 35]. MM cover a wide range of applications such as antennas [36, 37, 38, 39, 40, 41], electromagnetic absorbers [42, 43, 44, 45, 46, 47], lenses [48, 49, 50], cloaking [51, 52, 53, 54, 55, 56] and so on.

Frequency Selective Surfaces (FSS) [57, 58] are a family of MM. They are an array of periodically arranged elements, that shows a particular filtering behavior with respect to the frequency. The two most common applications of FSS are filters [59, 60, 61] and absorbers [62, 63, 64]. For example they can be used to prevent Electromagnetic Interference (EMI) between two antennas operating in overlapping frequency bands [65, 66, 67], to reduce the Radar Cross Section (RCS) of antennas located on a ship's radomes or in the nose of an aircraft [46, 47] and so on .

2.2.2 Examples of Metamaterial based electromagnetic wave absorbers

Let us consider a narrowband EW absorber for the first example. This example is the research done by Landy & al. in 2008 and entitiled "Perfect Metamaterial Absorber" [44]. The unit cell of the EW absorber is presented in Figure 2.6(a).

The EW absorber consists of two metamaterial resonator layers separated by a FR4 dielectric substrate of thickness 0.6 mm. The top layer of the absorber consists of an Electric

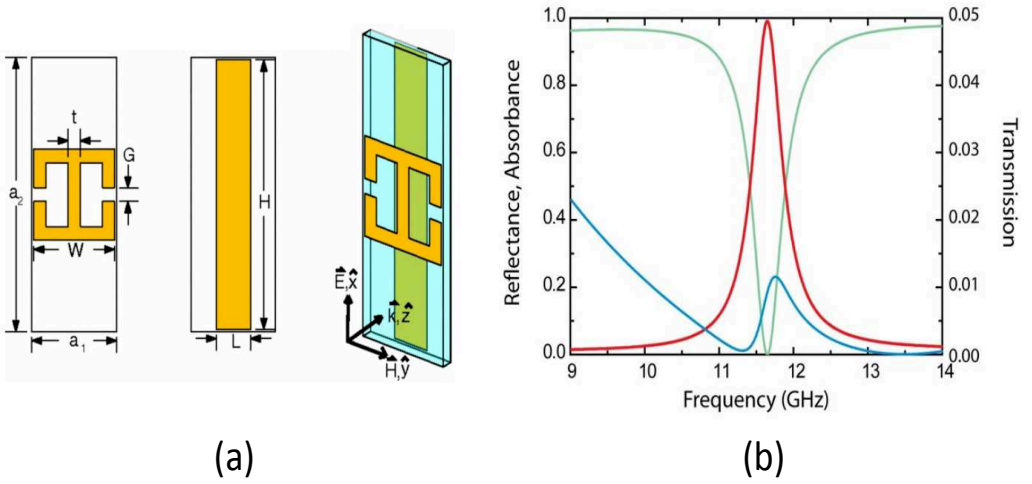

FIGURE 2.6: (a) Unit cell design of the perfect metamaterial proposed in [44]. (b) simulated absorption response of the structure under linearly polarized TE wave.

Ring Resonator (ERR) and a cut wire is designed at the bottom layer. The dimensions of the absorber can be found in [44]. The absorption rate, presented in 2.6(b), is reported as 96% at 11.65 GHz and the Full width Half Maximum (FWHM) bandwidth is 4%. The top and bottom layers couples strongly to incident electric field to contribute electric response at the certain resonance frequency. As by matching ϵ and μ a metamaterial can be impedance-matched ($Z(f) = \sqrt{\mu(f)/\epsilon(f)}$), the magnetic response is provided by the circulating flow of antiparallel surface currents at the top and bottom layers. The absorption frequency is controlled by the geometric parameters of ERR structure and the magnetic response is controlled by altering the gap between the two metallic layers. The ERR designs are also usually referred as electric field driven resonator based designs.

Furthermore, the researchers have rigorously investigated the loss mechanism of the absorber through simulations and postulated that the dielectric loss is an order of magnitude greater than the ohmic loss as shown in Figure 2.7. It is observed that the center conducting region provides the ohmic loss, however, significant dielectric loss is observed in between the metamaterial elements at the location of maximum electric field. Therefore, the dielectric is the main contributor of loss in this metamaterial based microwave absorber.

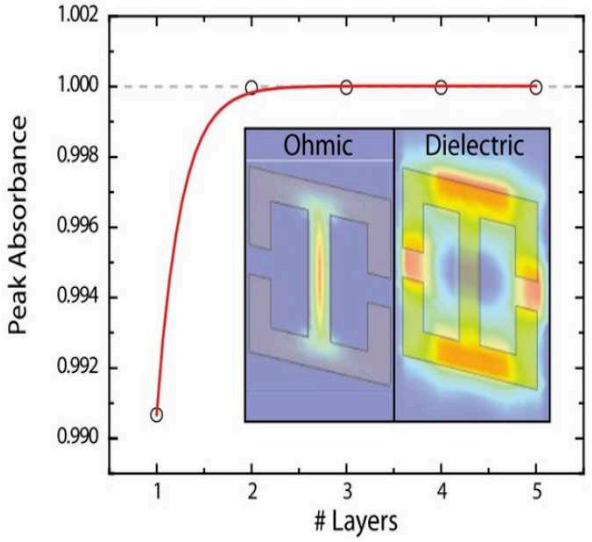

FIGURE 2.7: Absorption rate for multiple layers.

In the following example the research done by Wang & al. in 2015 on multiband metamaterial absorber and entitiled "Novel Quadruple-Band Microwave Metamaterial Absorber" [69] is summurized. The unit cell of the EW absorber is presented in Figure 2.8(a). The dimensions of the absorber can be found in [69]. The structure is composed of a Electric Split Ring (ESR) placed on top of a 0.217 mm metal backed FR4.

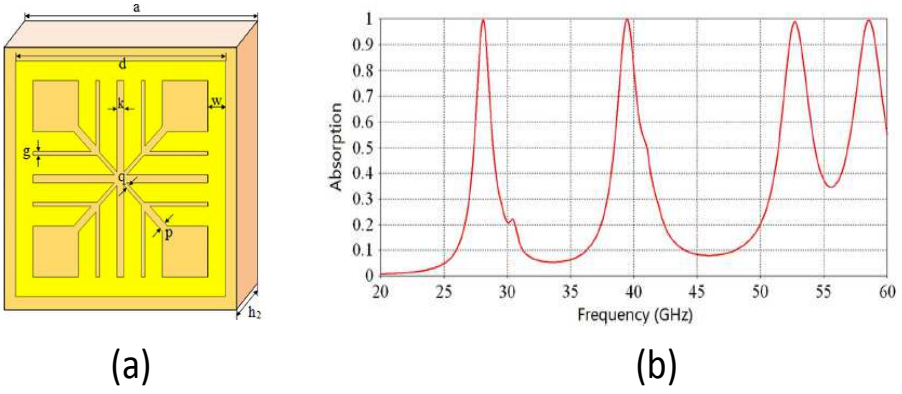

FIGURE 2.8: (a) Unit cell design of the perfect metamaterial proposed in [69]. (b) Simulated absorption response of the structure under linearly polarized TE wave.

The absorption rate is presented in 2.8(b). The EM absorber provides four absorption peaks at 28.21 GHz, 39.59 GHz, 52.78 GHz, and 58.63 GHz with absorption rates of 99.47%, 99.94%, 99.05%, and 99.55%, respectively.

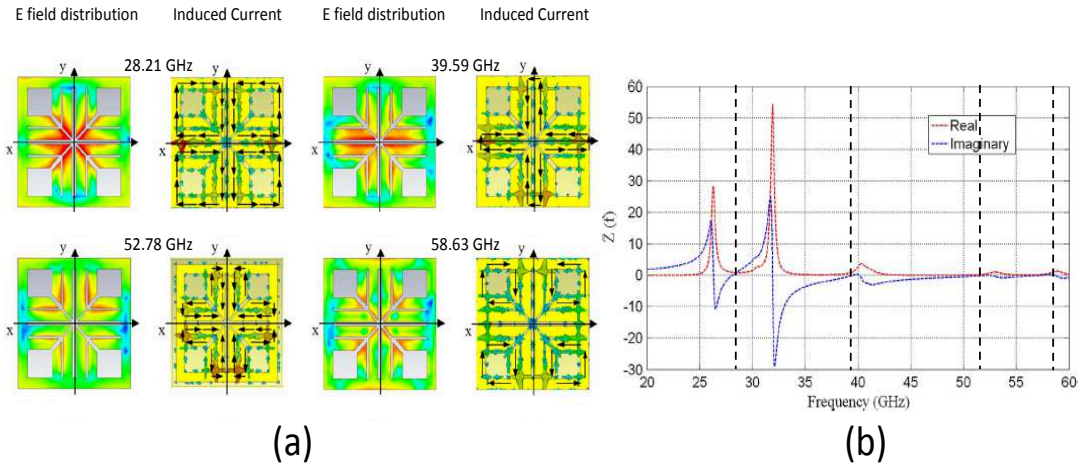

FIGURE 2.9: (a) Electric field distribution and induced current at the four absorption peaks. (b) Normalized effective impedance of the structure [69]. The four vertical dotted lines shows the frequencies where absorptions have been obtained. In this case the normalized real part of the impedance is close to 1 and the normalized imaginary part of the impedance is close to 0.

According to the authors, the first resonance frequency is mainly contributed by the large ESR resonators while the fourth resonance frequency is mainly provided by the small ESRR in each quadrant (Figure 2.9(a)). For these two cases, the electric field is mainly localized within the oblique slots of ESRR, enabling the electric energy to be mainly confined in those regions. In addition, the induced current in the ground plate is anti-parallel to those exhibited in the top layer, generating a strong magnetic resonance. As shown in Figure 2.9(a), the electric field at the second resonance frequency is localized within the slots between large ESRR, and the electric field at the third resonance frequency is mainly distributed within the slots between large and small ESRR. Therefore, most of the power is lost due to the high confinement of energy. Meanwhile, the distribution of currents at the second frequency are mainly along the adjacent bars of two large ESRR, while the surface currents at the third resonance frequency mainly concentrate on the bars of large and small ESRR in each quadrant. The antiparallel currents, appearing at different positions in the ground plate, associated with the two electric resonances, are also excited to provide the corresponding magnetic resonances. The authors have also calculated the

effective impedance of the structure ($Z(f) = \sqrt{(1+S_{11})/(1-S_{11})}$) to show that the EM absorber impedance matches the free space impedance at the near unity absorption peak frequencies as shown in Figure 2.9(b).

The last example of MM based EW absorber concerns broadband absorbers. The following work was done by Xiong & al. in 2013 and entitled "An ultrathin and broadband metamaterial absorber using multi-layer structures" [70]. One of the most common ways of increasing the bandwidth is to use multilayers. The authors have proposed a MM absorber that is composed of a periodic array of loop-dielectric multilayered structure. Numerical results show that the absorption at normal incidence is more than 90% in the frequency range of 8.37–21 GHz. The structure has a thickness of 3.65 mm and all other dimmensions can be found in [70]. The unit cell of the proposed MM absorber is presented in Figure 2.10(a) and the simulated absorption response of the structure under linearly polarized TE wave is presented in Figure 2.10(b). Different absorption results for different values of the final layer's thickness is presented in Figure 2.10(b).

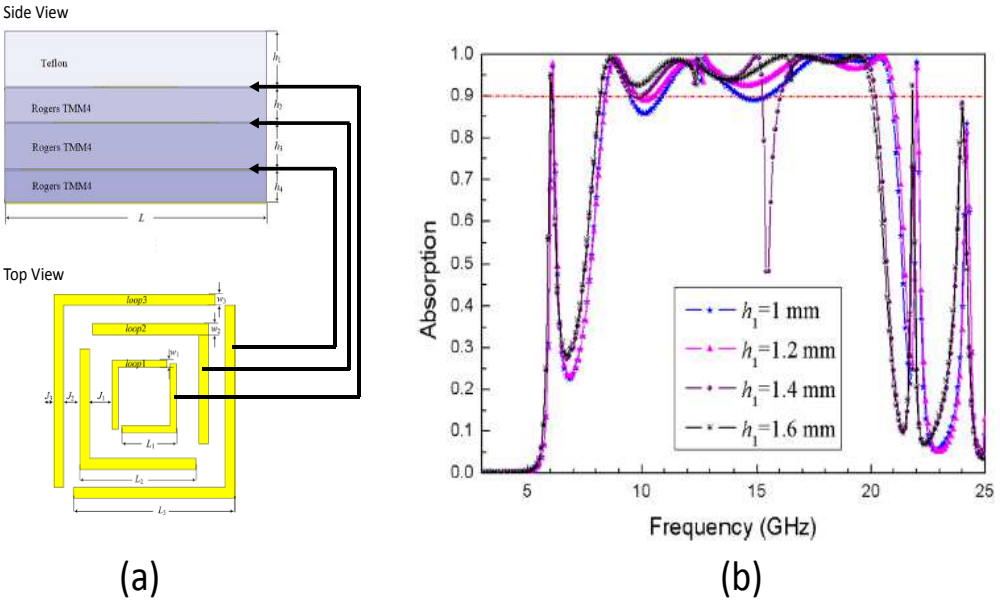

FIGURE 2.10: (a) Unit cell design of the perfect metamaterial proposed in [70]. (b) Simulated absorption response of the structure under linearly polarized TE wave.

The authors have explained the absorption mechanism by using the destructive interference method and by presenting the electric field and magnetic field distribution.

In any case, the surface impedance of a radar absorber must match the impedance of the free space at a given frequency in order to have perfect absorption at that particular frequency. Using MM, which are engineered materials, the effective permittivity and permeability of the MM absorber can be tailored such that its surface impedance matches the free space impedance. By several resonating elements (resonating at different frequencies), multiband EW absorbers can be created. By using mulilayered MM absorbers, the absorption bandwidth can be increased. We have described briefly only three examples of MM based absorbers but references are given in our published journal and conference papers which can be found in Appendix B. In the next subsection, a detailed explanation is given on how to obtain absorption using FSS of MM by studying their equivalent TLM.

2.2.3 Impedance matching of Metamaterial radar absorbers by Transmission Line Model

2.2.3.1 Absorption for normal incidence

One solution to design an FSS (or MM) absorber is to place a complex sheet over a grounded dielectric. The complex sheet provides the required real and imaginary impedances for absorption. The complex sheet is designed in a way that it matches the impedance of the free space.

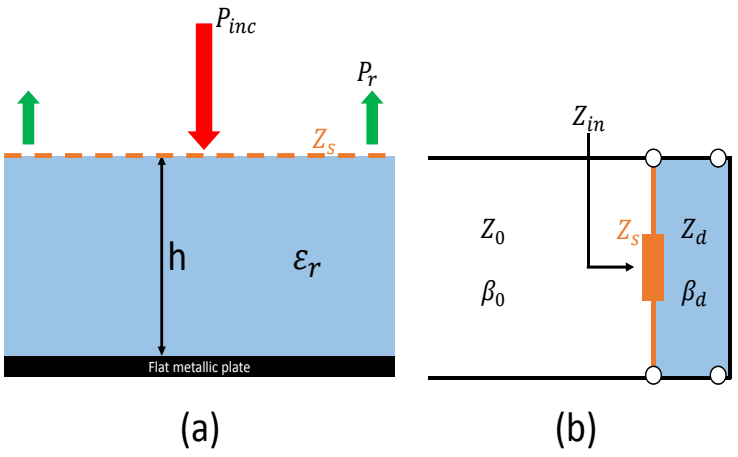

FIGURE 2.11: (a) Schematic representation of a metasurface absorber. (b)Equivalent TLM of the absorber.

A schematic representation of a metasurface absorber is shown in Figure 2.11 (a) and its equivalent circuit model (or TLM) is depicted in Figure 2.11 (b). A dielectric layer of

permittivity, ϵ_r, having a thickness, h, and a characteristic impedance, $Z_d = \sqrt{\mu_0/\epsilon_0\epsilon_r}$, is sandwiched between a metallic ground and a complex impedance sheet, Z_s. The metallic ground is used to prevent any transmission. Using the TLM [1, 68], the impedance of the grounded substrate is given by:

$$Z_g = jZ_d tan(\beta_d h), \tag{2.8}$$

where $\beta_d = \frac{\omega\sqrt{\epsilon_r}}{c}$ is the propagation constant in the dielectric. The input impedance, Z_{in}, is given by the parallel combination of the grounded dielectric (Z_g) and the complex sheet (Z_{sr}):

$$Z_{in} = \frac{jZ_{sr}Z_d tan(\beta_d h)}{Z_{sr} + jZ_d tan(\beta_d h)} \tag{2.9}$$

For perfect absorption, the reflexion must satisfy $R = (Z_{in} - Z_0)/(Z_{in} + Z_0) = 0$. Hence, perfect absorption is obtained when $Z_{in} = Z_0$. The required impedance of the complex sheet, Z_{sr}, for perfect absorption, satisfying $Z_{in} = Z_0$ is given by:

$$Z_{sr} = \frac{Z_0 Z_d tan(\beta_d h)}{jZ_0 + Z_d tan(\beta_d h)}, \tag{2.10}$$

where Z_0 is the impedance of free space. From Equation 2.10, we can see that the required complex sheet for perfect absorption depends on the characteristics of the dielectric (permittivity and thickness). The complex required impedance for different thicknesses is plotted according to Equation 2.10 in Figure 2.12. The permittivity of the substrate is fixed at $\epsilon_r = 4$ (lossless). As shown in Figure 2.12 (a) at 1 GHz, the real part of the required impedance increases as the thickness increases. On the contrary, again at 1 GHz, the imaginary part of the required impedance, in Figure 2.12 (b), decreases with increasing thickness. The thickness must be carefully selected such that the corresponding real and imaginary parts are physically realizable according to the used technology. As an example, the 10 mm thick dielectric is considered for further studies at the frequency of 1 GHz is considered. The corresponding complex required impedance is of 17.17 - j79.737 Ω at 1 GHz for a 10 mm thick dielectric having a permittivity of 4.

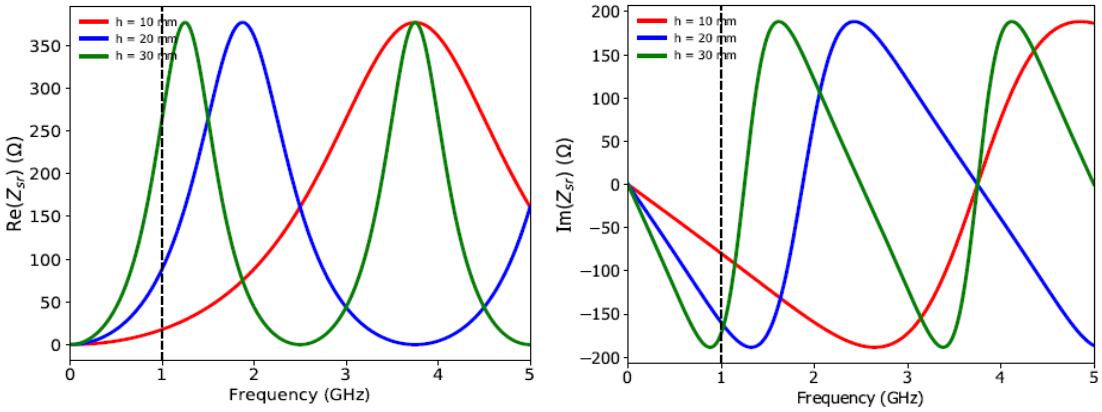

FIGURE 2.12: (a) Real part of required impedance. (b) Imaginary part of required impedance.

It should also be noted that positive values of the imaginary part of Z_{rs} imply that an inductive response is needed and negative values require capacitive response for perfect absorption. $Im(Z_{rs})$ being negative at 1 GHz in the presented case, the complex sheet must be capacitive whose circuit equivalent model can be given by a series of Resistor-Capacitor (R_sC_s) circuit in parallel of the 10 mm transmission line. The value, R_s, of the resistor is directly given by $Re(Z_{rs})$ which is 17.17 Ω in this case. The value of the C_s, of the capacitor is given by equating the impedance of the capacitor $(1/jC_s\omega)$ to $-j79.7370$. C_s is found to be equal to 1.995 pF. For a grounded absorber, the absorption is given by:

$$A = 1 - |R|^2, \tag{2.11}$$

where, R is the reflexion coefficient. The reflexion, R, is given by $R = (Z_{in} - Z_0)/(Z_{in} + Z_0)$. The absorption rate is plotted for a complex sheet placed on top of a grounded dielectric. The dielectric has an $\epsilon_r = 4$ and $h = 10$ mm and the complex sheet is modeled by a resistance of 17.17 Ω and a reactance of -79.737 Ω.

The red curve of Figure 2.13 corresponds to the absorption rate calculated analytically using Equations 2.8 - 2.11 and the blue curve corresponds to the simulated absorption rate. The simulation was done using CST Studio 2017. Periodic boundary conditions were applied in the numerical model in order to mimic a 2D infinite structure. Floquet

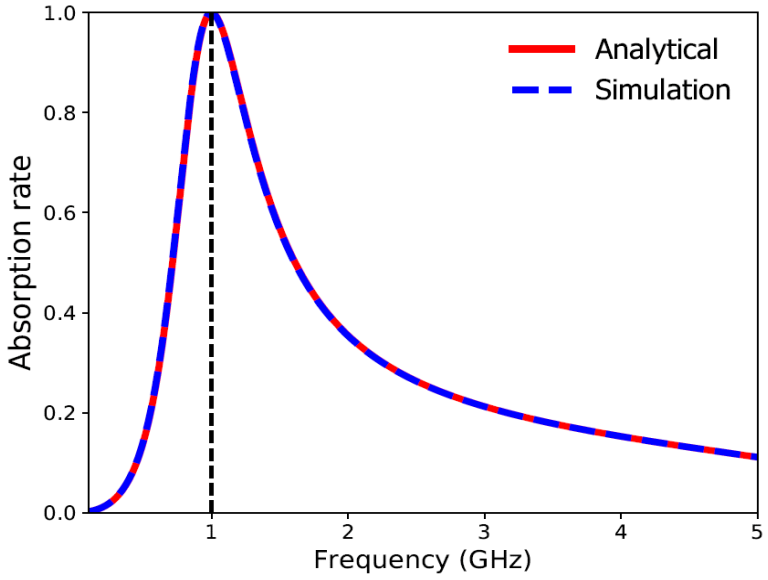

FIGURE 2.13: Analytical and numerical (simulated) absorption rates.

ports were used for the excitation of the periodic structure. The period of the structure was equal to 15 mm ($\lambda/20$). An excellent agreement is found between the analytical and numerical results. As predicted, perfect absorption is obtained at 1 GHz validating the design procedure (red curve). However, this procedure is valid for normal incidence only. The oblique incidence case is treated in the next subsection. The absorption bandwidth can be increased by increasing the thickness of the dielectric. As shown in Figure 2.12, different thicknesses of a fixed value of the permittivity of the dielectric requires different values of the complex impedance sheet for perfect absorption. Table 2.2 gives the values of complex impedance needed for perfect absorption at 1 GHz of different thicknesses. We fix the permittivity of the dielectric to 4 as previously.

h (mm)	10	20	30
$Re(Z_r)(\Omega)$	17.70	88.43	264.57
$Im(Z_r)(\Omega)$	-79.737	-159.741	-172.489

TABLE 2.2: Complex sheet impedances required for perfect absorption at 1 GHz for different thicknesses.

Figure 2.14 represents the absorption of different thicknesses of dielectric. The values of the complex sheet impedance are as given in Table 2.2.

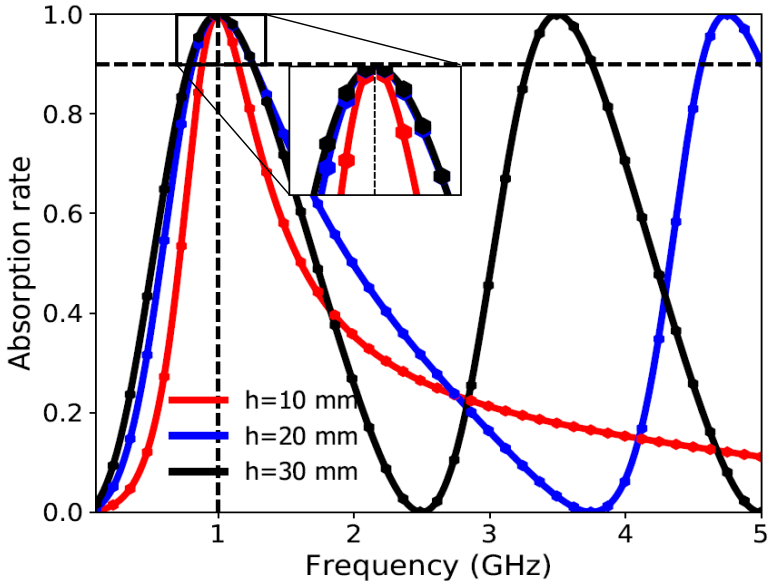

FIGURE 2.14: Calculated absorption rate for different thicknesses. The continuous lines correspond to simulation results and the hexagons on the lines correspond to the analytical results.

From Figure 2.14, two important remarks can be made. First, we can observe an increase in the bandwidth as the thickness increases. The table below gives the bandwidth value for different thicknesses of dielectric.

h (mm)	10	20	30
90% absorption bandwidth (MHz)	265.76	444.67	469.04

TABLE 2.3: 90% absorption bandwidth at 1 GHz for different thicknesses.

The second important remark that can be made is that for thicknesses greater or equal to 20 mm, a double absorption bandwidth is obtained between 3 and 5 GHz. To explain this, we take the dielectric of 20 mm of thickness as an example. In Figure 2.12, we can observe that the required complex impedance of the sheet to have perfect absorption is the same at 1 GHz and 3.5 GHz. Hence perfect absorption is obtained at two different frequencies.

2.2.3.2 Absorption for oblique incidences

Let us consider the case when a wave is obliquely incident on the surface of a metasurface. The impedance of the air is no more Z_0. The impedance of air, $Z_{0_{TE}}$, for perpendicular

(Transverse Electric, TE) and, $Z_{0_{TM}}$, for parallel (Transverse Magnetic TM) polarizations are given by:

$$Z_{0_{TE}} = \frac{Z_0}{cos(\theta_i)}, \tag{2.12}$$

$$Z_{0_{TM}} = Z_0 cos(\theta_i), \tag{2.13}$$

where θ_i is the incident angle. The impedance of the grounded dielectric susbtrate, Z_g, also changes. The impedance of the grounded dielectric, $Z_{g_{TE}}$, for TE, and $Z_{g_{TM}}$, for TM polarizations are given by:

$$Z_{g_{TE}} = jZ_{d_{TE}} tan(\beta_d h), \tag{2.14}$$

$$Z_{g_{TM}} = jZ_{d_{TM}} tan(\beta_d h) \tag{2.15}$$

where $Z_{d_{TE}} = \frac{Z_0}{\sqrt{\epsilon_r - sin^2(\theta_i)}}$, $Z_{d_{TM}} = Z_0\sqrt{(\frac{1}{\epsilon_r}) - (\frac{sin^2(\theta_i)}{\epsilon_r^2})}$, $\beta_d = \beta_0\sqrt{\epsilon_r - sin^2(\theta_i)}$ and $\beta_0 = \frac{w}{c}$.

Following the same reasoning as for normal incidence, the input impedances, $Z_{in_{TE}}$, for TE and $Z_{in_{TM}}$, for TM polarizations are given by:

$$Z_{in_{TE}} = \frac{jZ_{sr}Z_{d_{TE}} tan(\beta_d h)}{Z_{sr} + jZ_{d_{TE}} tan(\beta_d h)} \tag{2.16}$$

$$Z_{in_{TM}} = \frac{jZ_{sr}Z_{d_{TM}} tan(\beta_d h)}{Z_{sr} + jZ_{d_{TM}} tan(\beta_d h)} \tag{2.17}$$

For perfect absorption, the input impedances for TE and TM polarizations must be equal to the impedances of air for TE and TM polarizations respectively. Hence by $Z_{in_{TE}}$ to $Z_{0_{TE}}$ and $Z_{in_{TM}}$ to $Z_{0_{TM}}$, the required complex sheet impedances, $Z_{sr_{TE}}$, for TE and $Z_{sr_{TM}}$, for TM polarizations can be found:

$$Z_{sr_{TE}} = \frac{Z_0 Z_{d_{TE}} tan(\beta_d h)}{jZ_0 + jZ_{d_{TE}} cos(\theta_i) tan(\beta_d h)} \tag{2.18}$$

$$Z_{sr_{TM}} = \frac{Z_0 Z_{d_{TE}} cos(\theta_i) tan(\beta_d h)}{jZ_0 cos(\theta_i) + Z_{d_{TE}} tan(\beta_d h)} \tag{2.19}$$

Figure 2.15 illustrates the required impedance at different angles of a complex impedance sheet placed on a grounded dielectric. The dielectric has an $\epsilon_r = 4$ and $h = 10\ mm$. The case for TE polarization is considered as per Equation 2.11.

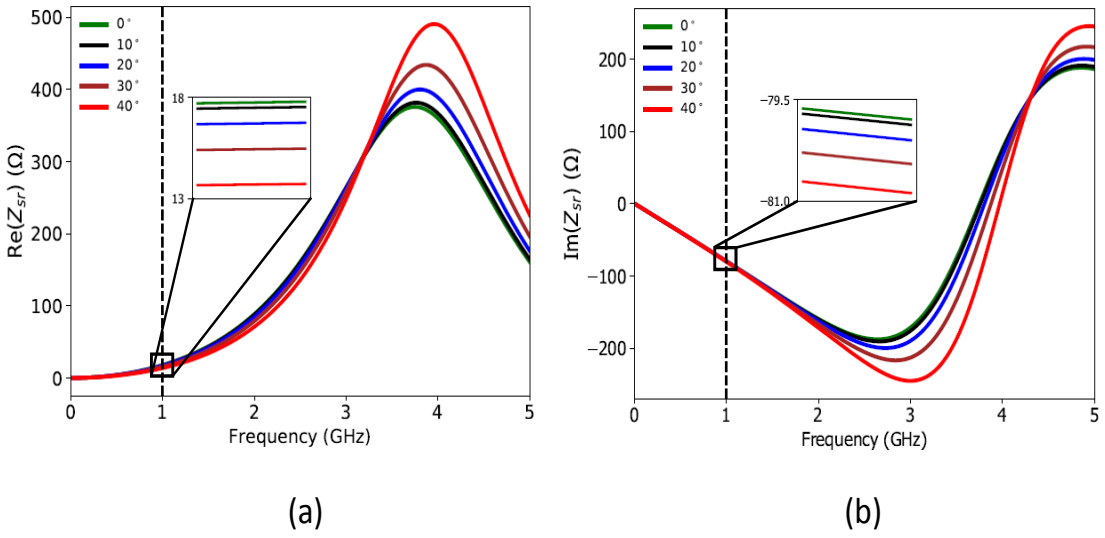

FIGURE 2.15: (a) Real part of required impedance for TE mode. (b) Imaginary part of required impedance for TE mode. The insets on both are a zoom around 1 GHz. The exact values of required impedances for perfect absorption for TE polarized oblique incidences is given in Table 2.4.

We can observe from Figure (a) and (b) that, at 1 GHz, the variation in the impedances are not big. The tables below provides values of real at imaginary parts of the complex impedance sheet for perfect absorption at different angles.

θ (deg)	0	10	20	30	40
$Re(Z_r)(\Omega)$	17.70	17.48	16.71	15.43	13.69
$Im(Z_r)(\Omega)$	-79.737	-79.804	-80.024	-80.385	-80.554

TABLE 2.4: Complex sheet impedances required for perfect absorption of a TE polarized wave for a grounded dielectric having $\epsilon_r = 4$ and $h = 10\ mm$.

The required impedance of the complex sheet for TM polarization can be determined using Equation 2.19. We use the same parameters of dielectric as for TE mode to find the real and imaginary parts of the complex impedance. Figure 2.16 illustrates the complex impedance required for perfect absorption of a TM polarized wave at 1 GHZ.

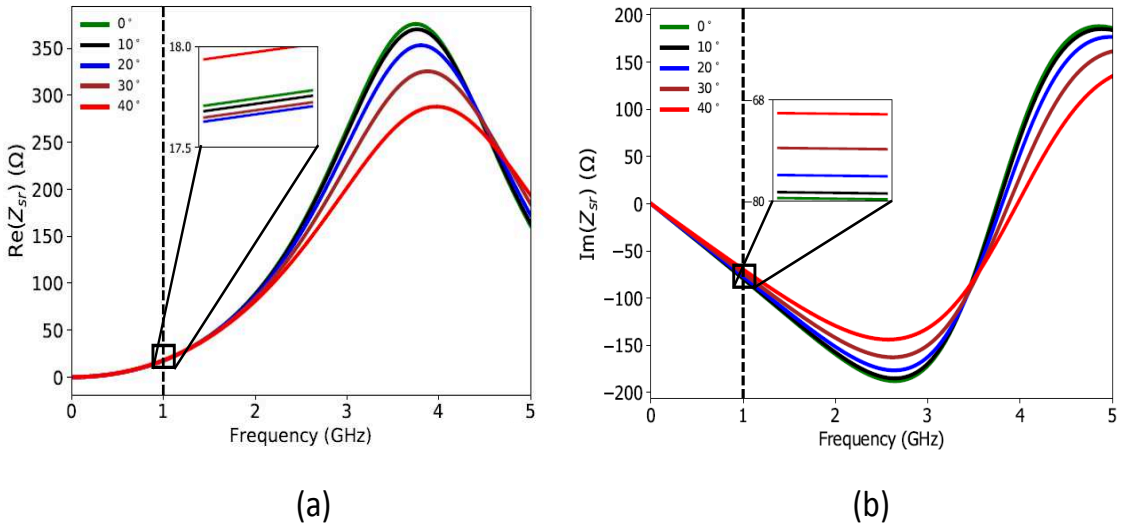

FIGURE 2.16: (a) Real part of required impedance for TM mode. (b) Imaginary part of required impedance for TM mode. The insets on both are a zoom around 1 GHz. The exact values of required impedances for perfect absorption for TMpolarized oblique incidences is given in Table 2.5.

The required impedance of the complex sheet for TM polarization is given in the table below.

For oblique incidences, as the reflection coefficients are not equal for TE and TM polarizations, the absorption rate will also not equal for TE and TM polarizations. Hence the

θ (deg)	0	10	20	30	40
$Re(Z_r)(\Omega)$	17.70	17.72	17.66	17.68	17.98
$Im(Z_r)(\Omega)$	-79.737	-79.023	-76.992	-73.777	-69.649

TABLE 2.5: Complex sheet impedances required for perfect absorption of a TM polarized wave for a grounded dielectric having $\epsilon_r = 4$ and h = 10 mm.

absorption for TE and TM polarizations are given by,

$$A_{TE} = 1 - |R_{TE}|^2, \tag{2.20}$$

$$A_{TM} = 1 - |R_{TM}|^2, \tag{2.21}$$

with $R_{TE} = \frac{Z_{in_{TE}} - Z_{0_{TE}}}{Z_{in_{TE}} + Z_{0_{TE}}}$ and $R_{TM} = \frac{Z_{in_{TM}} - Z_{0_{TM}}}{Z_{in_{TM}} + Z_{0_{TM}}}$. Figure 2.17 illustrates the absorption rate calculated analytically for TE mode of a complex sheet placed over a grounded dielectric having $\epsilon_r = 4$ and $h = 10\ mm$. The complex sheet impedances at different angles are as given in Table 2.4. Analytical results are compared to CST simulation results.

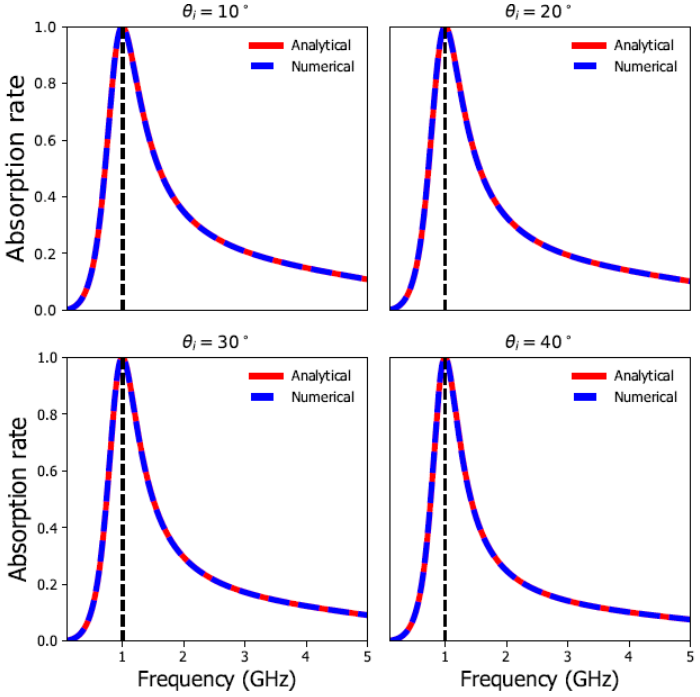

FIGURE 2.17: Absorption rate at 1 GHz for TE polarizations at different angles.

In Figure 2.17, we can observe that perfect absorption is found at 1 GHz for different angles both analytically and numerically. Moreover an excellent agreement is found between the analytical results and numerical (CST simulation) results.The absorption of the same absorber for TM mode is calculated. The values of the complex sheet impedance are as given in Table 2.5. The Figure 2.18 below depicts the analytical and simulated results.

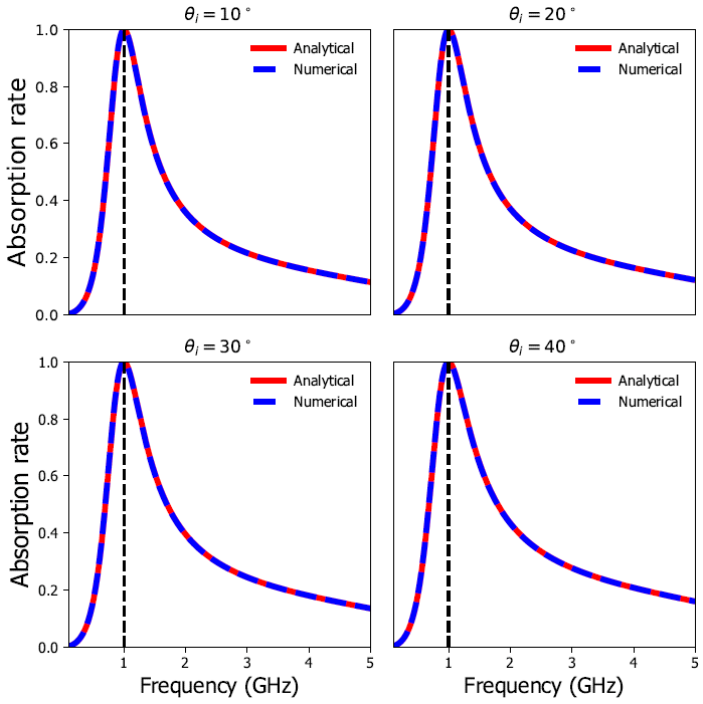

FIGURE 2.18: Absorption rate at 1 GHz for TM polarizations at different angles.

We can observe in Figure 2.18, that perfect absorption is found at 1 GHz for different angles both analytically and numerically and excellent agreement is found between the analytical results and numerical (CST simulation) results.

2.2.4 Conclusion

We have described in this section how by using MM or FSS, perfect absorption can be obtained. Proper resonating shapes and dimensions of FSS can provide required real and imaginary parts of surface impedance for absorption in a given frequency band. Also, FSS can be optimized such that broadband absorption is obtained for wide oblique incidence. Furthermore, these features can be obtained by using thin dielectrics. Apart from optimizing the resonant elements, in order to enlarge FSS based radar absorbers' bandwidth, two of the popular techniques used, consist of incorporating resonating elements working at nearby frequencies by arranging then on the same plane [71, 72, 73, 74] or by using multi layers [75, 76, 77]. Both techniques can lead to a drop in the absorption (sometimes S_{11} > -10 dB) at certain frequencies in the bandwidth. Using several elements on the same plane is very difficult to implement due to the lack of space in a small unit cell and coupling between different elements can be difficult to understand and interprete. Moreover, using different resonating elements on a single unit cell can lead to an asymmetrical design and hence degrading the performance considerably for oblique incidences and different polarizations. By following the same reasoning a multilayer structure can considerably increase the total height of the absorber. For all these reasons, designing thin broadband radar absorbers with easily available dielectrics especially for low frequencies (VHF/UHF) and the gigahertz regime (microwave) is very complicated and is a challenging subject.

2.3 Monostatic Radar Cross Section

The monostatic Radar Cross Section (RCS) tells us how strongly an object scatters electromagnetic fields when the transmitter and receiver are located at the same position [78]. This parameter measures the radar "visibility" of an object. In terms of power, electric and magnetic fields, the monostatic radar cross section of any object is given by [78]:

$$\sigma = \lim_{R\to+\infty} 4\pi R^2 \frac{P_{sc}}{P_{inc}} = \lim_{R\to+\infty} 4\pi R^2 \frac{|E_{sc}|^2}{|E_{inc}|^2} = \lim_{R\to+\infty} 4\pi R^2 \frac{|H_{sc}|^2}{|H_{inc}|^2}, \tag{2.22}$$

where R is the distance between the transmitter/receiver and the object, P_{sc} is the scattered power density and P_{inc} is the incident power density. The monostatic RCS measurement arrangement of on object is illustrated in Figure 2.19.

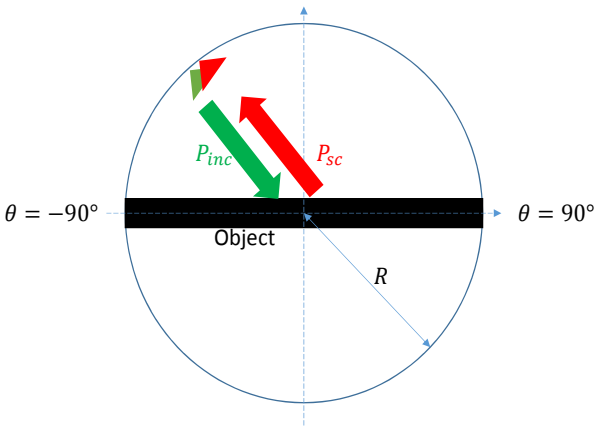

FIGURE 2.19: Monostatic RCS measurement arrangement.

For all the planar structures presented in Chapters 3, 4 and 5 in this thesis, the monostatic RCS is presented for angles between $-90°$ - $90°$ in cartesian form. In order to show the RCS reduction of the presented structures, their RCS are compared to a perfectly conducting plate of same size.

An example of the RCS of a 70 mm * 70 mm perfectly conducting plate at 8 GHz is given in Figure 2.20. CST Studio 2017 is used for the simulation and a linearly polarized TE wave is considered for the incident wave.

The maximum RCS of a perfectly conducting plate is given by:

$$\sigma_{max} = \frac{4\pi A^2}{\lambda^2}, \tag{2.23}$$

where A is the surface area of the plate. For a 70 mm * 70 mm perfectly conducting plate, at normal incidence σ_{max} = -6.68 dBm^2. In the simulated RCS (Figure 2.20), at normal incidence, σ_{max} = -6.68 dBm^2 thus validating our simulation procedure. The same procedure is used for all the planar structures presented in Chapters 3, 4 and 5.

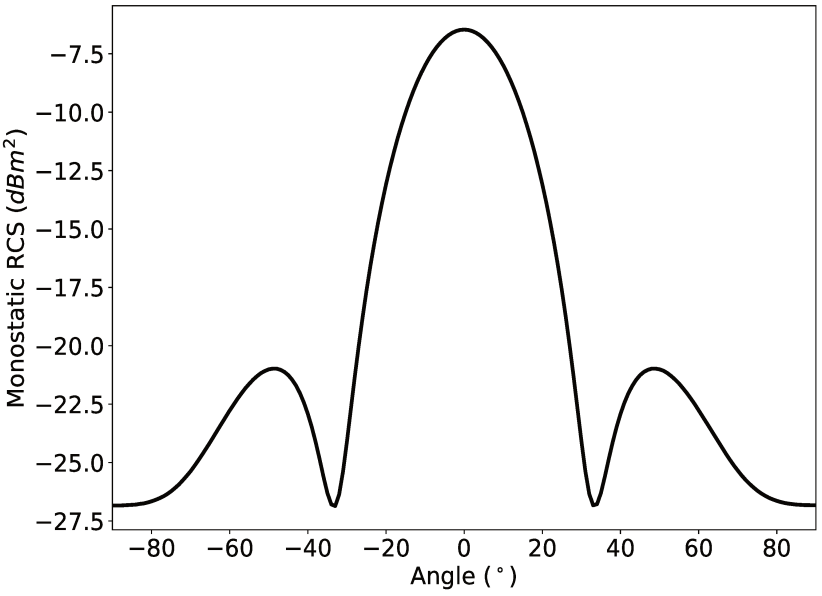

FIGURE 2.20: Monostatic RCS of a 70 mm * 70 mm perfectly conducting plate at 8 GHz.

2.4 Performance of radar absorbers

The performance of an absorber is often judged upon its -10 dB reflection or 50% absorption rate (Full Width at Half Maximum). These two criteria do not take into consideration the thickness of the absorber which can be the most important factor in some applications. A better method to evaluate the performance of an absorber is to use the -10 dB operational bandwidth to thickness ratio in order to evaluate the performance of EW absorbers. It seems that the bigger the ratio is, the better (in terms of performance) the absorber is. We consider this method better than the first two mentioned methods to evaluate the performance of absorbers. However, the problem with this approach is that that we can not compare the performance of two absorbers having exactly the same -10 dB frequency band and having exactly the same thicknesses. Also, with these approaches two absorbers must be compared only if, firstly, they have the same operating frequency range and different thicknesses or, secondly, same thicknesses and different operating frequencies. We often see comparison between radar absorbers which do not operate in the same frequency range and do not have the same thicknesses.

2.4.1 Theoretical thickness to real thickness ratio

We present a new approach to evaluate the performance of an absorber. According to [79], the minimum theoretical thickness, t, of a non magnetic absorber can be calculated by:

$$t \geq \frac{|\int_0^\infty ln|\rho(\lambda)|d\lambda|}{2\pi^2}, \tag{2.24}$$

where ρ is the module of the reflexion coefficient, λ is the wavelength in free space, and t is the theoretical minimum thickness required. This formula takes into account the exact reflexion, and the whole frequency range of the absorber (not the -10 dB frequency range). Our approach to evaluate the performance of a radar absorber consists of doing the ratio of the minimum theoretical thickness that the absorber must have to the real thickness of the structure. The minimum value of this ratio is very close to zero ($\approx 0\%$ in terms of percentage), and its maximum value is one (100% in terms of percentage). The closer to 100% the value is, the closer will be the thickness of the structure to its theoretical thickness. The advantage of this approach is that we will be able to compare the performances of absorbers which does not operate in the same frequency band as the minimum theoretical thickness to real thickness ratio is a ratio in which the thickness of an absorber is compared to its minimum possible thickness. The disadvantage of this approach is that the exact S parameters of the absorber must be known and can be time consuming to design and simulate absorbers that we want to compare. The performance of the previously presented magneto-dielectric radar absorber and the salisbury screen is given in Table 2.6.

Radar absorber	**Frequency** (GHz)	**Theoretical thickness,** t_T	**Real thickness,** t_R	(t_T/t_R)***100**
Magneto-dielectric	1 - 20	12.6 mm	25 mm	50.4 %
Salisbury screen	1 - 10	3.43 mm	15 mm	22.8%

TABLE 2.6: Performance of the magneto-dieletric radar absorber and the Salisbury screen. For the magneto-dielectric absorber, the thickness of the dielectric is of $\lambda/4$, $\mu_r = 1$ and $\epsilon_r = 1.392 - j1.1938$. For the Salisbury screen the resistive sheet's impedance is of 350 Ω/sq, $\mu_r = 1$, $\epsilon_r = 1$ and the thickness is of 15 mm. It is also important to note that column two corresponds to the frequency range in which the reflexion coefficients were integrated and not the -10 dB frequency range.

It can be seen from Table 2.6, that the theoretical thickness to real thickness ratio is of 50.4 % for the example of magneto-dielectric radar that has been considered. Similarly for the considered Salisbury screen, the theoretical thickness to real thickness ratio is of 50.4 22.8 %. We will show in Chapter 3, 4 and 5, that with the FSS based radar absorbers

developed in our work, a better theoretical thickness to real thickness ratio performance is obtained.

Chapter 3

THEORETICAL ANALYSIS FOR SYSTEMATIC DESIGN OF FSS BASED BROADBAND RADAR ABSORBERS

3.1 Introduction

As described in Chapter 2, one straight forward solution to design a radar absorber is to place a complex sheet (surface providing complex impedance) over a grounded dielectric substrate. The complex sheet is designed in a way that the whole structure matches the impedance of the free space ($Z_0 = 377\ \Omega$). Let us assume that we want to design a flexible broadband non magnetic absorber in the frequency range of 3.5 - 7 GHz which achieves at least -10 dB of reflection (at least 90% of absorption) in the given range. Three parameters are important for the design of the absorber: the thickness and permittivity of the dielectric substrate and the geometrical parameters of the complex sheet. By taking into account the facts that thick dielectrics are required for low frequency absorbers, that thick dielectrics are not always flexible, and that targets are not always planar, an efficient tool for the systematic design of flexible broadband radar absorbers using the Transmission Line Model (TLM) is presented in this work. Two approaches for designing the physical model of the absorber are presented. The first one consists of resistive square loops deposited on top of a dielectric, and the second one consists of metallic square loops associated with lumped resistors. More than 90% of absorption rate is obtained in the

required bandwidth for both transverse electric and transverse magnetic polarizations with the two approaches. The design concept provides a theoretical to real thickness ratio of 69.5% of the radar absorbers making the proposed design strategy extremely interesting. Finally, the required dimensions of flexible absorbers in some low frequency bands are given in order to show the versatility of the approach. The monostatic RCS of the proposed strcuture has also been simulated at some frequencies in the absorption band. It has been shown that the RCS reduces considerably with the absorber when compared to a planar conducting plane. In the following section our design strategy for the design of broadband absorption is discussed. The design of radar absorbers using the TLM method is a very powerful tool but, the litterature provides us the equivalent circuit model of simple resonating elements such as Square Loops and Jerusalem Cross Arrays [80]. Therefore, if the absorption bandwidth is to be broadened using more complex resonating elements, the design of radar absorbers using the TLM method can become very complicated. One option is to use genetic algorithms [81, 82, 83] to obtain the resonating element which will provide the required surface impedance, but one of the main problems with genetic algorithms is that they can be very long to provide expected results. Also, when lumped elements or resistive sheets are used, the fabrication cost of the structure considerably increases. This work has been published in Progress In Electromagnetics Research C and entitled 'Theoretical Analysis for Systematic Design of Flexible Broadband Radar Absorbers Using the Least-Square Method' [84].

3.2 Design strategy for broadband absorption

The strategy we adopt in this work is to achieve perfect absorption at f_{min} and f_{max} where f_{min} and f_{max} are the lower and upper limits of the desired frequency band respectively. To do so, the thickness must be selected such that the imaginary part of the required impedance, $Im(Z_{Req})$, have the same values at f_{min} and f_{max} but must be exactly out of phase. In this case we must observe $Im(Z_{Req})$ increasing from being negative to positive and $Re(Z_{Req})$ must have the same values at f_{min} and f_{max}. In our design goal, f_{min} = 3 GHz and f_{max} = 7.8 GHz, as shown in Figure 3.1, the 8 mm ($\lambda/7$ thin at the center frequency of 5.4 GHz) dielectric thickness satisfies the conditions described above. It can be observed with the red curves that $Im(Z_{Req})$ = -170 Ω at f_{min} and $Im(Z_{Req})$ = +170 Ω at f_{max}. Also, $Re(Z_{Req})$ = 118 Ω at both f_{min} and f_{max}.

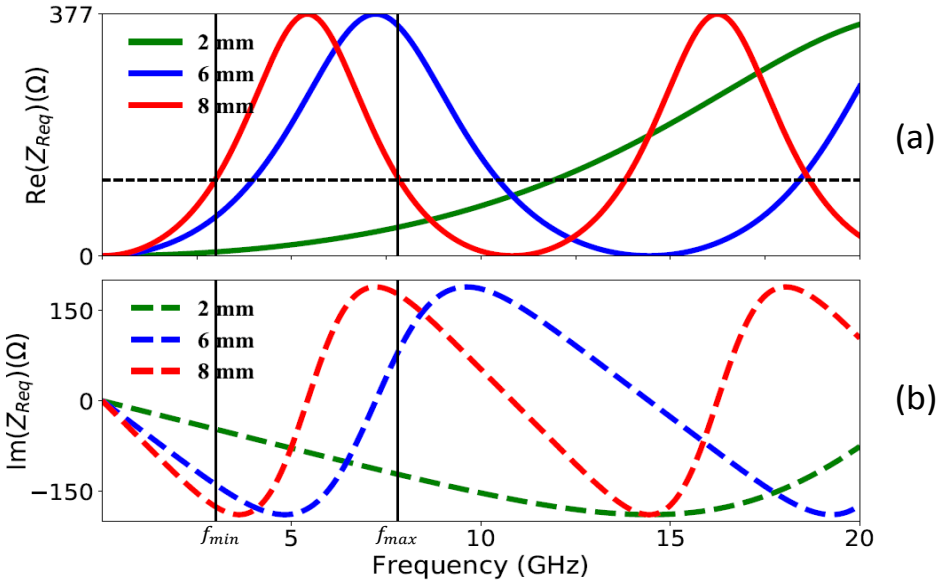

FIGURE 3.1: (a): Real part of required impedance of the complex sheet. (b): Imaginary part of required impedance of the complex sheet. The two solid vertical black lines represent the f_{min} = 3 GHz and f_{max} = 7.8 GHz limits which is our frequency band design goal. The required impedance have been plotted using Equations 2.8 - 2.10 of Chapter 2. Note that Z_{Req} was called Z_{sr} in Chapter 2.

As observed in Figure 3.1, $Im(Z_{Req})$ is both positive and negative between 3 - 7.8 GHz. The complex sheet must be both capacitive and inductive and must be the closest possible to $Im(Z_{Req})$. The TLM is hence given by a series of Resistance-Capacitor-Inductor (RLC) circuit in parallel of the 8 mm thick grounded transmission line as shown in Figure 3.2.

In the TLM of Figure 3.1, the resistance, R_s, will take into account the resistive losses ($Re(Z_{Req})$). The absorption optimization based on the losses will be discussed later. The impedance of a series RLC circuit is given by:

$$Z_{RLC} = R_s + j\frac{LC\omega^2 - 1}{C\omega}, \tag{3.1}$$

where ω is the angular frequency. As stated previously, we want to have perfect absorption at f_{min} and f_{max} in a first time. The imaginary part of Equation 3.1 must be equal to $Im(Z_{Req})$ at f_{min} and f_{max} leading to the following condition:

$$-C.Im(Z_{Req}).\omega + L.C.\omega^2 = 1 \tag{3.2}$$

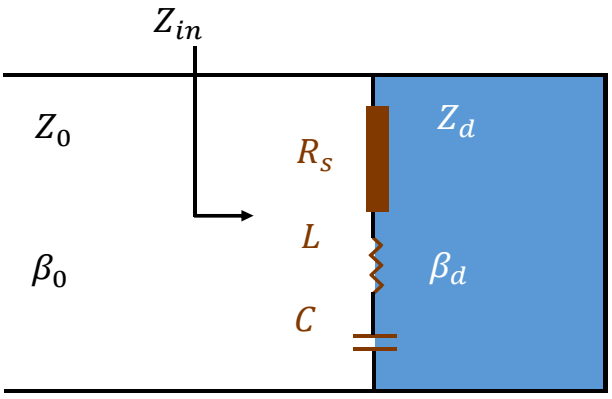

FIGURE 3.2: TLM model proposed for broadband absorption.

For simplicity we let $Im(Z_{Req})$=z_r. As z_r is frequency dependent, Equation 3.2 can be written in the following matrix form:

$$\begin{bmatrix} 1 \\ 1 \end{bmatrix} = \begin{bmatrix} -z_r(\omega_{min}).\omega_{min} & \omega_{min}^2 \\ -z_r(\omega_{max}).\omega_{max} & \omega_{max}^2 \end{bmatrix} \begin{bmatrix} C \\ LC \end{bmatrix} = \psi \begin{bmatrix} C \\ LC \end{bmatrix} \tag{3.3}$$

where ψ is a $(2 * 2)$ matrix. C and LC can be calculated using the least square method [85] such that it fits z_r:

$$\begin{bmatrix} C \\ LC \end{bmatrix} = (\psi^T \psi)^{-1} \psi^T \begin{bmatrix} 1 \\ 1 \end{bmatrix}, \tag{3.4}$$

where ψ^T is transpose of the matrix ψ. From Equation 3.4, the value of the capacitance is given by C directly and the value of L is given by LC/C. In our case, L = 5.84 nH and C = 0.186 pF are obtained. Figure 3.3 shows the imaginary part of the LC series impedance. It can be observed that the imaginary part of the complex sheet's impedance whose values of L and C has been calculated using Equation 2.8, is exactly the same as the required imaginary part of impedance at f_{min} and f_{max} validating Equation 2.8.

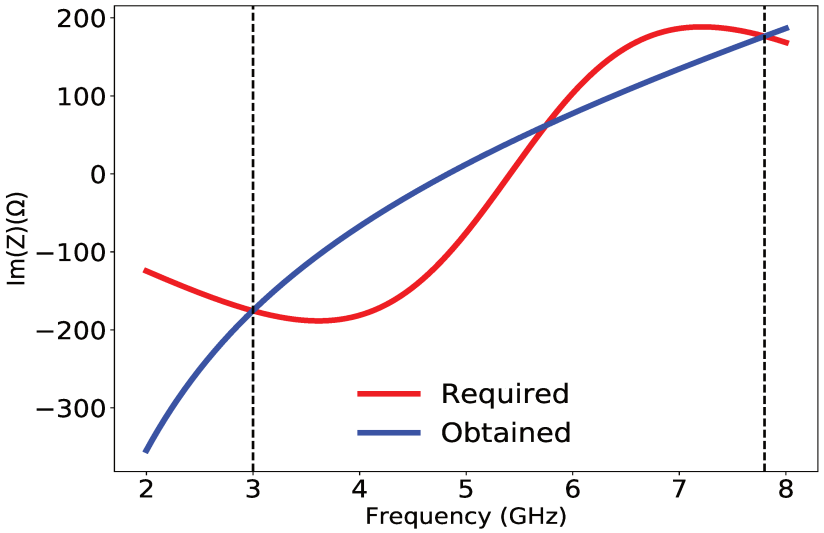

FIGURE 3.3: Comparison between required Im(Z) and calculated Im(Z) using Equation 2.8 of the LC model.

At this stage, all the TLM parameters of the absorber for a broadband absorption between 3 - 7.8 GHz are known. The thickness of the dielectric, h = 8 mm having $\epsilon_r = 3$. The initial resistance of the complex sheet, $R_s = 118\ \Omega$ and L and C values are of L = 5.84 nH and C = 0.186 pF respectively. By substituting Z_{RLC} of Equation 3.1 to Z_{sr} in Equation 2.9 (Chapter 2) and using Equation 2.11 (Chapter 2), the absorption rate of the TLM of the absorber is plotted in Figure 3.4 for different values of R_s.

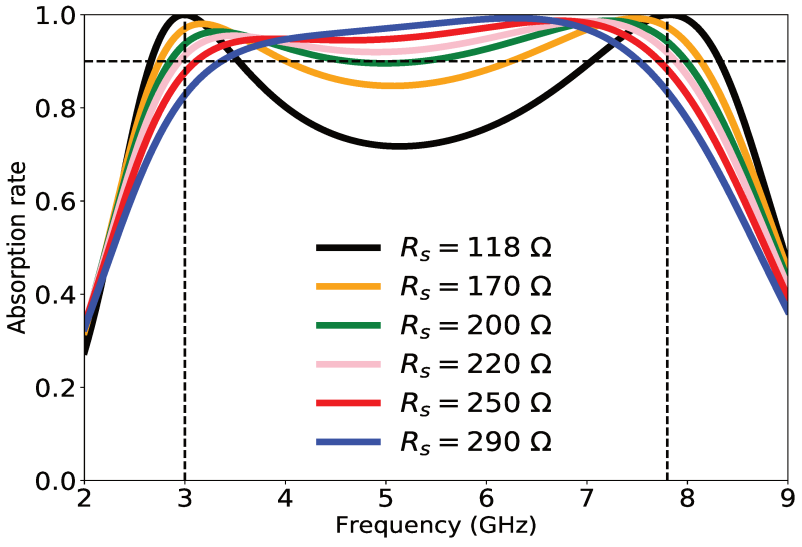

FIGURE 3.4: Absorption rate for different values of resistance.

It can be seen that with the initial value R_s, which is 118 Ω (black curve), perfect absorption is obtained at 3 GHz and 7.8 GHz respectively (as expected), but the absorption is less than 90% in the 3 - 7.8 GHz band. This result is logical as the RLC model has been matched at 3 GHz and 7.8 GHz respectively and not in the whole band. It can also be observed that when the complex sheet is made more lossy, by increasing the value of its real part (R_s), the absorption is enhanced and for values of R_s greater than 200 Ω, the absorption is at least of 90% in the whole band of 3 - 7.8 GHz. R_s cannot be increased infinitely since the bandwidth becomes very narrow, as it can be observed for $R_s = 290$ Ω in Figure 3.4. Thus R_s must be carefully selected. For our case, $R_s = 200$ Ω is selected as the absorption is at least of the 90% in the whole band of 3 - 7.8 GHz. To recapitulate, the final TLM parameters of the complex sheet impedance are: $R_s = 200$ Ω, L = 5.84 nH and C = 0.186 pF.

3.3 Physical model

Extensive research has been done on equivalent circuit models of FSS taking into consideration its geometry [86, 87, 88]. In this work, simple square loop arrays will be used to design the complex sheet in order to obtain an inductive and a capacitive response of L = 5.84 nH and C = 0.186 pF respectively. A well dimensioned infinite array of square loops can give a capacitive and inductive response and hence $Im(Z_{Req})$. The arrays of square loops have been designed as described in [88]. The relations between L and C values and the dimensions of the square loops can be found in [88] where the array is represented by a single series LC circuit shunted across a transmission line of impedance Z_0 (characteristic impedance of free space). An infinite thin array of narrow continuous perfectly conducting strips of period p has, for the incident field polarized parallel to the strips, a shunt inductive reactance given by:

$$\frac{X(\omega)}{Z_0} = F(p,\omega,\lambda) = \frac{p}{\lambda} cos(\theta) \left[ln\left(cosec \frac{\pi\omega}{2p} \right) + G(p,\omega,\lambda) \right], \tag{3.5}$$

where θ is the angle of incidence, λ is the wavelength and

$$G(p,\omega,\lambda) = \frac{1}{2} \frac{(1-\beta^2)^2 \left[(1-\frac{\beta^2}{4})(A_+ + A_-) + 4\beta^2 A_+ A_- \right]}{\left(1-\frac{\beta^2}{4}\right) + \beta^2 \left(1 + \frac{\beta^2}{4} + \frac{\beta^4}{8}\right)(A_+ + A_-) + 2\beta^6 A_+ A_-}, \tag{3.6}$$

where,

$$A_{+} = \frac{1}{\sqrt{1 \pm \frac{2psin(\theta)}{\lambda} - (\frac{pcos(\theta)}{\lambda})^2}} - 1 \tag{3.7}$$

and

$$\beta = \frac{sin(\pi\omega)}{2p} \tag{3.8}$$

The ractance X_L of the inductance L is given by:

$$\frac{X_L}{Z_0} = \frac{d}{p}(p, 2s, \lambda) \tag{3.9}$$

The susceptance B_C of the capacitance C is given by:

$$\frac{B_C}{Z_0} = 4\frac{d}{p}(p, g, \lambda), \tag{3.10}$$

where g is the gap between the loop sides. In order to get the required resistive response that is $Re(Z_{Req})$, the square loops can be made of ohmic sheets or of PEC including lumped resistances. By using the values of L, C and equations 3.5-3.10, the unit cell's period, p, has been calculated to be of 10 mm and the square array's length, d, has been calculated to be of 9.5 mm and width s equal to 0.15 mm. Figure 3.5 depicts the top view of the a unit cell of square loops placed on top of the 8 mm thick grounded dielectric.

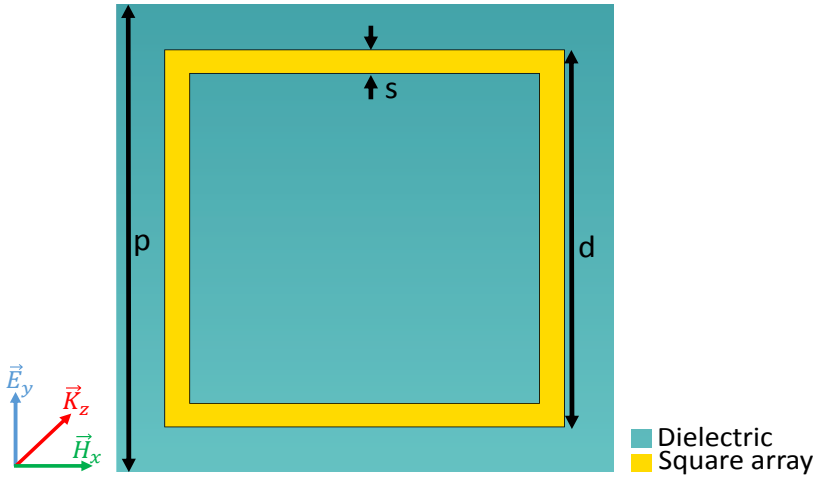

FIGURE 3.5: Top view of the unit cell of squared ohmic sheet placed on a 8 mm grounded dielectric.

3.3.1 Square arrays made of PEC with lumped resistors

For the first design, we will consider metallic (PEC) square arrays. As discussed in the design strategy subsection, the required real part of impedance must be around 200 Ω. Since PEC is not lossy, the the real part of the required impedance for absorption will not be achived and the absorption will be very small as shown in Figure 3.6.

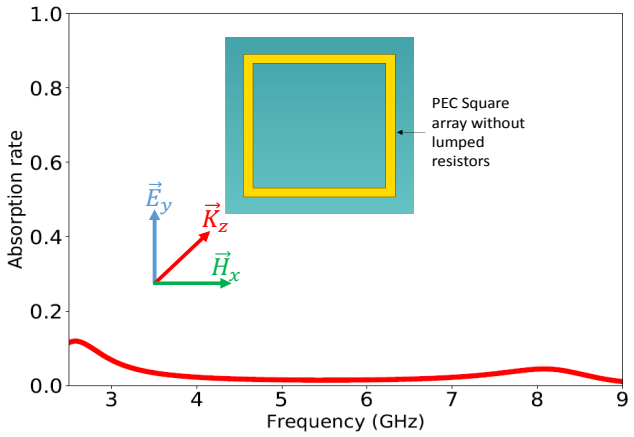

FIGURE 3.6: Simulated absorption rate of the radar absorber. The PEC square arrays are continuous (without lumped resistors). A normal incident linearly polarized TE wave is considered. Same results are obtained for TM mode.

For this reason, additional resistors (optimized value and number) must be added in the square arrays so that broadband absorption is obtained. Figure 3.8, represents the top view of the absorber. Furthermore, as we want to design a flexible absorber and want to use rubber as dielectric, one can not print the PEC square arrays on rubber. The proposed solution is to place 0.1 mm thick FR4 substrate (ϵ_r = 4.2 -j0.105) placed on top of a 7.9 mm grounded rubber ($\epsilon_r = 3$) substrate . The metallic square arrays are printed on the 0.1 mm thick FR4 substrate. In our case, the 0.1 mm thick FR4 being very small compared to the 7.9 mm thick rubber and their permittivity being close to each other, the overall effective permittivity is around $\epsilon_r = 3$. In Figure 3.7 the real part and imaginary part of the effective permittivity of a 0.1 mm thick FR4 substrate placed on top of a 7.9 mm thick rubber substrate has been retrieved and calculated as described in [89]. The effective permittivity can be observed to be around ϵ_{eff} = 3 - j0.

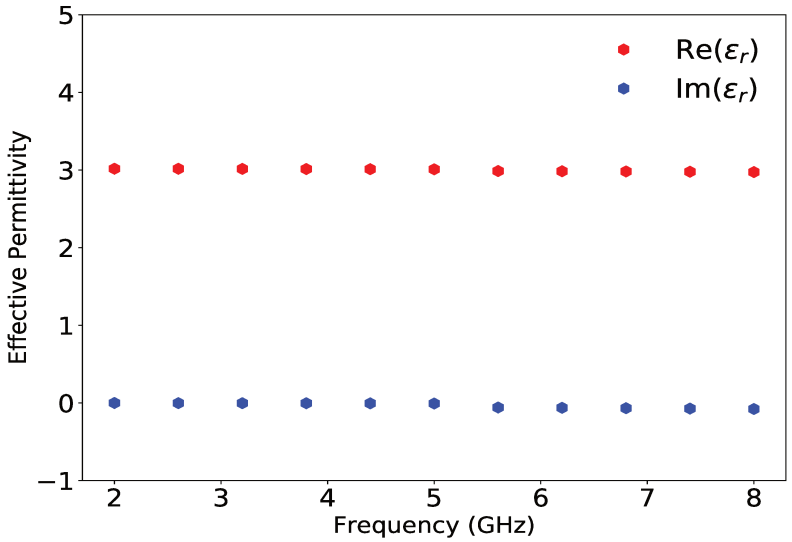

FIGURE 3.7: Retrieved real part (red curve) and imaginary part (blue curve) of the effective permittivity of a 0.1 mm thick FR4 substrate placed on top of a 7.9 mm thick rubber substrate.

The structure of the absorber is now a 0.1 mm thick FR4 substrate on which the square arrays are printed, placed on top of a 7.9 mm thick grounded rubber.

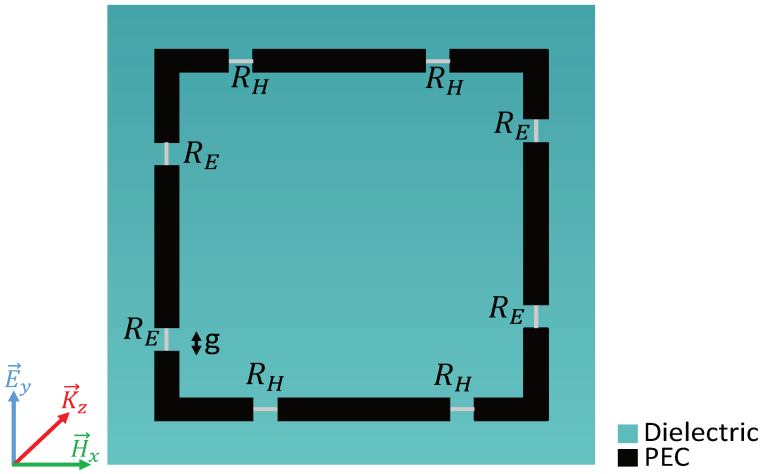

FIGURE 3.8: Top view of the unit cell of a PEC square array printed on FR4 substrate placed on top of a 7.9 mm grounded rubber dielectric.

The square arrays have the same dimensions p, d and s (as described earlier,p = 10 mm, d = 9.5 mm and s = 0.15 mm). Optimized gaps of dimension, $g = 1\ mm$ have been added in order to connect the resistors R_E and R_H. The resistors, R_E and R_H are set at 220 Ω. From Figure 3.4, it can be seen that for values of R_s between 200 - 250 Ω, the absorption

remains more than 90% in the 3 - 7.8 GHz range. Hence the surface impedance of the square loop including the lumped resistors can be between 200 - 250 Ω. The number of resistors in each arm of the square loops will give different surface impedances and absorption. In Figure 3.9, the absorption rate for different numbers of 220 Ω resistors is plotted. The simulation was done using CST Studio 2017. Periodic boundary conditions were applied in the numerical model in order to mimic a 2D infinite structure. Floquet ports were used for the excitation of the periodic structure. It must be noted that any value of resistor, R_s, can be chosen but the surface impedance of the square loop including the lumped resistors must be between 200 - 250 Ω.

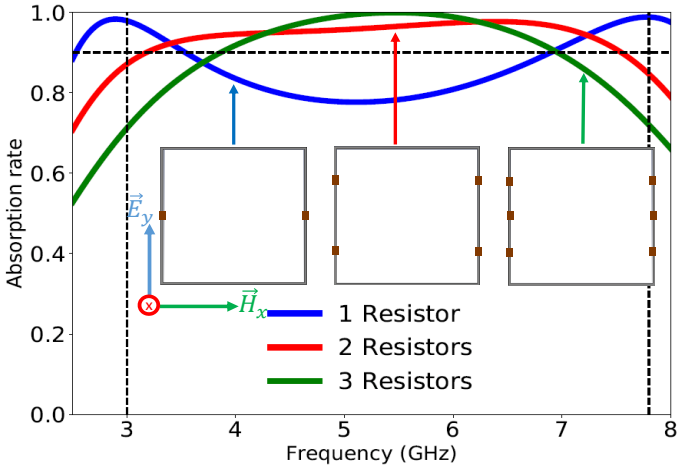

FIGURE 3.9: Absorption rate of the PEC with one, two and 3 resistors in the two vertical arms. The structures were simulated for linearly polarized TE wave.

Figure 3.9 shows the absorption rate of the square arrays with varying numbers of resistors in the vertical arms for the TE polarization case. It can be observed that for 1 resistor (blue curve) of 220 Ω in the two vertical arms, the absorption rate is more than 90% at 3 GHz and 7.8 GHz respectively but do not provide a surface impedance between 200 - 250 Ω. Following the same reasoning, two resistors (red curve) do provide the necessary surface impedance as the absorption rate is more than 90% in the whole band of 3 - 7.8 GHz (very slightly less in bandwidth but the resistors can be tuned and get a bandwidth of exactly 3 - 7.8 GHz). In the case when 3 resistors (green curve) are added, the surface impedance is very big compared to what is required and perfect absorption is obtained between 5 - 6 GHz but the bandwidth is reduced as we could have deduced from Figure 3.4. Thus two 220 Ω resistors in the two vertical arms are maintained in the designed of our broadband absorber for TE polarization. Our structure being perfectly symmetrical 220 Ω resistors are maintained on the horizontal arms of the square arrays for TM polarization.

For TE polarization, maximum currents flow on the vertical arms of the square arrays, and maximum currents flow in the horizontal arms for TM polarization as shown in 3.10.

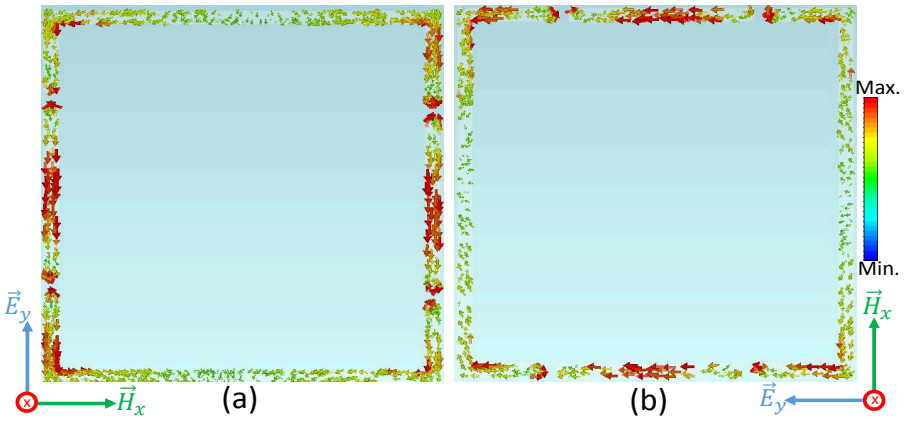

FIGURE 3.10: (a) Maximum currents flow on the vertical arms for TE polarization at 5.5 GHz. (b) Maximum currents flow on the horizontal arms for TM polarization at 5.5 GHz.

The resistors R_E bring the required losses for TE polarization and resistors R_H bring losses for TM polarization. Depending on which polarization we are working on, R_E or R_H can be removed from the arms on which currents are not flowing, must be made with continuous PEC (with no gaps, g). In some applications where both TE and TM are required, the gaps, g, must be optimized such that the imaginary part of the required impedance does not change significantly (as the gaps will bring some capacitive effects). Figure 3.11 depicts the simulated absorption rate of the structure for linearly polarized TE (a) and TM (b) waves under oblique incidences.

It can be seen from Figure 3.11, for both TE and TM polarizations, that for normal and oblique incidences of until 20°(red, blue curves) the absorption rate is more than 90% in the whole band of 3.09 - 7.7 GHz. These results are slightly less than 3 - 7.8 GHz band but the two resistors of each arms can be tuned around 220 Ω in order to have the exact bandwidth. The same trends are observed for higher incidences as in Section 3.3.2. These results also validate the proposed design strategy for broadband absorption.

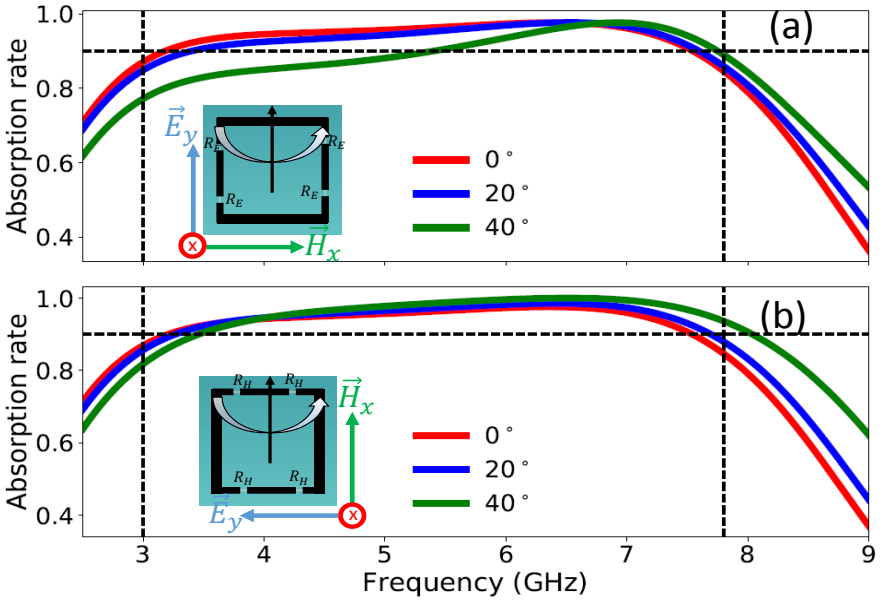

FIGURE 3.11: Absorption rate of the proposed structure under oblique incidences of 0 - 40°. (a) TE polarization. (b) TM polarization.

3.3.2 Square arrays made of resistive films

For the first design of the radar absorber using resistive films, the dimmensions p, d and g of the square loops the the dielectrics used are the same as in Section 3.3.1 (The unit cell has a period p of 10 mm and the square array has a length d of 9.5 mm and width s equal to 0.15 mm).

The relationship between the value of the required real part, $R_s = 200\ \Omega$, and the value of the resistive sheet is related by Equation 2.9 as described in [88].

$$R_s = R_{OhmicSheet}\frac{S}{A}, \tag{3.11}$$

where S is the surface area of the unit cell and A represents the elements along which currents propagate on the square loop. In our case, for Transverse Electric (TE) polarization, A is the surface area of the two vertical arms of the square loop, $S = 0.1\ mm^2$, $A = 2.85\ \mu m^2$, $R_s = 200\ \Omega$ and thus the resistance of our ohmic sheet, $R_{OhmicSheet} = 5.7\ \Omega$/Square. From Equation 3.11, we can see that the unit of the resistive sheet,$R_{OhmicSheet}$, is Ω, but

Ω/Square represents a special "square" situation yielding an answer in ohms. Ω/square is dimensionally equal to an ohm, but is exclusively used for sheet resistance.

The simulation was done using CST Studio 2017. Periodic boundary conditions were applied in the numerical model in order to mimic a 2D infinite structure. Floquet ports were used for the excitation of the periodic structure. Figure 3.12 depicts the simulated absorption rate of the structure for linearly co-polarized TE and TM waves under oblique incidences.

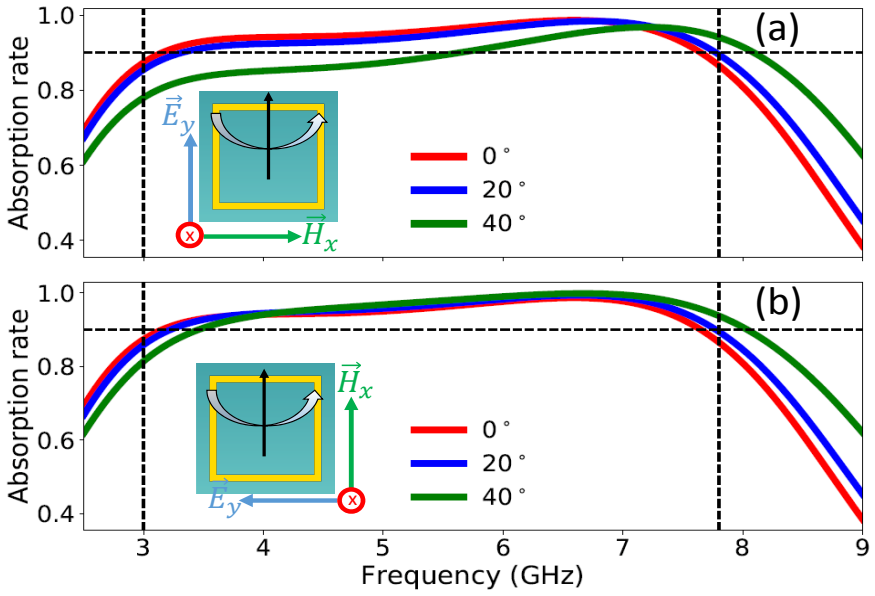

FIGURE 3.12: Absorption rate of the proposed structure under oblique incidences of 0 - 40°. (a) TE polarization. (b) TM polarization.

From Figure 3.12, it can be observed that for both TE and TM polarizations, that for normal incidence and oblique incidences of until 20°(red and blue curves) the absorption rate is more than 90/% (less than -10 dB of reflection) in the whole band of 3 - 7.8 GHz which was our design goal. Results for incidence angles of until 40° (green curve) shows that the absorption band decreases but remain interesting. The absorption rate for TE and TM polarizations are the same for normal incidence as the square arrays are completely symmetrical along x and y axes. These results validates the proposed design strategy as more than 90% of absorption is obtained in the whole band of 3 - 7.8 GHz.

3.3.3 Examples and performance

In order to show the versatility of the proposed design plan, the methods used in Section 3.2 have been applied to some low frequency bands. Table 3.1 shows the TLM elements required for at least 90% of absorption in these desired frequency bands. In each case rubber ($\epsilon_r = 3$) was selected as dielectric whose thickness is given in column 2 of Table 3.1. We have purposely selected some low frequency bands for which the dielectric thickness is not negligible and classical dielectrics are not flexible for large thicknesses. For the cases studied in the table below, slabs of 10 mm thick flexible rubber can be put on top of each other making the whole system flexible.

TABLE 3.1: TLM model elements for flexible absorbers in some low frequency bands.

Example	Desired Band (GHz)	Thickness (mm)	R_s (Ω)	L (nH)	C (pF)
1	$0.3 - 0.6$	90	250	77.18	1.69
2	$0.5 - 0.9$	60	250	52.6	1.09
3	$1 - 2.4$	25	250	19.85	0.52

TABLE 3.2: Dimensions of physical model of radar absorbers using square loop arrays made of resistive sheets for the same bands as in Table 3.1.

Example	Desired Band (GHz)	$R_{OhmicSheet}$ (Ω/square)	p (mm)	d (mm)	s (mm)
1	$0.3 - 0.6$	0.86	80	75	0.147
2	$0.5 - 0.9$	1.2	60	55	0.160
3	$1 - 2.4$	1.43	25	24	0.127

In order to design the square loop arrays with PEC using lumped resistors, the dimensions of p, d and s remain the same as in 3.2. Two lumped resistors of 220 Ω must be added to each arm as described in Section 3.3.1. The PEC square loops must be printed on a 0.1 mm FR4 substrate (or any other substrate but the overall effective permittivity must be around 3) as explained in 3.3.1.

The theoretical thickness of the proposed absorber achieving more than 90% of absorption in the whole band of 3 - 7.8 GHz is of 5.56 mm (calculated as described in Chapter 2). As the real thickness is 8 mm, the theoretical to real thickness ratio in this case is of 69.5%. The theoretical to real thickness ratio of the proposed absorber is better than

the magneto-dielectric absorber (50.4%) and the Salisbury screen (22.8%) described in Chapter 2.

3.3.4 Monostatic radar cross section of the absorber

The monostatic radar cross section of the structure has been simulated for the 3 - 8 GHz band in CST Studio 2017 using the same configuration described in Chapter 2. The simulated structure was 7 cm * 7 cm containing 7 * 7 square loops. The RCS of the radar absorber is compared to RCS of a 7 cm * 7 cm reference metallic plate. The simulated monostatic RCS of the radar absorber and the metallic plate at 3 GHz, 4GHz, 5 GHz, 6 GHz, 7 GHz and 8 GHz is presented in Figure 3.13. CST Studio 2017 has been used for the simulations and a linearly polarized TE wave is considered.

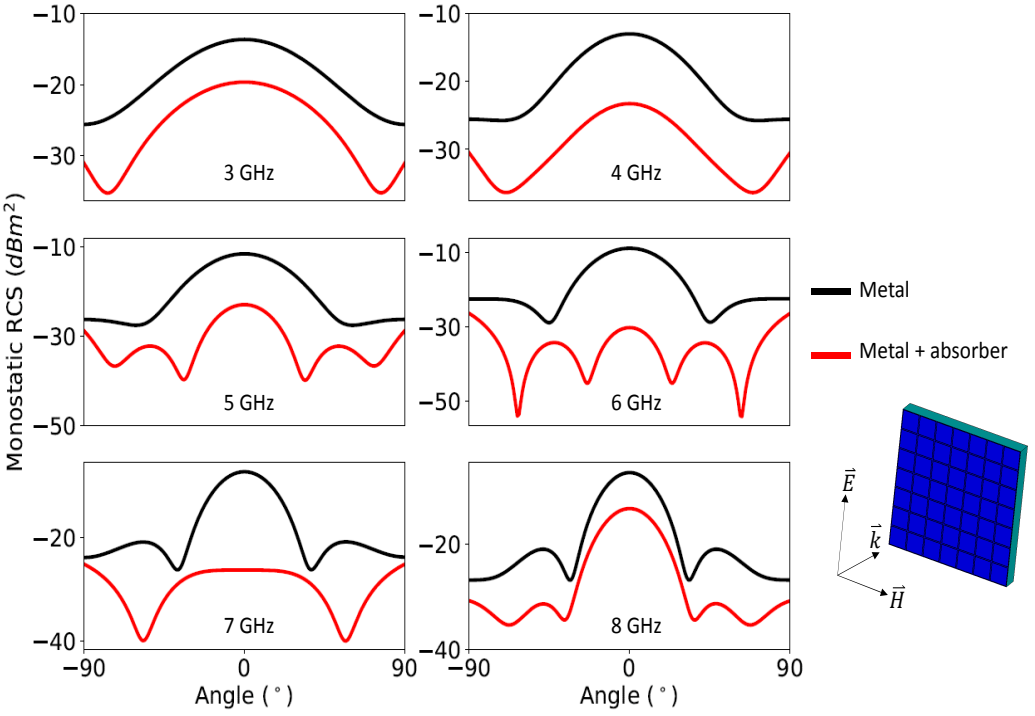

FIGURE 3.13: Co-polarization Monostatic RCS for 3, 4, 5, 6, 7 and 8 GHz of the absorbing stucture and a reference metallic plate of the same dimensions.

It can bee seen from Figure 3.13 that when for the proposed absorbing stucture the monostatic RCS considerably reduces for all oblique incidences between $-90°$ - $90°$ in the whole

band of 3 - 8 GHz. When only themetallic plate is considered the co-polarized monostatic RCS for normal icidence is of -13.4 dBm^2, -12.8 dBm^2, -11.5 dBm^2, -8.7 dBm^2, -7.3 dBm^2 and -6.6 dBm^2 at 3, 4, 5, 6, 7 and 8 GHz respectively. The co-polarization monostatic RCS of the proposed grounded radar absorber at normal incidence reduces to -19.6 dBm^2, -23.3 dBm^2, -23.1 dBm^2, -30 dBm^2, -26.4 dBm^2, -13.4 dBm^2 for 3, 4, 5, 6, 7 and 8 GHz respectively. The cross-polarization RCS monostatic RCS, shown in Figure 3.14 is very small (around -90 dB) for the cases when the metallic alone is considered and when the grounded radar absorber is is considered. These results validate our structure for broadband reduction of RCS.

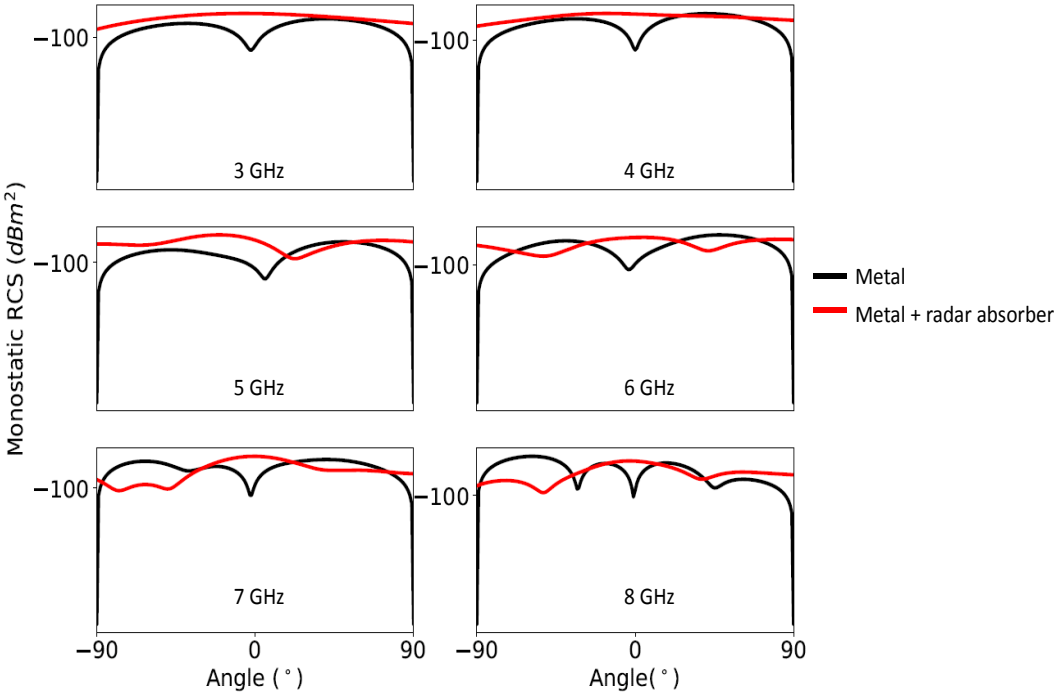

FIGURE 3.14: Cross-polarization Monostatic RCS at 3, 4, 5, 6, 7 and 8 GHz of the absorbing stucture and a perfecty conducting plate of the same dimensions.

Table 3.3 recapitulates all the the monostatic RCS ressults described above for normal incidence.

Object	Co-Polarization RCS at 3, 4, 5, 6, 7 and 8 GHz in (dBm^2)	Cross-Polarization RCS at 3, 4, 5, 6, 7 and 8 GHz in (dBm^2)
Reference metal plate	-13.4, -12.8, -11.5, -8.7 , -7.3 and -6.6	$\approx$ -90
Radar absorber	-19.6, -23.3, -23.1, -30 , -26.4 and -13.4	$\approx$ -90 $\approx$ -90

TABLE 3.3: Recapitulation of monostatic RCS results.

3.4 Conclusion

In this chapter, a simple but powerful analytical tool to design broadband flexible radar absorbers for any frequency band using the TLM is presented. Firstly, the expressions to calculate the required real and imaginary parts of impedances for broadband absorptions for any dielectric permittivity and thickness are given. The real part of the required impedance has been associated to a resistance and the imaginary part has been associated to an inductor and a capacitor in series. A simple matrix formulation is used to get the values of L and C that fits the required imaginary part of the impedance at the lower and upper limits of the frequency band. We have shown that broadband absorption can be achieved by increasing the value of the resistance in the TLM. Finally, once all the parameters of the TLM model found, two physical model approaches using square arrays to design the absorber are described. The first approach is to use printed metallic square arrays on a grounded dielectric substrate. The dimensions of the arrays and the unit cell will give the required imaginary part of impedance. The real part of the impedance is obtained by including lumped resistors in the arms of the square arrays. The second approach consists of using resistive sheets patterned as square arrays. As for the first approach, the dimensions of the arrays and the unit cell will give the required imaginary part of impedance. The required real part of impedance is given by the resistance value of the resistive films. In both cases the square arrays being symmetrical, broadband absorptions for both linearly polarized TE and TM modes are obtained. Also the proposed absorbers achieve as high as 88% for the 90% absorption rate band to center frequency ratio and a theoretical to real thickness ratio of 69.5% making the proposed design strategy extremely interesting. The monostatic RCS of the proposed strcuture has also been simulated at some frequencies in the absorption band. It has been shown that the RCS reduces considerably with the absorber when compared to a metallic plate. When only the metallic plate is considered

the monostatic co-polarization RCS for normal icidence is of -13.4 dBm^2, -12.8 dBm^2, -11.5 dBm^2, -8.7 dBm^2, -7.3 dBm^2 and -6.6 dBm^2 at 3, 4, 5, 6, 7 and 8 GHz respectively. When the proposed grounded absorber is considered, the monostatic co-polarization RCS at normal incidence reduces to -19.6 dBm^2, -23.3 dBm^2, -23.1 dBm^2, -30 dBm^2, -26.4 dBm^2, -13.4 dBm^2 for 3, 4, 5, 6, 7 and 8 GHz respectively. The cross-polarization RCS of the metallic plate with and without the radar absorber have also been simulated, and in both cases, the cross-polarization RCS is found to be very small (around -100 dB). As discussed in the introduction, the design of radar absorbers using the TLM method is a very powerful tool but, the litterature provides us the equivalent circuit model of simple resonating elements and if the absorption bandwidth is to be broadened using more complex resonating elements, the design of radar absorbers using the TLM method can become very complicated. Also, when lumped elements or resistive sheets are used, the fabrication cost of the structure considerably increases. In the next chapter, our work on a single layer MM broadband radar absorber is described and it will be shown if better performance can be obtained with more complicated MM and FSS.

Chapter 4

A SINGLE LAYER BROADBAND RADAR ABSORBER

4.1 Introduction

In chapter 3, we have designed radar absorbers using the TLM. The required surface impedance have been designed using an equivalent RLC circuit model. Losses of the radar absorber are obtained mainly with the resistor (of the RLC model) and the bandwidth is mainly fixed with the the inductor and the capacitor. Well optimized resonating elements of MM or FSS (without the use of lumped elements) can provide electric and magnetic resonances such that the impedance of the structure matches with the impedance of air in a broad frequency range. In this chapter, a single layer co-polarization broadband radar absorber is presented. Under normal incidence, it achieves at least 90% of absorption from 5.6 GHz to 9.1 GHz for both TE and TM polarizations. Our contribution and the challenge of this work is to achieve broadband absorption using a very thin single dielectric layer. Broadband absorption is achieved by multiple resonances provoked by rotating the resonating element by 45°. An original optimized Underlined U shape (UUSR) has been developed for the resonating element which provides a broadband co-polarization absorption. The structure is 12.7 times thinner than the wavelength at the center frequency. Firstly, the main design methodologies of the unit cell is described. Numerical and measured absorption rate results are then presented and discussed. Then the absorption meachanism is described by the study of electric fields, magnetic fields (at the

three near unity absorption frequencies) and some parametric studies. As it will be seen in the Design section, the resonator (only the metallic UUSR) is rotated by 45° and due this rotation the cross-polar absorption is not significant. Depending on applications, not achieving cross-polar absorption is more or less critical. Inside radomes of military vessels for example, cross-polar absorption is not often required for the reduction of electromagnetic interference. Nevertheless, it has been shown by simulation results that when whole structre is configured in a 'chessboard' manner, the cross-polarization issue can be overcome and the the RCS can consederably reduced. The RCS of both the normally arranged full structure and the 'chessboard' configured full structure has been simulated for the three near unity absorption peak frequencies and it has been shown that both structures considerably reduces the co-polarization RCS when compared to a planar metallic plate and that the cross-polarization RCS reduction of the 'chessboard' configured full structure is better than that of the the can of the normally arranged full structure. This work has been published in mdpi Materials journal and entitled 'A co-polarization broadband radar absorber for RCS reduction' [47] and has been presented in IEEE EUCAP 2018 and IEEE CAMA 2018 international conferences.

4.2 Methodology for the design of the unit cell

The objective is to design a radar absorber achieving at least -10 dB of reflection in the range of 5 -10 GHz. The first step is to choose the dielectric and its thickness. As we want an easily avaliable dielectric we chose FR4 dielctric substrate having a permittivity of 3.92 and loss tangent of 0.025. In order to fix its thickness we can use the -10 dB thickness limit described in [79]. According to [79], a radar absorber must have a mimimum thickness in order to achieve at least -10 dB of reflection and is given by 4.1:

$$h_{min} = \frac{|ln(\rho_0)|(\lambda_{max} - \lambda_{min})}{2\pi^2}, \tag{4.1}$$

where h_{min} is the minimum thickness required for a minimum reflection given by ρ_0 in the range λ_{max} and λ_{min}. The wavelength in free space at the lower frequency(f_{min}) is given by λ_{max} and λ_{min} is the wavelength in the free space at the higher frequency (f_{max}).

In our case, in order to achieve at least -10 dB of reflection in the range of 5 -10 GHz, the minimum calculated thickness is of 1.8 mm. If we want to use cheap FR4, some standard thicknesses such as 1.6 mm and 3.2 mm are easily available. Thus we choose a grounded FR4 having a thickness of 3.2 mm as dielectric substrate. As discussed in Chapters 2 and

3, the required impedance (Re(Z_{req}) and Im(Z_{req})) of a grounded dielectric for absorption in a given range can be calculated based of the TLM. Figure 4.1 shows the required impedance for absorption in the range of 5 - 10 GHz of a grounded 3 mm thick FR4 dielectric.

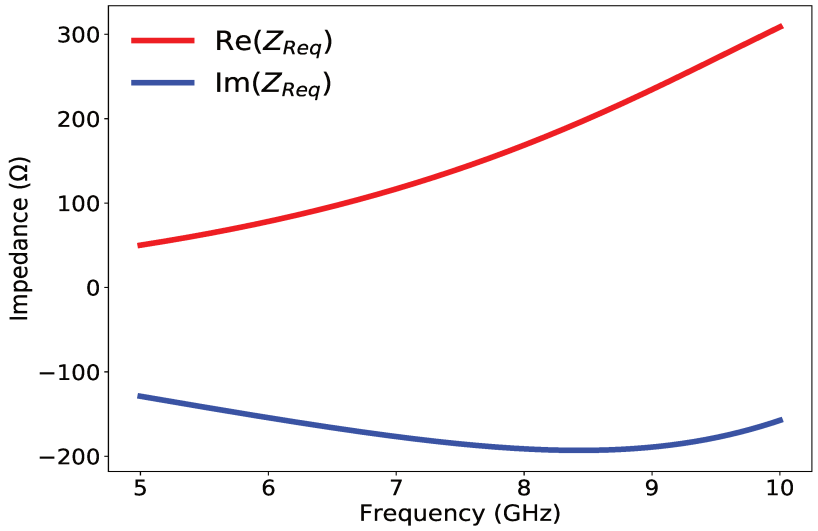

FIGURE 4.1: Required real (Re(Z_{req})) and imaginary (Im(Z_{req})) parts of surface impedance for perfect absorption of a 3.2 mm FR4 grounded dielectric substrate having a permittivity of 3.92 and loss tangent of 0.025. A normally incident linearly polarized TE wave is considered.

It should be noted that positive values of the imaginary parts mean an inductive coupling is taking place and negative values mean that a capacitive coupling is taking place. Im(Z_{req}) being negative, the surface impedance required is capacitive and can be written in the form $1/jC\omega$. C is the value of the equivalent capacitance. Hence the resonant element that is to be designed, must provide à capacitive coupling in the whole range of 5 - 10 GHz. The 'U' shape resonator is well known for providing capacitive coupling [91, 92, 93], but in the quest of multiple resonances, our aim is to design a new capacitive resonating element.'U' shape resonators can provide a capacitive coupling due to their two arms. Our first choice is to implement a 'U' shape resonator. As th 'U' shape resonator is not symetrical, it does not provide the same absorption response for TE and TM modes as shown in Figure 4.2. The segments excited by the electric field (blue points on the resonator in the inset of Figure 4.2) is not the same as the segments excited by the magnetic field (green points on the resonator in the inset of Figure 4.2). Hence, the absorption rates for TE represented by the blue curve and TM represented by green curve are not the same. Moreover, broadband

absorption is not achieved. It must be noted that the dimensions of the unit cell are given later in this subsection as we are only describing the main ideas of our methodology here.

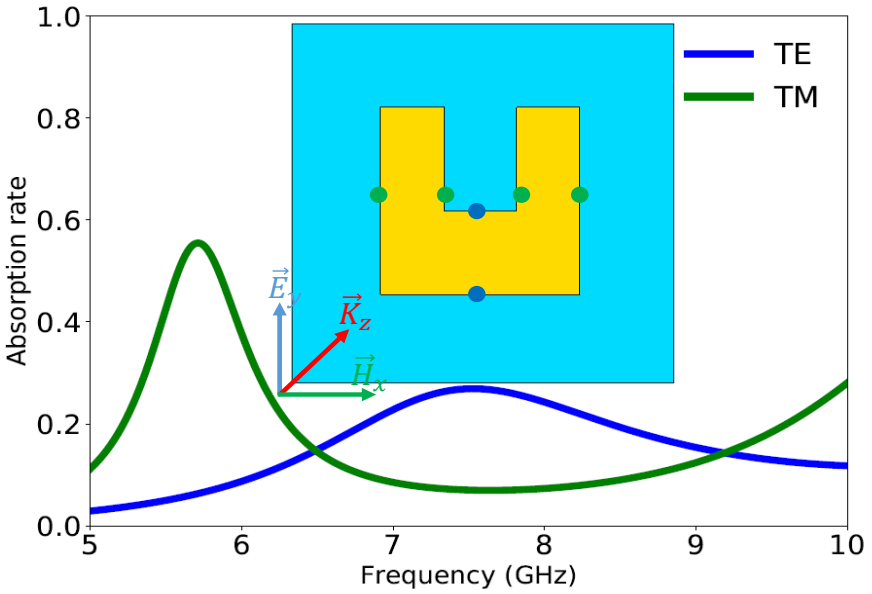

FIGURE 4.2: Absorption rates for normally incident linearly polarized TE and TM waves. Simulations were performed using the commercial software CST Design Studio Suite 2017. Periodic boundary conditions were applied in the numerical model in order to mimic a 2D infinite structure.

One way to make the 'U' shape resonator symetrical when excited by the E and H fields is to rotate it by 45° as shown in the inset of Figure 4.3. This strategy has been adopted in some recent works such as [90] . In this case the structure becomes more interesting as the electrical and magnetic field interact with exactly the same segments of the resonator as seen in the ninset of Figure 4.3. TE and TM modes become equal as shown by red and blue curves of Figure 4.3. Furthermore, the absorption is considerably increased and broadened. The absorption mechanism is described later in this chapter.

The problem with structures having rotated resonating elements is that the cross polarization absorption is small (as shown in Figure 4.3) but as discussed earlier, depending on applications, not achieving cross-polar absorption is more or less critical.

In order to increase further the absorption rate (as we want more than 90% in the range of 5 - 10 GHz) new resonances may be created by adding an optimized strip line as shown in the inset of Figure 4.4(case 1). The absorption results for both TE and TM linearly polarized waves of the absorber is presented for two cases (rotated resonator and unrotated

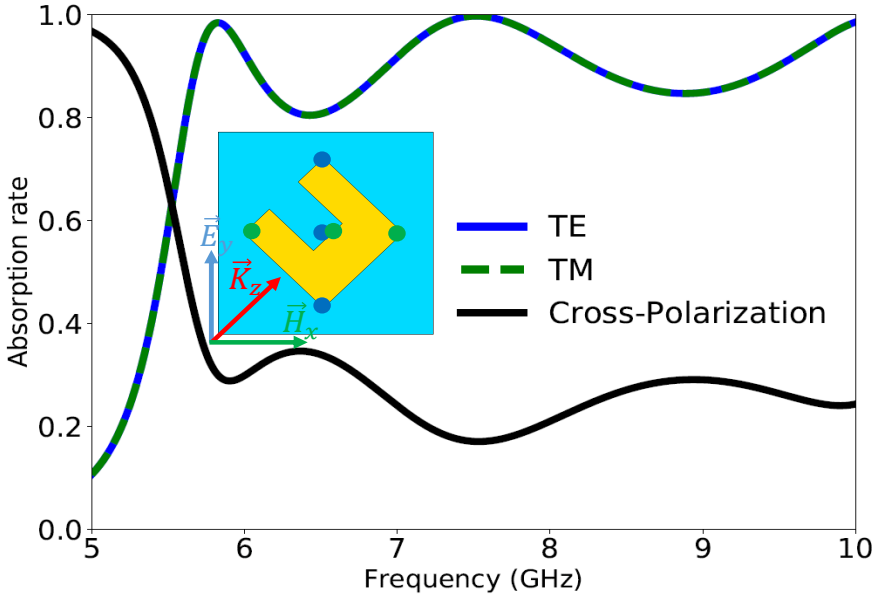

FIGURE 4.3: Absorption rates for normally incident linearly polarized TE and TM waves. Cross-polarization absorption is also shown. Simulations were performed using the commercial software CST Design Studio Suite 2017. Periodic boundary conditions were applied in the numerical model in order to mimic a 2D infinite structure.

resonator) in Figure 4.4. From Figure 4.4, it can be observed that the absorption rate is more than 90% in the whole range of 5.6 GHz to 9.1 GHz for both TE and TM modes when the resonator is rotated. This final structure is thus retained for the final unit cell. The first case (Case 1) represents the unrotated UUSR and the second case (Case 2) represents the UUSR rotated by 45°.

For the first case (Case 1 of Figure 4.4), when the UUSR is not rotated the segments of the patch (UUSR) excited by the electric field (blue points on the patch) is not the same as the segments excited by the magnetic field (green points on the patch). Hence, the absorption rates for TE represented by the green curve and TM represented by orange curve are not the same. Moreover, broadband absorption is not achieved. Therefore, the patch oriented as in case 1 is not efficient. When the UUSR is rotated by 45°, as in Case 2 of Figure 4.4, the structure becomes more interesting as the electrical and magnetic field interact with exactly the same segments of the patch. TE and TM modes become equal as shown by red and blue curves. Furthermore, the absorption is considerably increased and broadened.

The final dimensions of the 'U' resonator and the whole unit cell is obtained by heavy

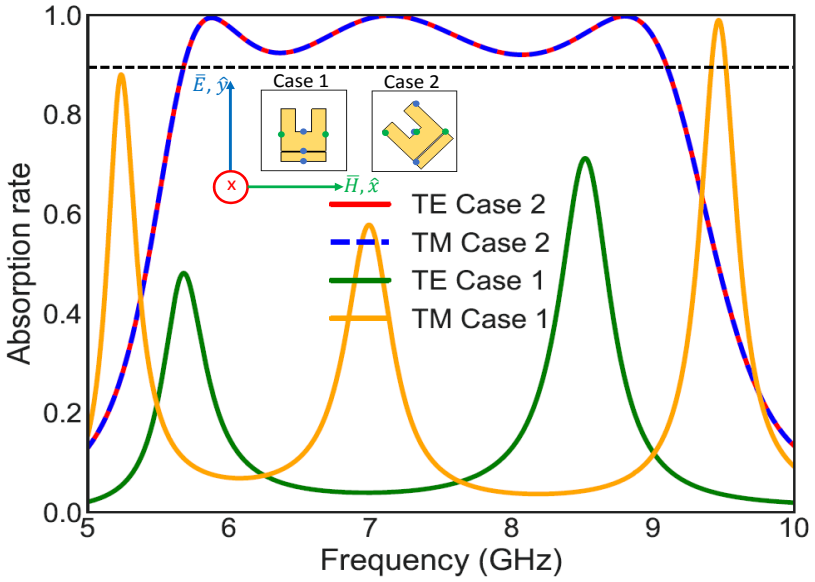

FIGURE 4.4: Absorption rates for linearly polarized TE and TM waves for Case 1 and Case 2. Simulations were performed using the commercial software CST Design Studio Suite 2017. Periodic boundary conditions were applied in the numerical model in order to mimic a 2D infinite structure.

parametric studies (for which the goal is to enhance magnetic and electric couplings) using CST Studio 2017. The final unit cell of the absorber is illustrated in Figure 4.5. It consists of a metallic Underlined U Shaped Resonator (UUSR) deposited on a metal backed FR4 dielectric. The UUSR is axially rotated by 45°. The FR4 dielectric is 3.2 mm thick and is backed with metal to prevent transmission. A 0.017 mm thin copper having electric conductivity of $5.8 * 10^7$ S/m was used for the UUSR and to back the FR4. The FR4 has a permittivity of 3.92 and loss tangent of 0.025. The unit cells are arranged in periods of P = 15 mm. Numerical design and simulations were performed using the commercial software CST Design Studio Suite 2017. Periodic boundary conditions were applied in the numerical model in order to mimic a 2D infinite structure. The dimensions in milliliters (mm) are as follows. W1 = 2.5, W2 = 7.85, W3 = 1.8, W4 = 2.85, W5 = 7.85, W6 = 8, W7 = 0.175, L = 4.35, P = 15 and h = 3.2. The USSR is centered at (x = -0.112611, y = 0.112611).

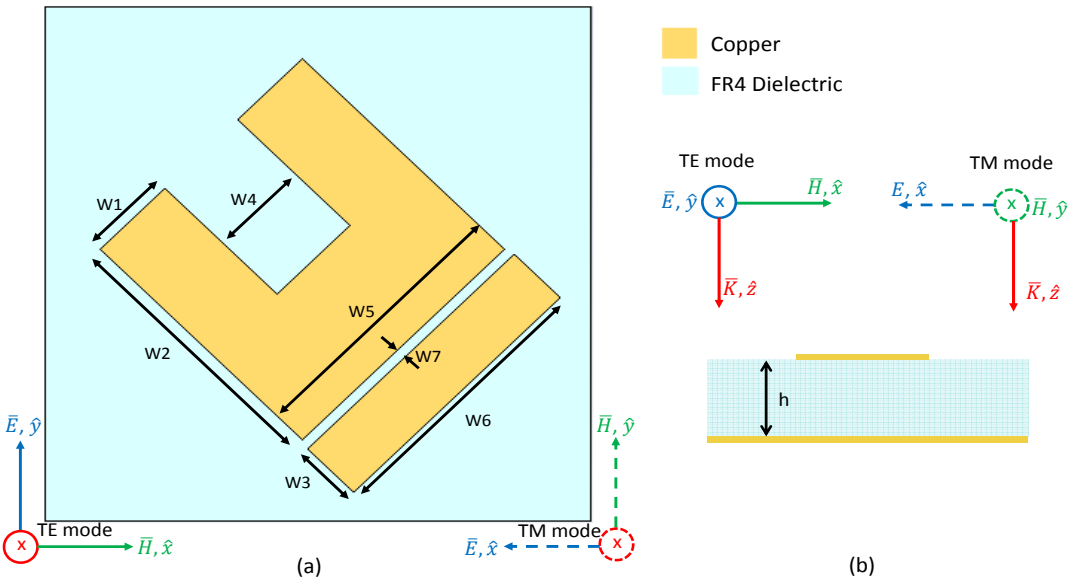

FIGURE 4.5: (a).Top view of the unit cell of the proposed absorber.(b) Cross sectional view of the unit cell.

4.3 Results

4.3.1 Simulated and measured absorption rates

The co-polarization and cross-polarization refelction under normal incidence of linearly polarized TE and TM waves are presented in Figure 4.6(a). Their absorptions are presented in Figure 4.6(b). The co-polarization absorption rates for normal and oblique incidences of linearly polarized TE and TM waves of our structure are presented in Figure 4.6(c) and (d) respectively. Firstly, we can see that the cross polar absorption rate is not significant (high reflectivity under cross-polarization). This is due to the rotation of the UUSR. Secondly, concerning co-polarization absorption rates for both TE and TM polarizations, for normal incidence and oblique incidences until 20°, the absorption rate is more than 90% in the whole range of 5.6 GHz – 9.1 GHz frequency band. The absorption rate is more than 85% and 77% for 30° and 40° respectively. Numerical designs and simulations were performed using the commercial software CST Design Studio Suite. Periodic boundary conditions were applied in the numerical model in order to mimic a 2D infinite structure. Floquet ports were used for the excitation of the periodic structure. Simulation results were plotted using a free mathematical programming language tool. Three near unity

absorption peaks have been observed at 5.86 GHz, 7.16 GHz and 8.82 GHz and are be used to understand the absorption mechanism in the next section.

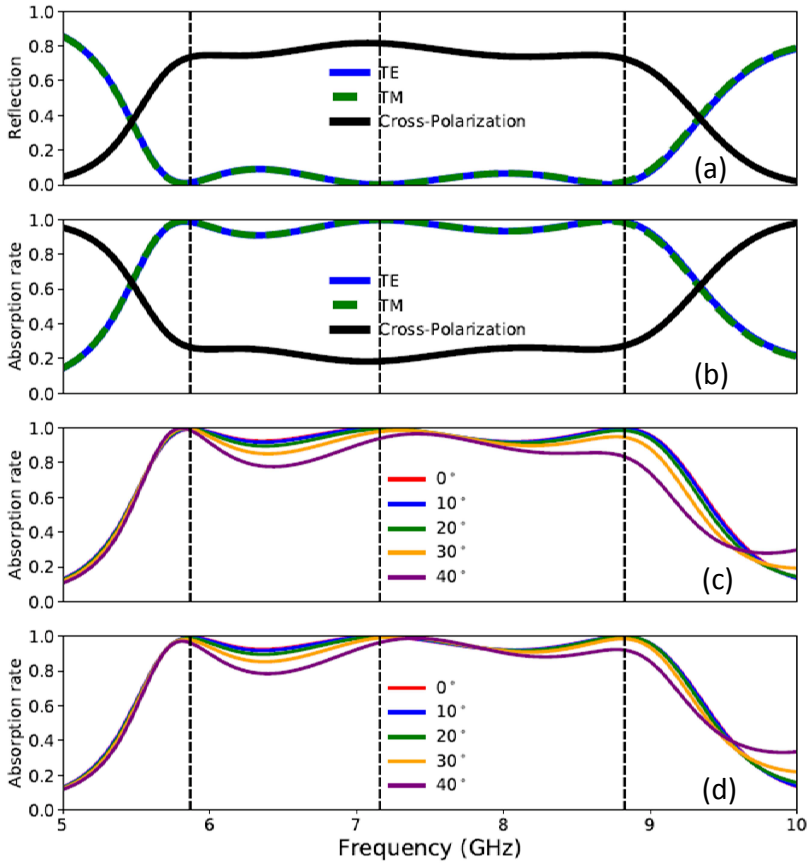

FIGURE 4.6: (a) Co-polarized reflection for normally incident linearly polarized TE and TM waves. The Cross polarization reflection is also shown. (b) Co-polarized absorption rate for normally incident linearly polarized TE and TM waves. The Cross polarization absorption is also shown. (c) Absorption rate of the proposed structure under oblique incidences of 0 - 40° for TE polarization. (d) Same configuration as (c) but for TM polarization.

An experimental prototype with dimensions of 300 mm * 300 mm and consisting of 19 * 19 unit cells was fabricated using conventional Printing Circuit Board (PCB) technology as shown in the inset of Figure 4.7. Measurements have been done in an anechoic chamber using a vector network analyzer. Two broadband FLANNR® horn antennas working in the 2-18 GHz frequency band are used as emitter and receiver in reflection configuration. The reflection coefficient is normalized using a sheet of copper as reflecting mirror. For a linearly polarized TE wave the simulated (solid green line) and measured (red circles) amplitudes of the absorption rate under normal incidence are plotted in Figure 4.7. Good agreement in terms of bandwidth and absorption rate is reported between simulation and

measurement. For the measured absorption rate, the slight shift of the whole frequency band towards lower frequencies can be explained by the fact that the exact value of the permittivity of the fabricated FR4 dielectric. Simulations have shown that a small variation of the value of FR4 (for example 4 instead of 3.92) shifts the whole frequency band towards lower frequencies.

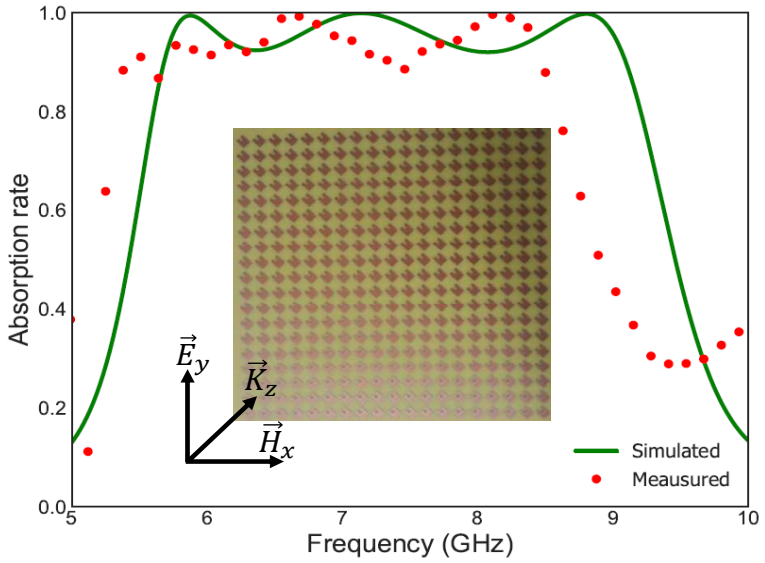

FIGURE 4.7: In red circles, the measured absorption rate is plotted and in green the simulated absorption rate is shown. Both are plotted under normal incidence for linearly polarized TE waves.

4.3.2 Absorption Mechanism

As described in Chapter 2, the required surface impedance (real and imaginary parts) for perfect absorption of a grounded dielectric can be calculated. The required surface impedance of a 3.2 mm grounded dielectric having a permittivity of 3.92 and loss tangent of 0.025 is plotted in the Figure 4.8.The actual surface impedance of the UUSR is also given in Figure 4.8. The surface impedance of the UUSR has been extracted from CST Studio 2017.

It can be observed from Figure 4.8 that the real part of impedance of the UUSR ($\mathrm{Re}(Z_s)$) is very close to zero which is logical as the UUSR is made of copper. It should be noted that positive values of the imaginary parts mean an inductive coupling is taking place and negative values mean that a capacitive coupling is taking place. In our case, $\mathrm{Re}(Z_s)$ being

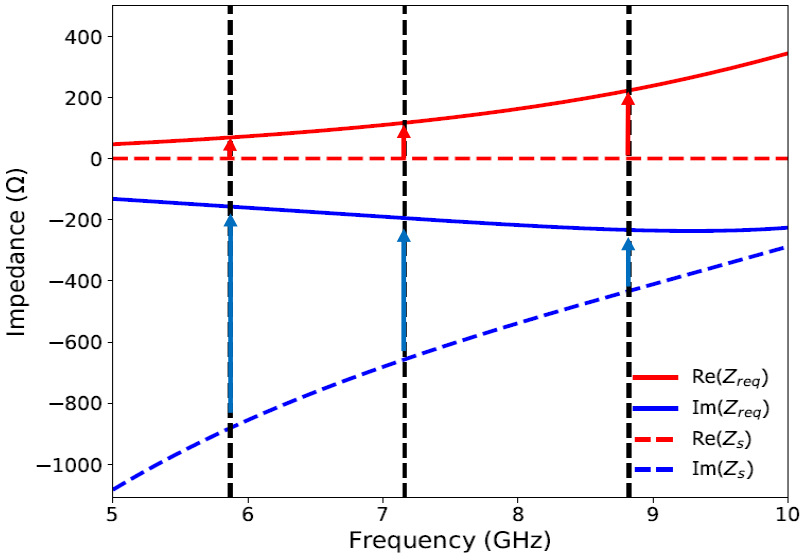

FIGURE 4.8: Required real (Re(Z_{req})) and imaginary (Im(Z_{req})) parts of surface impedance for perfect absorption of a 3.2 mm FR4 grounded dielectric and actual real (Re(Z_s)) and imaginary (Im(Z_s)) parts of the impedance of the UUSR.

very close to zero and Im(Z_s) being negative, the surface impedance Z_s is capacitive and can be written in the form $Z_s = 1/\mathrm{j}C\omega$. C is the value of the equivalent capacitance. For a good absorption (if not perfect), Re(Z_s) and Im(Z_s) must be as close as possible to Re(Z_{req}) and Im(Z_{req}) respectively. For broadband absorption, firstly, an inductive coupling is required such that Im(Z_s) increases and becomes close to Im(Z_{req}) and secondly losses must be introduced such that Re(Z_s) increases and becomes close to Re(Z_{req}). Placing the UUSR on top of the metal backed lossy FR4 dielectric substrate will increase both Re(Z_s) and Im(Z_s). The real part of the surface impedance, Re(Z_s) will be increased as the dielectric substrate is lossy and the inductive coupling to increase Im(Z_s) will be produced by anti parallel currents between the UUSR and the ground plane provided that the dielectric is very thin compared to the wavelength. Obviously, electric coupling is also induced in the structure. The figure below depicts the electric and magnetic fields at the three near unity absorption peaks.

For the first near-unity absorption frequency at 5.86 GHz, the electric fields are mainly produced around regions A and B. The magnetic fields are caused by the anti-parallel currents (not shown in the paper) flowing at regions E. At 7.16 GHz, the electric fields are created by regions A and C. The magnetic fields are mainly provoked by the anti-parallel currents flowing at region F and the ground plane. For the final near unity absorption

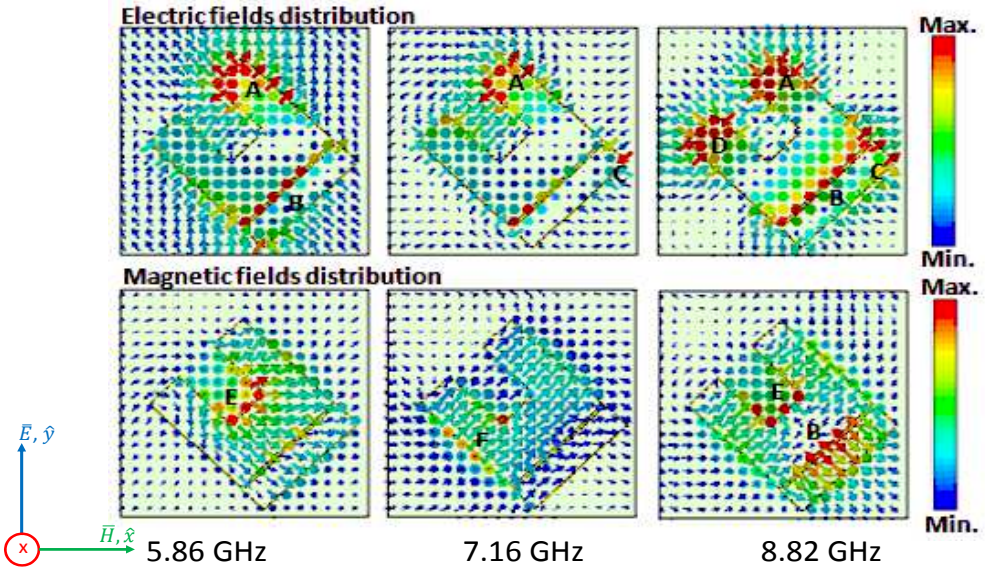

FIGURE 4.9: Distribution of electric and magnetic fields on the absorber at 5.86 GHz, 7.16 GHz and 8.82 GHz for a linearly polarized TE wave. Different labelled regions correspond to regions where maximum electric or magnetic fields have been observed.

peak at 8.82 GHz, the electric fields are mainly produced around regions A, B, C and D. The magnetic fields are introduced by the anti-parallel currents flowing at regions E, B and the ground plane and also by the anti parallel currents flowing between the bottom of the UUSR shape and the top of the strip line. The coupling of electric and magnetic fields led to near unity absorption. As we can observe for the three frequencies, the electric fields are, among others, confined around region A (right hand of the UUSR). Decreasing the length, L1, of the right hand of USSR should decrease the absorption in the whole band. We can check this by tuning the length, L1, of the right hand of the UUSR. It has been observed that the capacitance increases and while L1 decreases. Thus the absorption rate is deteriorated when L1 decreases as shown In Figure 4.10 (a).The magnetic fields around region B contributed to the third absorption peak only. No magnetic fields were found around region B for the first and second absorption peaks. Thus, modifying the distance between the strip line and the U shape will affect only the third absorption peak as shown in Figure 4.10 (b).

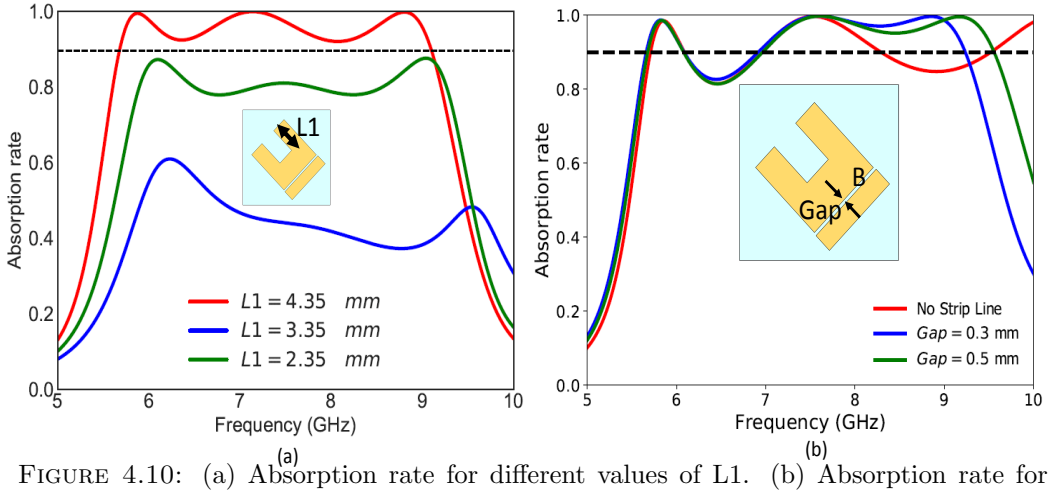

FIGURE 4.10: (a) Absorption rate for different values of L1. (b) Absorption rate for different values of the gap. An illumination of linearly polarized TE wave is considered.

The selection of dielectric thickness is a very important parameter in the design of a broadband absorber as we have described in the methodology subsection. Increasing the thickness of an absorber does not necessarily increase the absorption bandwidth. What is more important is that the surface the parallel combination of the UUSR impedance and the grounded dielectric impedance matches the impedance of air. Moreover different thicknesses of grounded dielectrics will required different impedances (Re(Z_{Req}) and Im(Z_{Req})) for efficient absorption and this requiredifferent type of coupling. Figure 4.11 depicts the absorption rate for different thicknesses. An illumination of linearly polarized TE wave is considered.

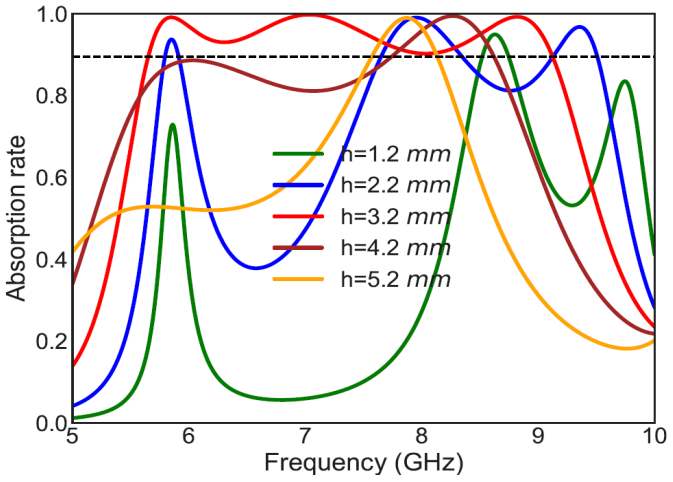

FIGURE 4.11: Absorption rate for different values of thickness (h). An illumination of linearly polarized TE wave is considered.

4.3.3 Monostatic RCS of the proposed radar absorber

The monostatic RCS of the full strucrure has been simulated using CST Studio 2017 and a linearly polarized TE wave is considered with same configurations as described in Chapter 2. Figure 4.12(b) shows the simulated RCS of the full structure (Figure 4.12(a)) at the three frequencies where near unity absorption peaks have been obtained (5.87 GHz, 7.16 GHz and 8.82 GHz). The simulated structure is 12 cm * 12 cm. The RCS of the radar absorber is compared to the RCS of a 12 cm * 12 cm reference metallic plate. The simulated co-polarization and cross-polarization monostatic RCS of the radar absorber and the metallic plate are shown.

It can bee seen from Figure 4.12(b) that when the proposed grounded absorbing stucture is considered, the co-polarization monostatic RCS considerably reduces for normal incidence but it sometimes increases for some oblique incidences between $-90°$ - $90°$. When only the reference metallic plate is considered the monostatic co-polarization RCS for normal incidence is of 0 dBm^2, 1.7 dBm^2 and 3.6 dBm^2 for 5.87, 7.16, and 8.82 GHz respectively. When the proposed grounded absorbing stucture is considered, the monostatic co-polarization RCS at normal incidence reduces to -11.3 dBm^2, -13.6 dBm^2 and -10.9 dBm^2 for 5.87, 7.16, and 8.82 GHz respectively. On the contrary the monostatic cross-polarization RCS of the grounded radar absorber is bigger for all angles and all frequencies than when the reference metallic plate alone is considered. When only the

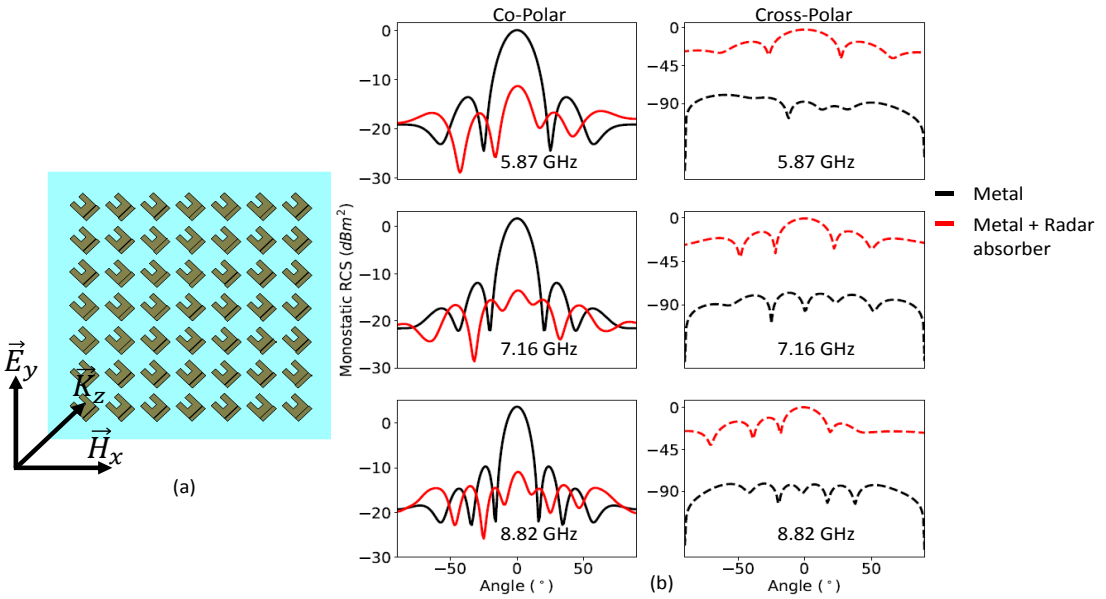

FIGURE 4.12: (a) Similated normally arranged full structure. (b) Monostatic RCS for 5.87, 7.16 and 8.82 GHz of the absorbing stucture and a perfecty conducting plate of the same dimensions. The first column represents co-polarization RCS results and the second column represents results for coss-polarization RCS.

reference metallic plate is considered the monostatic cross-polarization RCS for normal incidence is around -90 dBm^2 at 5.87, 7.16, and 8.82 GHz. The monostatic cross-polarization RCS at normal incidence increases to -2.27 dBm^2, 0 dBm^2 and 0 dBm^2 for 5.87, 7.16, and 8.82 GHz respectively for the grounded metallic plate. In brief, we have shown that when our whole structure is arranged in a normal periodic manner (as shown in Figure 4.12 (a)), the co-polarization monostatic RCS reduces considerably for normal incidence but the cross-polarization monostatic RCS increases considerably.

As we deduced earlier, the cross-polarization monostatic RCS is quite big due to the 45° rotation of the UUSR. Depending on applications, this can be more or less crucial. When these type of structures are placed in a 'chessboard' configuration, the cross-polarization to RCS or absorption can be enhanced as shown in [90]. The monostatic RCS of the 'chessboard' configured full structure has been simulated using CST Studio 2017 and a linearly polarized TE wave is considered. The simulated 'chessboard' configured full structure for the RCS is depicted in Figure 4.13(a). The simulated structure is 12 cm * 12 cm. The RCS of the radar absorber is compared to the RCS of a 12 cm * 12 cm reference metallic plate. The simulated co-polarization and cross-polarization monostatic RCS of

the radar absorber and the metallic plate at 5.87 GHz, 7.16 GHz and 8.82 GHz (where near unity absorption peaks have been obtained) are presented in Figure 4.13(b).

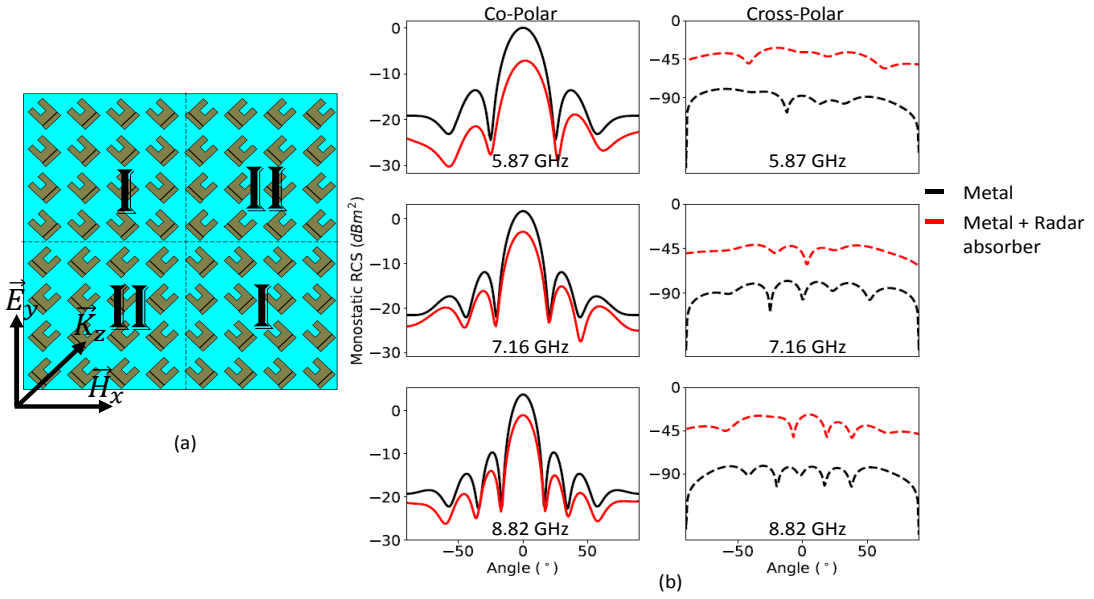

FIGURE 4.13: (a) Similated 'chessboard' configured full structure. (b) Monostatic RCS for 5.87, 7.16 and 8.82 GHz of the absorbing stucture and a perfecty conducting plate of the same dimensions. The first column represents co-polarization RCS results and the second column represents results for coss-polarization RCS.

From Figure 4.13(b), it can be seen that when the proposed grounded absorbing stucture is considered, the co-polarization monostatic RCS considerably reduces for for all oblique incidences between $-90°$ - $90°$. When only the reference metallic plate is considered the monostatic co-polarization RCS for normal incidence is of 0 dBm^2, 1.7 dBm^2 and 3.6 dBm^2 for 5.87, 7.16 and 8.82 GHz respectively. When the proposed grounded absorber is considered, the monostatic co-polarization RCS at normal incidence reduces to -7.1 dBm^2, -2.9 dBm^2 and -1.1 dBm^2 for 5.87, 7.16 and 8.82 GHz respectively. On the contrary, as for the normally organised full structure, the monostatic cross-polarization RCS of the grounded radar absorber is bigger for all angles and all frequencies than when the conducting plane alone is considered but in this case the monostatic cross-polarization RCS reduction is better than for the normal structure. When only the reference metallic plate is considered the monostatic cross-polarization RCS for normal incidence is around -90 dBm^2 at 5.87, 7.16 and 8.82 GHz. For the grounded radar absorber, the monostatic cross-polarization RCS at normal incidence increases to -36.1 dBm^2, -59.5 dBm^2 and -28.3 dBm^2 for 5.87, 7.16 and 8.82 GHz respectively. We have shown that the 'chessboard' configured

structure can overcome the problem of cross polarization absorption when compared to the normally arranged full structure. Table 4.1 below recapitulates all the the monostatic RCS ressults described above for normal incidence.

Object	Co-Polarization RCS at 5.87, 7.16, and 8.82 GHz in (dBm^2)	Cross-Polarization RCS at 5.87, 7.16, and 8.82 GHz in (dBm^2)
Reference metal plate	0, 1.7 and 3.6	$\approx$ -90
Normally arranged radar absorber	11.3, -13.6 and -10.9	-2.27, 0 and 0
'chessboard' configured radar absorber	-7.1, -2.9 and -1.1	-36.1, -59.5 and -28.3

TABLE 4.1: Recapitulation of monostatic RCS results.

4.4 Conclusion

A single layer low profile radar absorber exhibiting more than 90% of absorption in the whole band of 5.6 GHz to 9.1 GHz has been presented in this work. The proposed structure consists of an Underlined U Shape Resonator (UUSR) deposited on a dielectric. We have described the main lines of the methodology of how we designed the structure and we have discussed the absorption mechanism by studying a general and simple TLM model and the distribution of electric and magnetic fields. The simple TLM puts in light the required coupling for efficient absorption. A prototype of the absorber was fabricated and measurement results are in good agreement with numerical results. Due to the proposed original UUSR resonating element, a theoretical to real thickness ratio (described in Chapter 2) of 61% is obtained making the proposed UUSR very competitive and useful for future works. One very important limitation of the proposed absorber (when the full structure is configured normally) is that the absorber is not suitable for cross polarization absorption due to the shape of the UUSR. It has been shown by simulation results that when whole structre is configured in a 'chessboard' manner, the cross polarization issue can be overcome and both co and cross polarization RCS can considerably be reduced. The RCS has been calculated for the three near unity absorption peak frequencies and it has been shown that the proposed structure considerably reduces the RCS when compared to a planar reference metallic plate. When only the reference metallic plate is considered the monostatic co-polarization RCS for normal incidence is of 0 dBm^2, 1.7 dBm^2 and 3.6 dBm^2 at 5.87, 7.16, and 8.82 GHz respectively. When the normally arranged grounded full structure absorber is considered, the RCS monostatic co-polarization at normal incidence reduces to reduces to -11.3 dBm^2, -13.6 dBm^2 and -10.9 dBm^2 for 5.87, 7.16, and 8.82

GHz respectively. In this case the cross-polarization RCS with the radar absorber is quite big. When the structure is arranged in a 'chessboard' configuration the co-polarization RCS of the radar absorber is reduced when compared to a metallic plate and the most noticable result is the cross-polarization RCS which is very low when compared to the normally arranged full structure. In the next chapter, in order to further enlarge the bandwidth, a two layered radar absorber is presented.

Chapter 5

A DUAL LAYER BROADBAND RADAR ABSORBER

5.1 Introduction

In Chapter 4, we have presented an FSS based single layer broadband radar absorber. The resonating element of the stucture provides sufficient electric and magnetic resonances for co- polarization broadband absorption. No genetic algorithms or lumped elements for additional losses were used. As discussed in Chapter 2, in order to further enlarge the bandwidth, two popular techniques used, consist of incorporating resonating elements working at nearby frequencies [94, 95, 72, 96] by arranging then on the same plane or by using multi layers [97, 98, 99]. Both techniques lead to a drop in the absorption (sometimes the reflection, $S_{11} > -10$ dB) at certain frequencies in the bandwidth. Using several elements on the same plane is very difficult to implement due to lack of space in a small unit cell. Moreover, using different resonating elements on a single unit cell can lead to an asymmetrical design and hence degrading the performance considerably for oblique incidences and different polarizations. By following the same reasoning a multilayer structure can considerably increase the total thickness of the absorber. Using well customized magnetic materials [100], can decrease the thickness [79] but they can be very expensive as discussed in Chapter 2. For these reasons, designing thin broadband radar absorbers with easily available dielectrics especially for low frequencies (VHF/UHF) and the gigahertz regime (radio frequency and microwave) is very complicated and is a challenging topic. In this chapter a thin broadband dual-layer radar absorber based on periodic FSS to reduce the RCS of planar targets is described in this chapter. The proposed structure consists of

periodically arranged metallic patterns printed on two dielectric substrates separated by an optimized air gap. Under normal incidence, the proposed structure exhibits at least 89.7% of absorption in the whole band of 4.8 GHz to 11.1 GHz for both TE and TM polarizations. For oblique incidences, a very slight decrease in the bandwidth is observed in the upper frequency band until 30° and the absorption remains very interesting for higher incidences. The structure is $\lambda/7.2$ (λ is the wavelength in free space) thin compared to the center frequency (8.2 GHz). In addition, parametric studies have demonstrated that at least 90% of absorption can be produced with our structure by adjusting the thicknesses of the dielectric substrates. In this chapter, firstly, the main design methodologies of the unit cell is described. Numerical and measured absorption rate results are then presented and discussed. Then the absorption meachanism is described by the study of electric fields, magnetic fields and the power loss density (at the three near unity absorption frequencies). As in Chapter 4, the designed resonator of the first layer is rotated by 45° and due this rotation the cross-polar absorption is not significant. Thus two cases of monostatic RCS of the full structure of the radar absorber are presented. The first case is when the first layer is organized periodically (normally) and the second case is for the 'chessboard' configured first layer. It has been shown by simulation results, as in Chapter 4, that when whole structre is configured in a 'chessboard' manner, the cross polarization issue can be overcome and the the RCS can consederably reduced. The RCS of both the normally arranged full structure and the 'chessboard' configured full structure has been simulated for the three near unity absorption peak frequencies and it has been shown that both structures considerably reduces the co-polarization RCS when compared to a reference planar metallic plate and that the cross-polarization RCS reduction of the 'chessboard' configured full structure is better than that of the the can of the normally arranged full structure. This work has been published in mdpi Materials journal and entitled 'A co-polarization broadband radar absorber for RCS reduction' [47] and has also been presented at IEEE EUCAP and IEEE CAMA international conferences.

5.2 Methodology for the design of the unit cell

The dual layer broadband radar absorber presented in this chapter has been inspired from our work on a single layer broadband absorber presented in Chapter 4. In what follows, some important methodologies of how our final structure has been obtained is described. Our objective is to design a broadband radar absorber in the range of 4 - 11 GHz using two layers. Our first layer is based on our work on Chapter 4. Instead of using a 'U' resonator (Figure 5.1 (a)) we have used a 'Half Moon' resonator (Figure 5.1 (b)) which is

very similar to the 'U'. The reasons for using the 'Half Moon' resonator is that it does not have edges like the 'U'. These edges contibute to reflections.

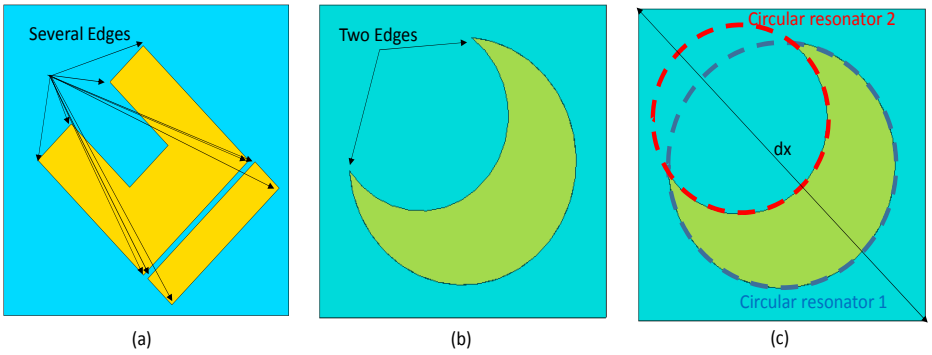

FIGURE 5.1: (a) Unit cell of'U' resonator presented in Chapter 4. (b) Proposed unit cell of 'Half Moon' resonator. (c) The 'Half Moon' is obtained by substracting a big circular resonator 1 to a small resonator 2

Once the dielectric FR4 substrate's relative permittivity $\epsilon = 4.2$, loss tangent $\delta = 0.018$ and thickness of 3.2 mm have been fixed the 'Half Moon' resonator is obtained after days of parametric study using CST Studio 2017. In the parametric study, a circular resonator 2 (having a smaller radius than a circular resonator 1) is substracted from a circular resonator 1. Paramatric studies have been done with the radius of the two resonators, moving circular resonator 2 along the line dx which is oriented at 45°, and the periodicity of the unit cell. Parametric studies have been stopped when broadband absorption is obtained in the range of 4 - 11 GHz. At this stage, the best results obtained are presented in Figure 5.2.

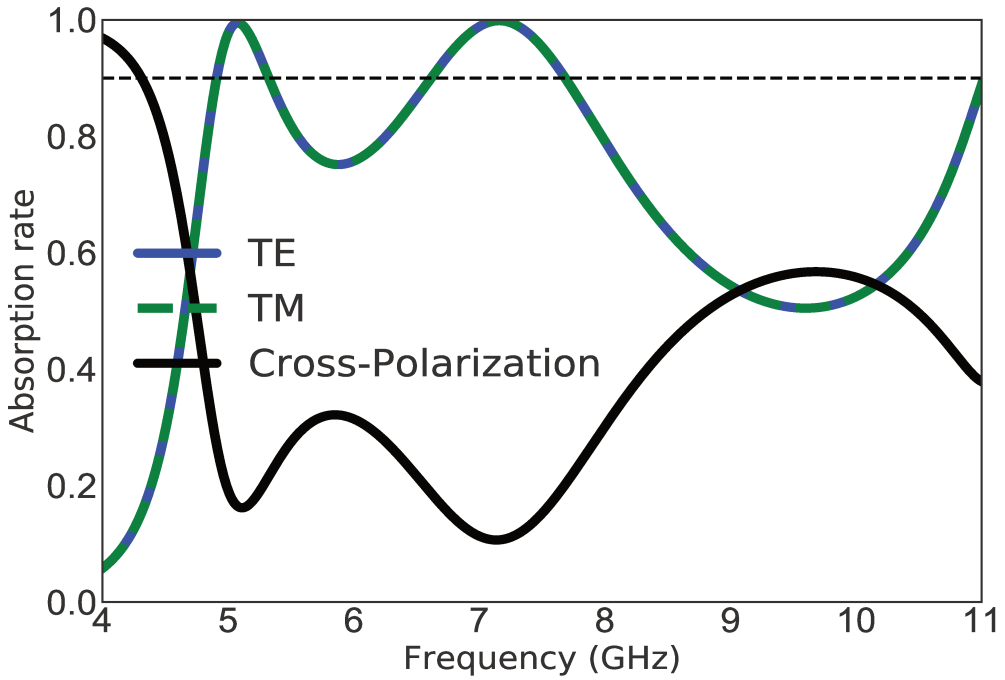

FIGURE 5.2: Absorption rates for normally incident linearly polarized TE and TM waves. Cross-polarization absorption is also shown. Simulations were performed using the commercial software CST Design Studio Suite 2017. Periodic boundary conditions were applied in the numerical model in order to mimic a 2D infinite structure.

From Figure 5.2, we can observe that at least 75% of absorption is obtained in the whole range of 4.7 - 8.3 GHz with two near unity absorption peaks at 5 and 7 GHz respectively for both TE and TM modes. As expected, and discussed in Chapter 4, the cross-polarization absoption is small due to the 45° rotation of the 'Half Moon' resonator. A second layer of FR4 dielectric on which a circular ring resonator is placed is introduced as shown in Figure 5.3.

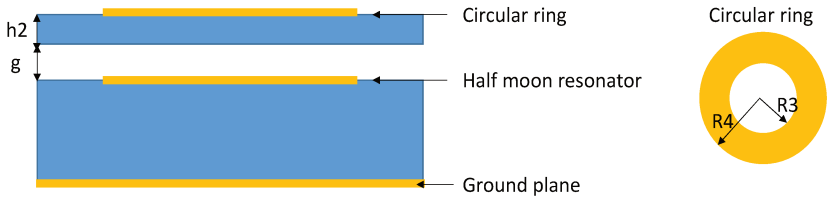

FIGURE 5.3: Design of the dual layer broadband radar absorber.

In the aim to improve the absorption rate and bandwidth of the radar absorber, a huge parametric study on the second layer has been performed. The parametric studies included

the dimensions of the radii R3 and R4 of the circular ring, the distance, g, between the two layers, and the thickness, h, of the second layer. The permittivity of the second layer is kept the same as the first FR4 dielectric substrate. One of our parametric studies on the thickness of the air gap, g, was very important. The study included the reflections and the imaginary parts of the effective impedances of the first layer and of different thicknesses of g. The real part and imaginary part of the normalized effective input impedance must be close to 1 and 0 respectively in order to match the impedance of free space (377 Ω or 1 if normalized). The sign of the imaginary part of the effective impedance (reactance) indicates whether the whole structure is having a capacitive or an inductive behavior. If the reactance is positive, the behavior is inductive and if the latter is negative, the structure has a capacitive behavior. A decrease in the reactance value also means that a capacitive coupling have taken place and an increase in the latter means an inductive coupling have taken place. The reflections and the reactances for different values of g under normal incidence of linearly polarized TE wave are plotted in Figure 5.4. The first row of Figure 5.4, corresponds to the reflection and the second row corresponds to the reactance. To begin with, we compare the resonance frequencies of first the layer only (red curve) to that of when the second layer is added and g = 0 mm (blue curve). We can observe that when we add the second layer, the first frequency peak splits into two adjacent resonances, the second resonance shifts to the right and the third resonance shifts tho the left (first column, first row of Figure 5.4). The splitting of the first resonance is due to two adjacent inductive (blue arrows) and capacitive (red arrows) couplings brought by the second layer (first column, second row). When the gap is increased from 0 mm to 1.5 mm (green curve), the inductive coupling increases and all the frequency resonances move towards higher frequencies (second column of Figure 5.4). When the gap is increased from 1.5 mm to 3 mm (orange curve), the first resonance frequency does not change, the second moves to the right, and the third to the left (third column, first row of Figure 5.4). We can observe from their reactance (third column, second row of 5.4) that an inductive coupling takes place at the second resonance and a capacitive coupling takes place at the third resonance. Hence, adding and air gap and the second layer brings and additional capacitive and inductive coupling which modifies the overall effective impedance of the structure and shifts the resonance frequencies.

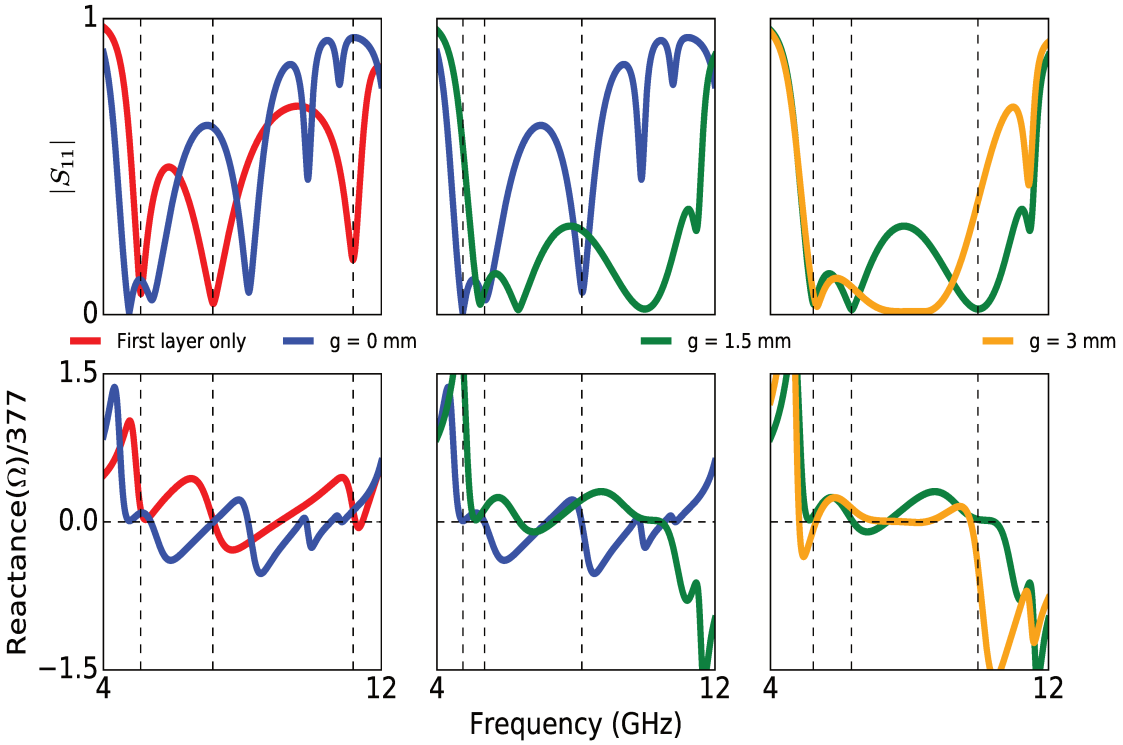

FIGURE 5.4: In the first row, the reflexions (S_{11}) of different values of g are shown. In the second row, the reactances of different values of g are plotted. Simulations were performed using the commercial software CST Design Studio Suite 2017. Periodic boundary conditions were applied in the numerical model in order to mimic a 2D infinite structure.

Thus the final unit cell of the proposed dual layer absorber is depicted in Figure 5.5. The absorber is composed of two layers separated with an optimized air gap of thickness, $g = 1.5$ mm. For the simulations, copper having $5.8 * 10^7$ S/m of electric conductivity and 0.0175 mm of thickness is used for the metallic patterns and ground plane, and dielectric FR4 of relative permittivity $\epsilon = 4.2$ and loss tangent $\delta = 0.018$ is used for the two dielectric substrates. The first FR4 layer, whose thickness, $h1$, is equal to 3.2 mm, is backed with a ground plane to prevent transmission. On top of the first layer, a half-moon-shaped resonator (HMSR) is deposited. The HMSR is obtained by removing, from a circular patch of radius $R1 = 5.45$ mm and center C1 ($x = 0$ mm, $y = 0$ mm), a circular section having radius $R2 = 4.2$ mm and center, C2 ($x = 2$ mm, $y = -2$ mm). A ring-shaped resonator (RSR), of outer radius $R4 = 3.5$ mm, and inner radius $R3 = 2$ mm, is deposited on top of the second FR4 layer which has a thickness, $h2$, equal to 0.5 mm. The unit cells (HMSR and RSR) are arranged in periods of $P_x = P_y = 13.75$ mm.

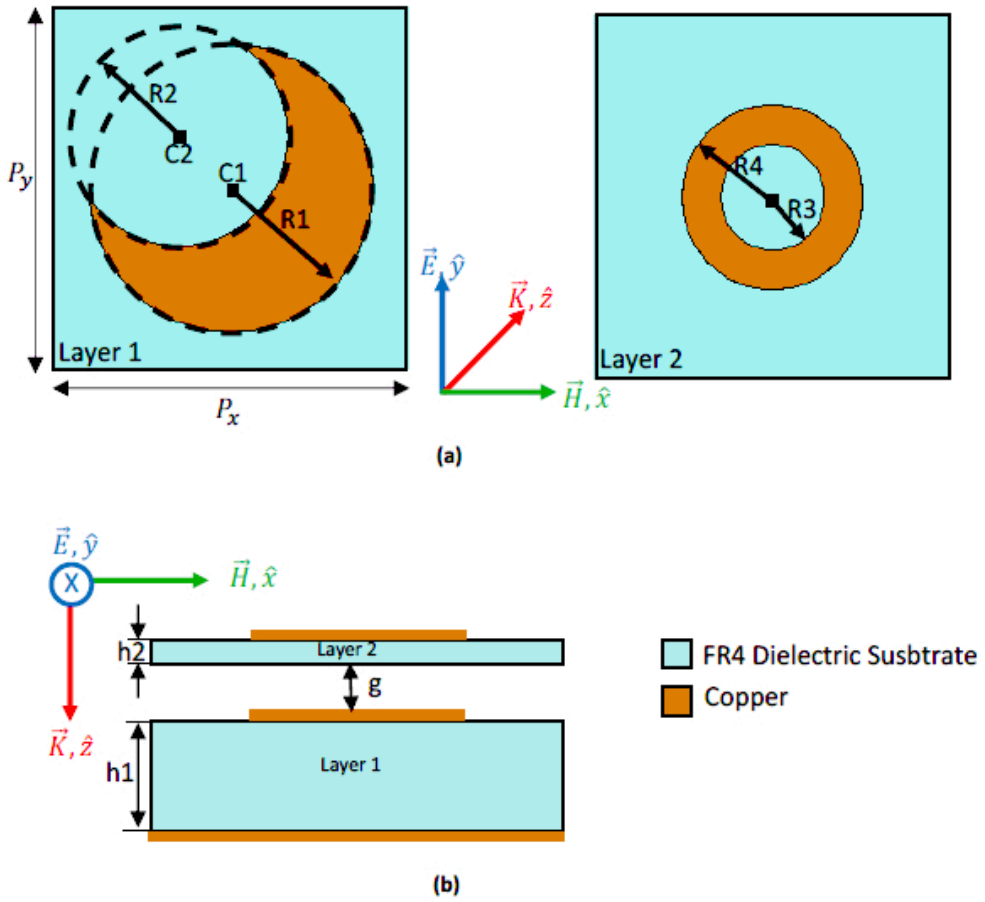

FIGURE 5.5: (a) On the Left hand side: Top view of layer 1 with the HMSR. On the right hand side: Top view of layer 2 with the RSR. (b) Perspective view of the proposed absorber. The first layer is backed with a metallic ground. The second layer is separated from the first layer by an air gap of 1.5 mm.

5.3 Results

5.3.1 Simulated and measured absorption rates

The co-polarization and cross polarization refelction under normal incidence of linearly polarized TE and TM waves are presented in Figure 5.6(a). Their absorptions are presented in Figure 5.6 (b) .The co-polarization absorption rates for normal and oblique incidences of linearly polarized TE and TM waves of our structure are presented in Figure 5.6(c) and (d) respectively. Firstly, we can see that the cross polar absorption rate is not significant (high reflectivity under cross-polarization). As shown in Figure 5.6(b), for normal incidence, the absorption rate is more than 89.7% in the whole band of 4.8 GHz to 11.1 GHz for TE and TM modes. Simulation results for oblique incidences of linearly polarized

TE wave are shown in Figure 5.6(c). For oblique incidences until $\theta = 30°$, the absorption remains more than 89.7% but the bandwidth is very slightly decreased. For 40° of incidence, the absorption rate is higher than 80% in the band of 4.8 GHz - 9.5 GHz and remains above 64% until 11.1 GHz. For 50° of incidence, the absorption is deteriorated but remains significant ($> 78\%$) in the band of 4.8 GHz - 8.7 GHz and more than 50% in the band of 8.7 GHz - 11.1 GHz. These results remain extremely interesting for a large band absorber. The results for oblique incidences concerning TM polarization are the same as those of TE polarization as shown in Figure 5.6 (d). Numerical designs and simulations were performed using the commercial software CST Design Studio Suite 2017. Periodic boundary conditions were applied in the numerical model in order to mimic a 2D infinite structure. Floquet ports were used for the excitation of the periodic structure.

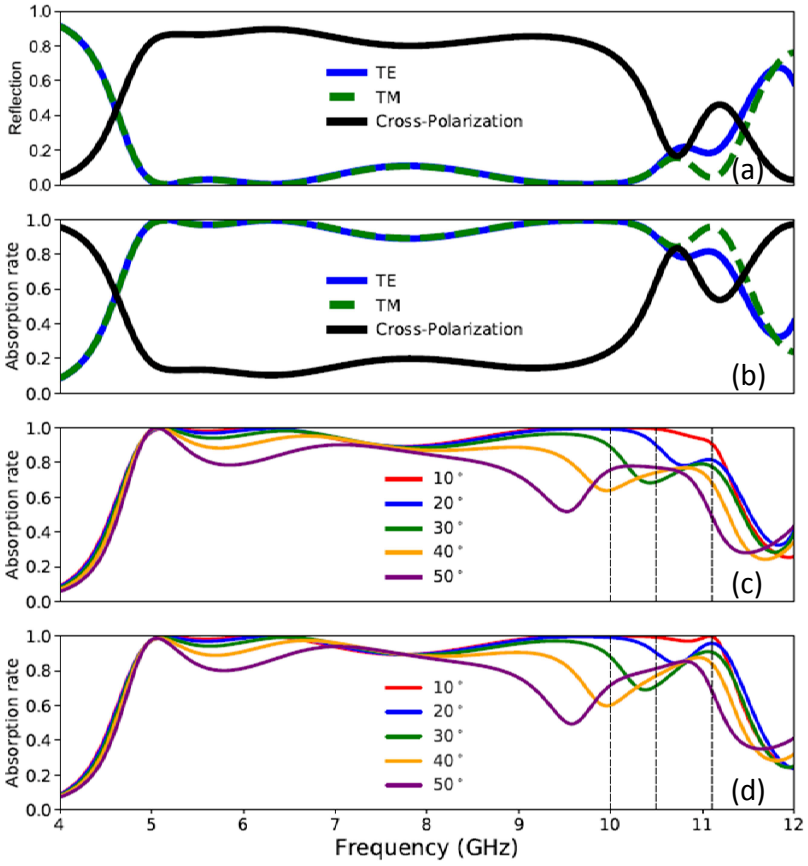

FIGURE 5.6: (a) Co-polarized reflection for normally incident linearly polarized TE and TM waves. The Cross polarization reflection is also shown. (b) Co-polarized absorption rate for normally incident linearly polarized TE and TM waves. The Cross polarization absorption is also shown. (c) Absorption rate of the proposed structure under oblique incidences of 0 - 40° for TE polarization. (d) Same configuration as (c) but for TM polarization.

An experimental prototype has been fabricated with 16 * 16 unit cells of dimensions 300 mm * 300 mm using printed circuit board technology (Figure 5.7(a) and (b)). Both layers were fabricated with a margin error of ±10% for the thicknesses. The thicknesses of the metallic ground and resonating elements are of 0.018 mm. Washers of thickness 1.5 mm ±10% were used to create the 1.5 mm air gap between the two layers (Figure 5.7(c)). Eight holes (four at each end and four in the middle of each edge) of 6 mm were made, and bolts/nuts/screws were used to fix the two layers together. Measurements have been carried out in an anechoic chamber (Figure 5.7(d)) using a vector network analyzer. A pair of broadband FLANNR horn antennas working in 2 GHz - 18 GHz band was used as an emitter and receiver in reflection configuration. The reflection coefficient is normalized using the backed metallic plate of the structure acting as an ideal reflector. The sample is placed at a distance of 1 m in front of the antennas to satisfy far-field requirements. Experimental results were plotted using a free mathematical programming language tool.

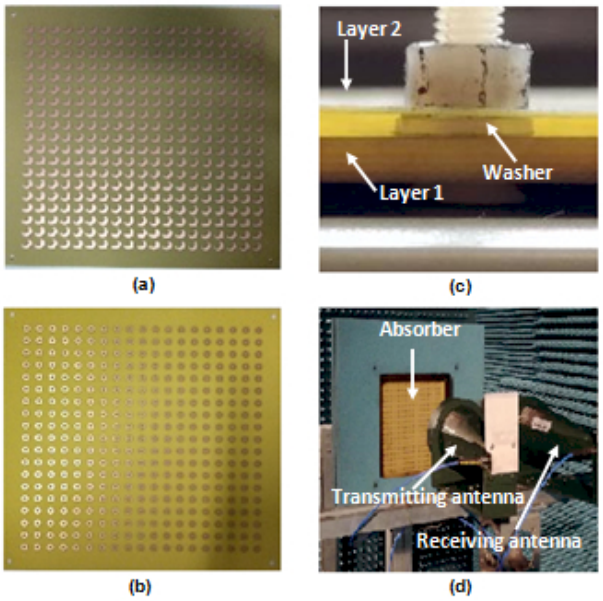

FIGURE 5.7: (a) HMSR layer. (b) RSR layer. (c) Fixing layers 1 and 2 with the 1.5 mm gap. (d) Measurement arrangements in anechoic chamber.

The simulated (blue curve) and the measured (red curve) are plotted in Figure 5.8. We can clearly see a very good agreement between both results. Moreover, we can clearly see the three near unity absorption peaks at 5.17 GHz, 6.16 GHz and 10 GHz for the measured absorption. The measured absorption is the same for both TE and TM modes. The thicknesses of the two substrates and the air gap in simulation were chosen such that the fabrication and measurements could be done easily. However, a parametric study is done in the next chapter to illustrate that total thickness of the structure can be reduced

and the structure leads more than 90% of absorption band in the range of 4.97 GHz - 11.2 GHz.

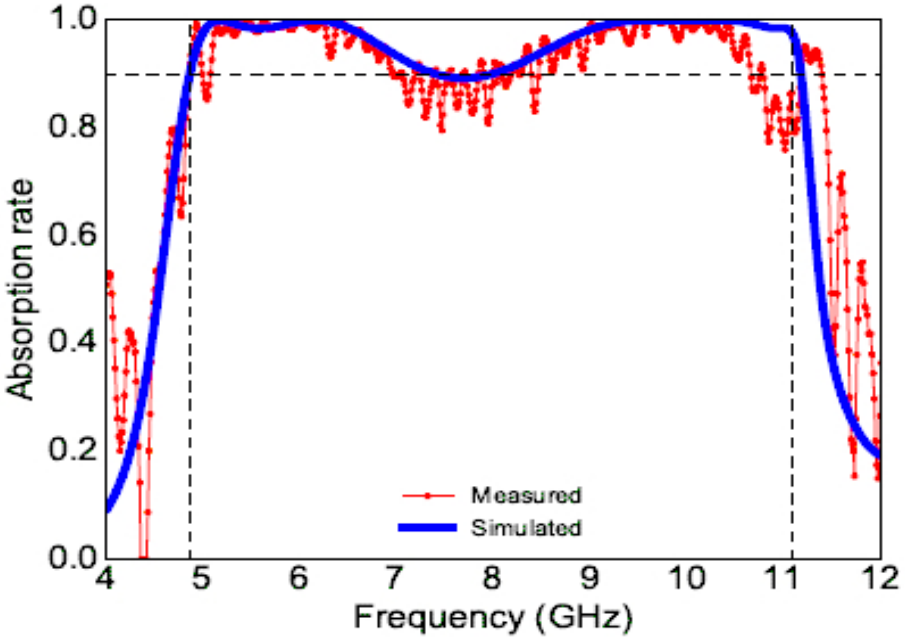

FIGURE 5.8: In red, measured absorption. In blue, simulated absorption.

The thicknesses of the two substrates and the air gap in simulation were chosen such that the fabrication and measurements could be done easily and rapidly. Different values of g, h1 and h2 are plotted in Figure 5.9. When $h1 = 2.7$ mm, $h2 = 0.5$ mm, $g = 1.5$ mm (red curve), the absorption rate is at least of 90% in the whole band of 4.97 GHz - 11.2 GHz. When $h1 = 2.7$ mm, $h2 = 0.65$ mm, $g = 1.5$ mm (blue curve), the absorption is at least of 93% in the whole band of 5 GHz - 11 GHz. Finally, when $h1 = 2.95$ mm, $h2 = 0.8$ mm, $g = 1.16$ mm (green curve), the absorption is at least of 90% in the whole band of 4.9 GHz - 10.8 GHz. Hence, the different thicknesses of g, h1 and h2 can be selected according the the frequency band and the least amount of absorption required.

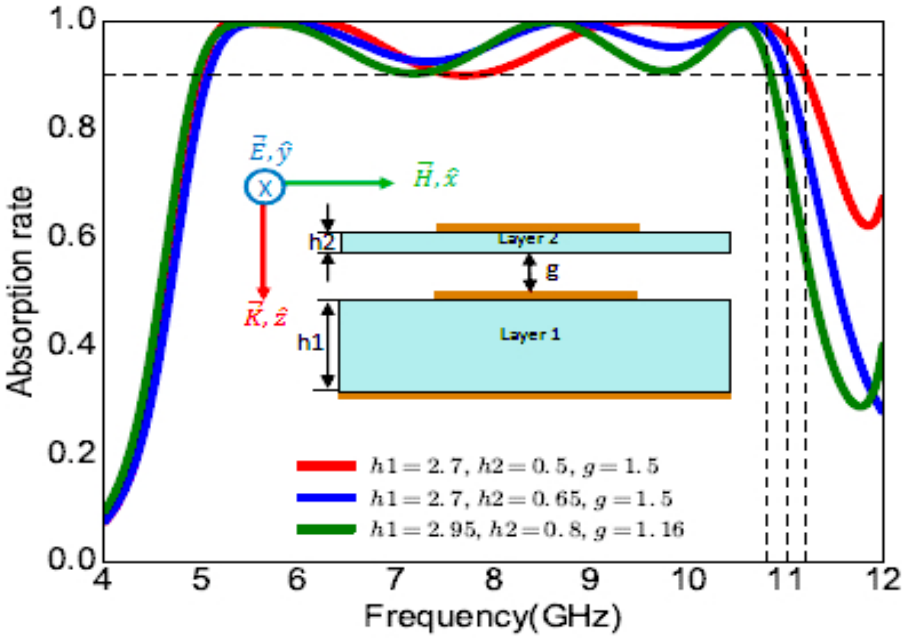

FIGURE 5.9: Absorption rate for linearly polarized TE wave of different values of g, h1 and h2. All dimensions are in millimeters.

5.3.2 Absorption Mechanism

To understand the absorption, we will in this section study the electric field (Figure 5.10(a)) the magnetic field (Figure 5.10(b)) distributions and the power loss density (Figure 5.10(c)) on the two layers for normal incidence of linearly polarized EM waves. The three columns of Figure 5.10(a) and Figure 5.10(c) correspond to the three frequencies of maximum absorption peaks (5.17 GHz, 6.16 GHz and 10 GHz). Their two rows illustrate the first layer with the HMSR and the second layer with the RSR. The three rows of (Figure 5.10(b)) depict the magnetic field distribution on the whole structure at the frequencies of maximum absorption peaks.

For the first absorption peak, the electric resonance is produced around regions A and B of the RSR and around regions E and F of the HMSR (first column of Figure 5.10(a). We can also observe in the first row of Figure 5.10(b), a strong magnetic resonance on the two layers and the air gap. Power loss will mainly occur where the current circulation (not shown) is strong. As shown in the first column of Figure 5.10(c), the surface losses are mainly caused around regions M, N, O, P and Q. For the first absorption peak, the electric resonance is produced around regions E and G of the HMSR as shown in the second column of Figure 5.10(a). We notice from the second row of figure 4b, that a strong magnetic resonance is created only between the HMSR and the ground plane. Surface losses are mainly caused

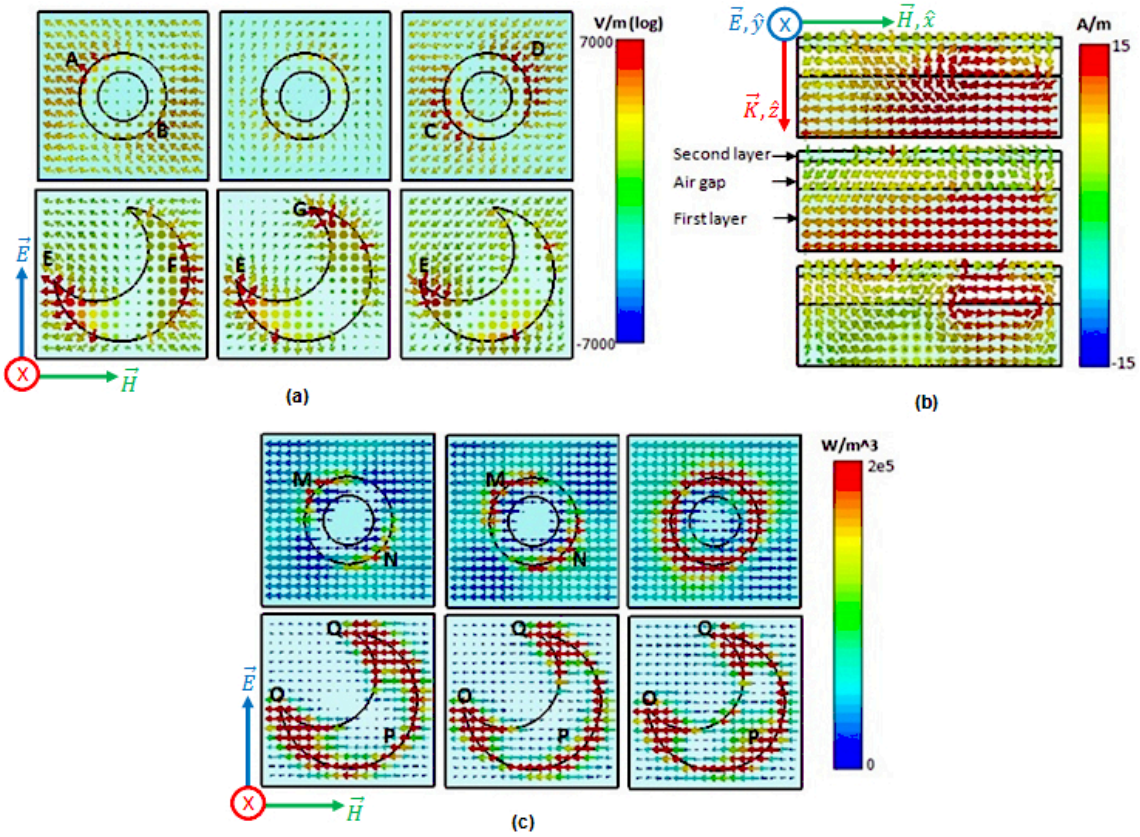

FIGURE 5.10: (a) Top view of electric field distribution on the first and second layers. (b) Perspective view of magnetic field distribution on the first whole structure. (c) Top view of power loss density on the first and second layers.

around regions M, N, O, P and Q as shown in the second column of Figure 5.10(c). For the last absorption peak, the electric resonance is produced around regions C and D of the RSR and around region E of the HMSR (third column of Figure 5.10(a)). In the third row of Figure 5.10(b), we can see a strong magnetic resonance between the HMSR and the RSR due to the circulation of strong anti parallel currents. The surface losses (third column of Figure 5.10(c)) are produced by the whole RSR and regions O, P and Q of the the HMSR. In the three cases overlapping of electrical (Figure 5.10(a)) and magnetic resonances (Figure 5.10(b)) and surfaces losses (Figure 5.10(c)) due to high intensity of current circulation on the HMSR and RSR lead to strong absorption.

5.3.3 Monostatic RCS of the proposed radar absorber

The RCS of the full strucrure has been simulated using CST Studio 2017 and a linearly polarized TE wave is considered with same configurations as described in Chapter 2. Figure 5.11(b) shows the simulated RCS of the full structure (Figure 5.11(a)) at the three

frequencies where near unity absorption peaks have been obtained (5.17GHz, 6.16 GHz and 10 GHz). The simulated structure is 12 cm * 12 cm. The RCS of the radar absorber is compared to the RCS of a 12 cm * 12 cm reference metallic plate. The simulated co-polarization and cross-polarization monostatic RCS of the radar absorber and the metallic plate are shown.

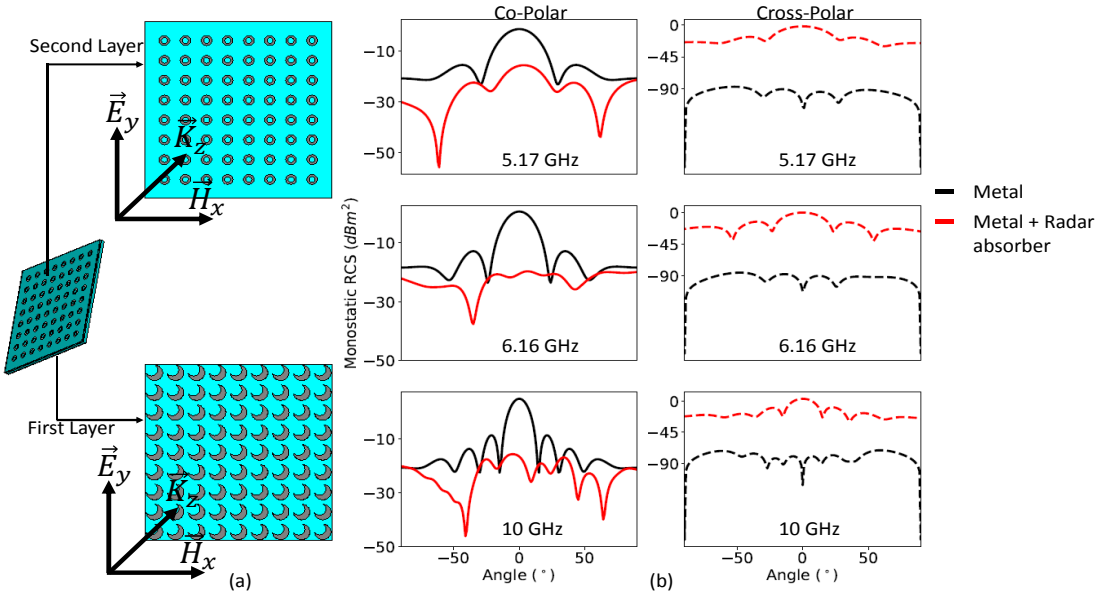

FIGURE 5.11: (a) Simulated full structure with normally arranged first layer. (b) Monostatic RCS for 5.17 GHz, 6.16 GHz and 10 GHz of the absorbing stucture and a perfecty conducting plate of the same dimensions. The first column represents co-polarization RCS results and the second column represents results for coss-polarization RCS. The RCS results between $-90°$ - $0°$ and $0°$ - $90°$ because the meshing on the structure during the simulations was not symetrical.

It can bee seen from Figure 5.11(b) that when the proposed grounded absorbing stucture is considered, the monostatic co-polarization RCS considerably reduces for normal incidence but it sometimes increases for some oblique incidences between $-90°$ - $90°$. When only the metallic plate is considered the monostatic co-polarization RCS for normal incidence is of -1.3 dBm^2, 0.62 dBm^2 and 4.9 dBm^2 for 5.17 GHz, 6.16 GHz and 10 GHz respectively. The monostatic co-polarization RCS of the proposed grounded radar absorber at normal incidence reduces to -15.5 dBm^2, -20.5 dBm^2 and -16.6 dBm^2 for 5.17 GHz, 6.16 GHz and 10 GHz respectively. On the contrary the monostatic cross-polarization RCS of the grounded radar absorber is bigger for all angles and all frequencies than when the metallic plate alone is considered. When only the perfectly conducting plate is considered the monostatic cross-polarization RCS for normal incidence is around -90 dBm^2 at 5.17 GHz,

6.16 GHz and 10 GHz. The monostatic cross-polarization RCS of the grounded radar absorber at normal incidence increases to -1.8 dBm^2, 0 dBm^2 and 3.2 dBm^2 for 5.17 GHz, 6.16 GHz and 10 GHz respectively. In brief, as for our single layer radar absorber in Chapter 4, we have shown that when the first layer of our structure is arranged in a normal periodic manner (as shown in Figure 5.11(a)), the co-polarization monostatic RCS reduces cinsiderably for normal incidence but the cross-polarization monostatic RCS increases considerably.

As our single layer radar absorber in Chapter 4, the cross-polarization monostatic RCS is quite big due to the 45° rotation of the HMSR of the first layer. We have shown in Chapter 4 that, when these type of structures are placed in a 'chessboard' configuration, the cross-polarization to RCS or absorption can be enhanced. The monostatic RCS of the 'chessboard' configured (first layer) full structure has been simulated using CST Studio 2017 and a linearly polarized TE wave is considered. The simulated full structure (with the 'chessboard' configured first layer) for the RCS is depicted in Figure 5.12(a). The simulated structure is 12 cm * 12 cm. The RCS of the radar absorber is compared to the RCS of a 12 cm * 12 cm metal plate. The simulated co-polarization and cross-polarization monostatic RCS of the radar absorber and the metallic plate at 5.17 GHz, 6.16 GHz and 10 GHz (where near unity absorption peaks have been obtained) are presented in Figure 5.12(b).

From Figure 5.12(b), it can be seen that when the proposed radar absorber is considered, the co-polarization monostatic RCS considerably reduces for normal incidence but it sometimes increases for some oblique incidences between $-90°$ - 90° as for the normally structured first layer case. When only the metallic plate is considered the monostatic co-polarization RCS for normal incidence is of -1.3 dBm^2, 0.62 dBm^2 and 4.9 dBm^2 for 5.17 GHz, 6.16 GHz and 10 GHz respectively. The monostatic co-polarization RCS of the radar absorber at normal incidence reduces to -19.1 dBm^2, -8.2 dBm^2 and -8.1 dBm^2 for 5.17 GHz, 6.16 GHz and 10 GHz respectively. On the contrary, as for the normally organised full structure, the monostatic cross-polarization RCS when the radar absorber is placed on the conducting plate is bigger for all angles and all frequencies than when the metallic plate alone is considered but in this case the monostatic cross-polarization RCS reduction is better than for the normal structure. When only the metallic plate is considered the monostati ccross-polarization RCS for normal incidence is around -90 dBm^2 at 5.17 GHz, 6.16 GHz and 10 GHz. When the proposed absorber is considered, the monostatic cross-polarization RCS at normal incidence increases to -20.2 dBm^2, -9.18 dBm^2 and -8.3 dBm^2 for 5.17 GHz, 6.16 GHz and 10 GHz respectively. As for the single layer radar absorber

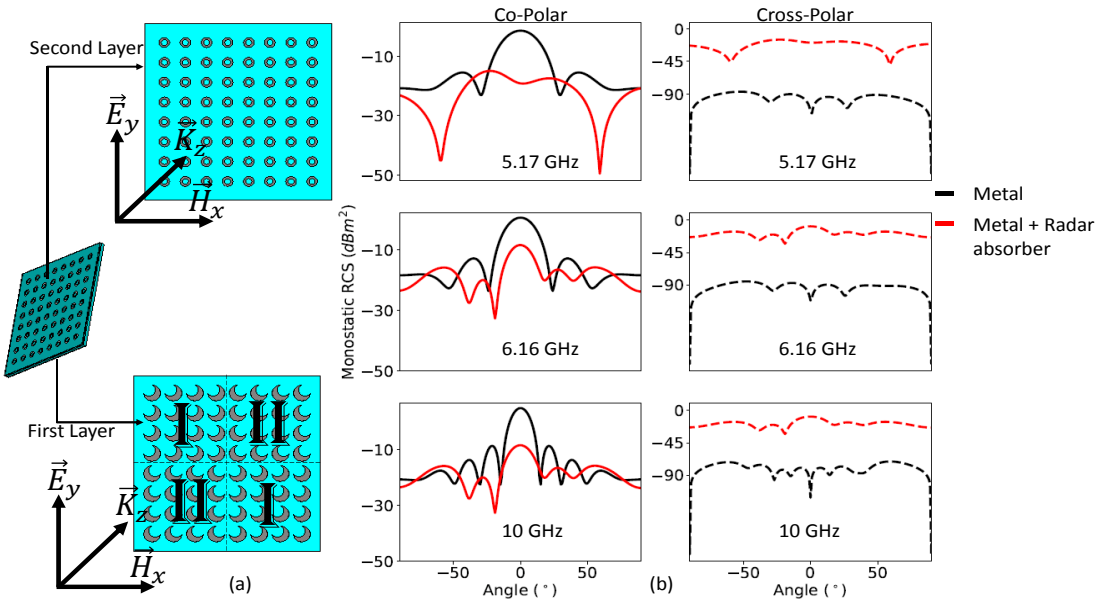

FIGURE 5.12: (a) Simulated full structure with 'chessboard' configured first layer. (b) Monostatic RCS for 5.17 GHz, 6.16 GHz and 10 GHz of the absorbing stucture and a perfecty conducting plate of the same dimensions. The first column represents co-polarization RCS results and the second column represents results for coss-polarization RCS.

in Chapter 4, we have shown that the 'chessboard' configured structure can overcome the problem of cross polarization absorption when compared to the normally arranged full structure.

Table 5.1 below recapitulates all the the monostatic RCS ressults described above for normal incidence.

Object	Co-Polarization RCS at 5.17, 6.16, and 10 GHz in (dBm^2)	Cross-Polarization RCS at 5.17, 6.16, and 10 GHz in (dBm^2)
Reference metal plate	-1.3, 0.62 and 4.9	≈ -90
Normally arranged radar absorber	-15.5, -20.5 and -16.6	-1.8, 0, 3.2
'chessboard' configured radar absorber	-19.1, -8.2, -8.1	-20.2, -9.18, -8.3

TABLE 5.1: Recapitulation of monostatic RCS results.

5.4 Conclusion

Our work on an ultra-broadband thin FSS based radar absorber achieving at least 89.7% of absorption in the whole band of 4.8 GHz – 11.1 GHz has been described in detail in this chapter. The absorption mechanism of our structure was first described by studying the contribution of each layer and secondly by observing the power loss density, the induced electrical and magnetic fields. Next, a parametric study complimented our work to show the coupling between the two layers and the effects that the air gap thickness has on the absorption. Another parametric study was done to give some optimized thicknesses of the two substrates and the air gap. Eventually after fabricating the structure and analyzing it, the experimental results proved to be in alignment with the numerical results. The experimental results are very promising and our design can be used to tackle EMI for civil and military applications. A theoretical to real thickness ratio of 80% is obtained making the structure very interesting. As in our work in chapter 4, due to the 45° rotation of the HMSR, cross-polarization absorption is not achieved. It has been shown by simulation results that when the first layer of the whole structure is configured in a 'chessboard' manner, the cross-polarization issue can be overcome and the the RCS can considerably be reduced. The RCS has been calculated for the three near unity absorption peak frequencies and it has been shown that the proposed structure considerably reduces the RCS when compared to a reference metallic plate. When only the metallic plate is considered the monostatic co-polarization RCS for normal incidence is of -1.3 dBm^2, 0.62 dBm^2 and 4.9 dBm^2 at 5.17 GHz, 6.16 GHz and 10 GHz GHz respectively. When the normally full structure absorber whith the normally arranged first layer is considered, the monostatic co-polarization RCS at normal incidence reduces to reduces to -15.5 dBm^2, -20.5dBm^2 and -20.6 dBm^2 for 5.17 GHz, 6.16 GHz and 10 GHz respectively. In this case the cross-polarization RCS with the radar absorber is quite big. When the structure is arranged in a'chessboard' configuration the co-polarization RCS of the radar absorber is reduced when compared to a metallic plate and the most noticable result is the cross-polarization RCS which is very low when compared to the normally arranged full structure.

In Chapters 3, 4 and 5 all our work on the reduction of RCS was for planar targets and planar radar absorbers was developped. In Chapter 6, cylindrical targets are considered.

Chapter 6

SECTORED DIELECTRICS FOR TOTAL SCATTERING REDUCTION FROM CYLINDRICAL BODIES

6.1 Introduction

Until now, all radar absorbers presented (Chapter 2, 3, 4 and 5) are suitable for planar stuctures. In Chapter 3, we have designed a flexible radar absorber for non planar structures. Nevertheless, if used for a cylindrical target, the radius of the target must be very big when compared to the free space wavelength. If the cylindrical target's radius is comparable or smaller compared to the wevelength, then radar absorbers designed for planar targets are not suitable. When a metallic cylindrical body is illuminated by an EW, the former will scatter EM in all directions around the body. The amplitudes of the scattered fields depend on the radius of the cylindrical body. Depending on the applications, the scattered waves can be more or less critical. Inside radomes of military vessels for example, cylindrical bodies placed in front of antennas causes reflexions (EW scattered towards the source), shadow zones, and also causes deterioration of the radiation pattern of nearby antennas which can be critical. The reduction of EW scattering from these bodies are therefore important. Coating the metallic cylindrical bodies with radar absorbers will reduce back and side scatterings but will not reduce the forward scattering which causes the shadow zones. One way of reducing the scattering in all directions from a

metallic body is to cloak it [101, 102, 103, 104, 105, 106]. Classical passive cloaks reduces scattering in all directions but are often narrow band . Recently active cloaking [108] has been developed in which one half of the metallic cylindrical body must be lossy in order to absorb the incoming EM waves, and the other half of the cylinder must be active in order to redirect towards the front the incoming EM wave. Broadband scattering reduction in all directions can be achieved with active cloaks. One major inconvenient with active cloaks is that active materials are very difficult to implement and the incoming signal must be known [109]. Our aim in this work is two show that using well customized inhomogeneous coatings can reduce scatterings. A way of considerably reducing scattering in all directions from a cylinder whose radius is comparable to the wavelength is demonstrated. It consists of coating the metallic cylinder by well optimized non-magnetic sectors of dielectrics. Each sector is optimized in order to reduce the scattering for a given range of scattering angle. Non magnetic dielectrics have been studied as they can be expensive. First, the analytical expression of bi-static scattering width of a perfectly conducting cylinder is given. Three cases are studied: First is when the radius of the cylinder is very small compared to the wavelength, second when the radius of the cylinder is comparable to the wavelength, and finally when the radius is much bigger than the wavelength. The case when the radius of the metallic cylinder is comparable to the wavelength is of our interest. The bi-static scattering width of a perfectly conducting cylinder coated by a magneto dielectric and a way of selecting homogeneous dielectrics reducing scattering in a given direction are given. One passive coat for back scattering reduction and one active coat for forward scattering are given as examples. We will find that, for both cases either the back scattering or the forward scattering is not reduced. Then the cases of inhomogeneous coating using optimized sectors are presented in detail for five different scenarios. In one of the cases (Scenario 5), the back scattering width is almost zero, the forward scattering width is reduced by 80% and the total scattering is reduced by 65% at the optimization frequency (3 GHz). With the 5 scenarios of inhomogeneous coatings, the back, forward and total scattering widths are at least reduced (because scattering of an uncoated metallic cylinder can be also be increased if coated with an inappropriate coating) in the whole range of 1- 3 GHz. In all the cases, 2D cylinders and an illumination of E - polarized EM wave is considered. All simulations of this chapter have been performed on Comsol 2017.

6.2 Scattering of perfectly conducting cylinders

Let us consider a perfectly conducting (PEC) cylinder of radius, r, illuminated by an electromagnetic wave as illustrated in Figure.

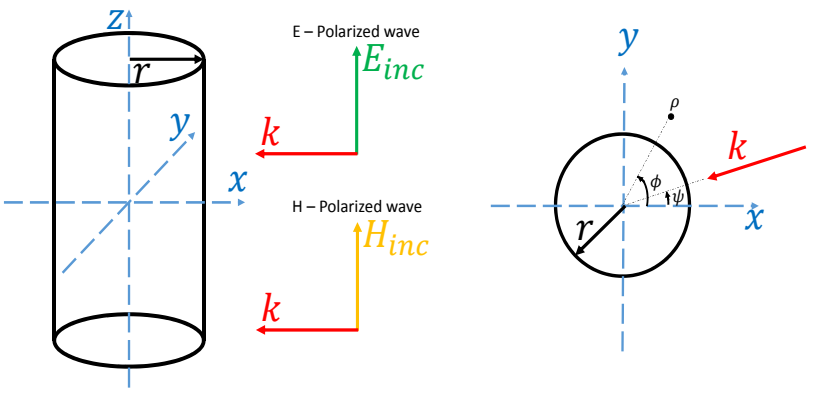

FIGURE 6.1: Illustration of a perfectly conducting cylinder illuminated by electromagnetic plane waves and the associated polar system with incidence and scattering angles.

The bistatic scattering width of an infinite PEC cylinder under normal incidence is given by [78]:

$$\sigma = \frac{4}{k}\left|\sum_{n=-\infty}^{\infty}\frac{\kappa J_n(kr)}{\kappa H_n^{(2)}(kr)}e^{-jn(\phi-\pi)}\right|, \tag{6.1}$$

r is the radius of the cylinder, $k = u\sqrt{\epsilon\mu}$ is the wavenumber in the exterior of the cylinder, ϕ is the scattering angle, J_n is the Bessel function, $H_n^{(2)}$ is the Hankel function of second kind. $\kappa = 1$ and $\kappa = \frac{d}{d(k\rho)}|_{\rho=a}$ for E and H polarized waves respectively.

It can be seen from Equation 6.1, that the scattering width from the PEC cylinder depends on its radius. Three cases of the radius can be defined: First is when the radius is very small compared to the wavelength ($r << \lambda$), second is when the radius is comparable to the wavelength ($r \approx \lambda$) and finally when the radius is very big compared to the wavelength ($r >> \lambda$). Figure 6.2 depicts the normalized scattering width, $\sigma/\pi r$, of the three cases calculated analytically using Equation 6.1 and simulated simulated using Comsol. Simulations and calculations were done for 3 GHz. An illumination of E polarized wave is considered traveling from the right to the left.

The first general observation that can be made from Figure 6.2 is that the analytical and simulated bistatic widths are in very good agreement for the three cases thus validating

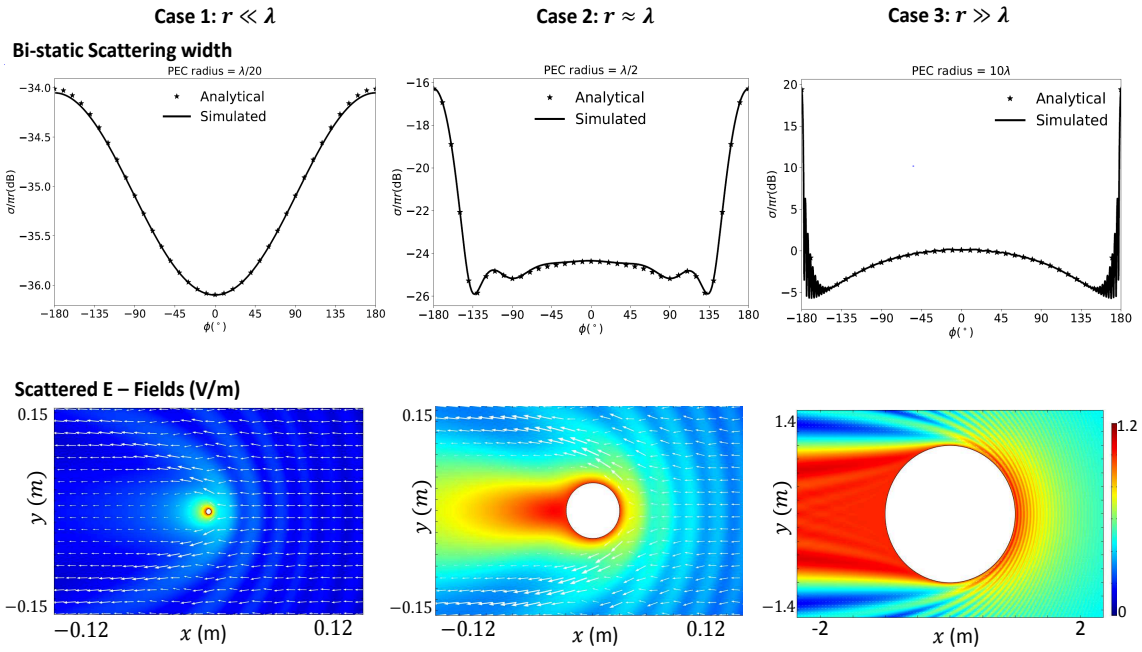

FIGURE 6.2: First row: Analytical and Simulated normalized (with respect to πr) scattering widths of PEC cylinders for the three cases. Second row: Scattered electric field from the PEC cylinders. An illumination of E polarized wave is considered. Simulations and calculations were done for 3 GHz.

Equation 2.1 for any radius. For the case when the radius is very big compared to the wavelength, a radius of 10λ has been studied. For this case, it can be observed from Figure 6.2, that the normalized back scattering width ($\phi = 0°$) is around 0 dB and the normalized forward scattering width ($\phi = \pm 180°$) is around 20 dB. For these values it can be observed that the forward, side and back scattered electric fields are very strong. A strong back scattering width means that a strong intensity of the transmitted energy is reflected back towards the source. A strong intensity of the forward scattering width provokes a shadow zone (zone where the transmitted plane wave does not travel). The very low intensity pointing vectors (white arrows) confirm that the scattering is huge in all directions for a cylinder of $r >> \lambda$.

For the case when the radius is very small compared to the wavelength, a radius of $\lambda/20$ has been studied. The normalized back scattering width is of -36 dB and the normalized forward scattering width is of -34 dB. It can also be observed that the scattered E - fields are of very low intensity in all directions leading in very low reflexion towards the source and nearly no shadow zone as the pointing vectors continue to propagate after the cylinder.

Finally, for the case when the radius is comparable to the wavelength, a radius of $\lambda/2$ has been studied. The normalized back scattering is around -24 dB and the normalized forward scattering is around -16 dB. It can also be observed that the scattered E - fields are of quite low intensity in the backward direction but are huge in the forward direction provoking a shadow zone. This observation is supported by the pointing vectors which are of high intensity before until the cylinder and disappears (or very low intensity) after the cylinder. The next chapter is dedicated to the reduction of scattering of PEC cylinders.

6.3 Coated cylinders

6.3.1 Homogeneous coatings

Let us now consider the case when the PEC cylinder coated with a homogeneous dielectric of thickness h, having a relative permittivity $\varepsilon_1/\varepsilon_0$ and relative permeability of μ_1/μ_0 illuminated by a E-polarized plane wave as illustrated in Figure 6.3. ε_0 and μ_0 are the permittivity and permeability of the surrounding space (free space in our case).

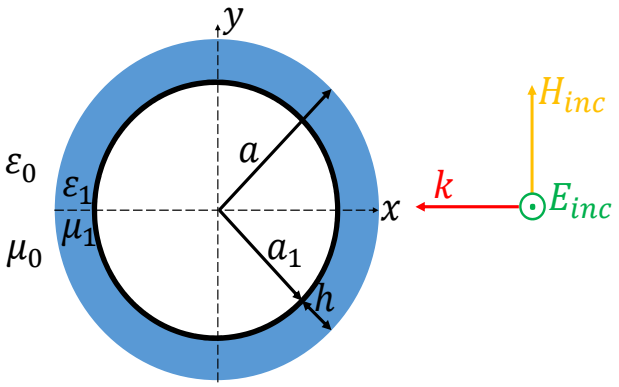

FIGURE 6.3: PEC cylinder of radius a_1 coated by a dielectric of thickness h, illuminated by an E-polarized plane wave.

For an E-polarized plane wave, the scattering width of a PEC cylinder coated with a homogeneous dielectric is given by [78]:

$$\sigma = \frac{4}{k_0 cos^2\psi} \left| \sum_{n=0}^{\infty} (-1)^n v_n A_n^{TM} cos(n\phi) \right|, \tag{6.2}$$

with ψ being the incidence angle, ϕ being the scattering angle,

$$A_{TM} = \frac{\delta_n V_n P_n + q_n^2 J_n(x_0) H_n^{(2)}(x_0)}{\delta_n N_n P_n + [q_n H_n^{(2)}(x_0)]^2}, \qquad v_n = \begin{cases} 1, & n = 0 \\ 2, & n \geq 1 \end{cases} \tag{6.3}$$

$$N_n = H_n^{(2)}(x_0) - z_n H_n^{(2)\prime}(x_0) \tag{6.4}$$

$$P_n = H_n^{(2)}(x_0) - y_n H_n^{(2)\prime}(x_0), \quad V_n = J_n(x_0) - z_n J_n'(x_0) \tag{6.5}$$

$$\delta_n = -\frac{s_0^2}{y_n z_n}, \quad q_n = -\frac{nsin(\psi)}{k_0 acos^2(\psi)} \left(1 - \frac{cos^2(\psi)}{\sqrt{\varepsilon_r \mu_r - sin^2(\psi)}}\right) \tag{6.6}$$

$$s_0 = \frac{1}{cos(\psi)}, \quad s_1 = \frac{\varepsilon_r}{\sqrt{\varepsilon_r \mu_r - sin^2(\psi)}}, \quad r_1 = \frac{\mu_r}{\sqrt{\varepsilon_r \mu_r - sin^2(\psi)}} \tag{6.7}$$

$$x_0 = k_0 acos(\psi), \quad x_1 = k_0 a \ \sqrt{\varepsilon_r \mu_r - sin^2(\psi)}, \quad x_2 = \frac{a_1}{a} x \tag{6.8}$$

$$y_n = \frac{s_0}{r_1} \frac{J_n(x_1) H_n^{(2)\prime}(x_2) - H_n^{(2)}(x_1) J_n'(x_2)}{J_n'(x_1) H_n^{(2)\prime}(x_2) - H_n^{(2)\prime}(x_1) J_n'(x_2)} \tag{6.9}$$

$$z_n = \frac{s_0}{s_1} \frac{J_n(x_1) H_n^{(2)}(x_2) - H_n^{(2)}(x_1) J_n(x_2)}{J_n'(x_1) H_n^{(2)}(x_2) - H_n^{(2)\prime}(x_1) J_n(x_2)} \tag{6.10}$$

The prime($'$) in the equations above denotes the derivative with respect to the argument of the Bessel functions. Non magnetic dielectric ($\mu_r = 1$) are considered in the following studies and the dielectric is allowed to be lossy ($\varepsilon_r = \varepsilon_r' - j\varepsilon_r''$). One way of reducing the scattering is to fix the dielectric's thickness and find the effective permittivity of the latter that gives the minimum possible scattering at a given scattering angle. By using Equations 6.2-6.10, the radius of the PEC cylinder, a_1, the thickness of the dielectric, h, the incidence angle, ψ, the scattered angle, ϕ, can be fixed, and ε_r' and ε_r'' can be varied in order to find the effective permittivity of a dielectric that scatters the least in a given direction (scattered angle).

Let us consider the three cases of PEC cylinders as in Section 6.2 ($a_1 << \lambda$, $a_1 \approx \lambda$, $a_1 >> \lambda$). For the case when $a_1 >> \lambda$, Equations 6.2-6.10 converges very slowly and high frequency approximations must be used. Figure 6.4, is a colormap illustrating ε_r' and ε_r'' that gives the least possible back scattering ($\phi = 0°$) and forward scattering ($\phi = \pm 180°$) for the cases when $a_1 << \lambda$ and $a_1 \approx \lambda$. The thickness of the dielectric is fixed at $\lambda/5$ in the two cases. Normal incidence for E-polarized plane wave is considered and calculations have been performed for reduction of scattering at 3 GHz.

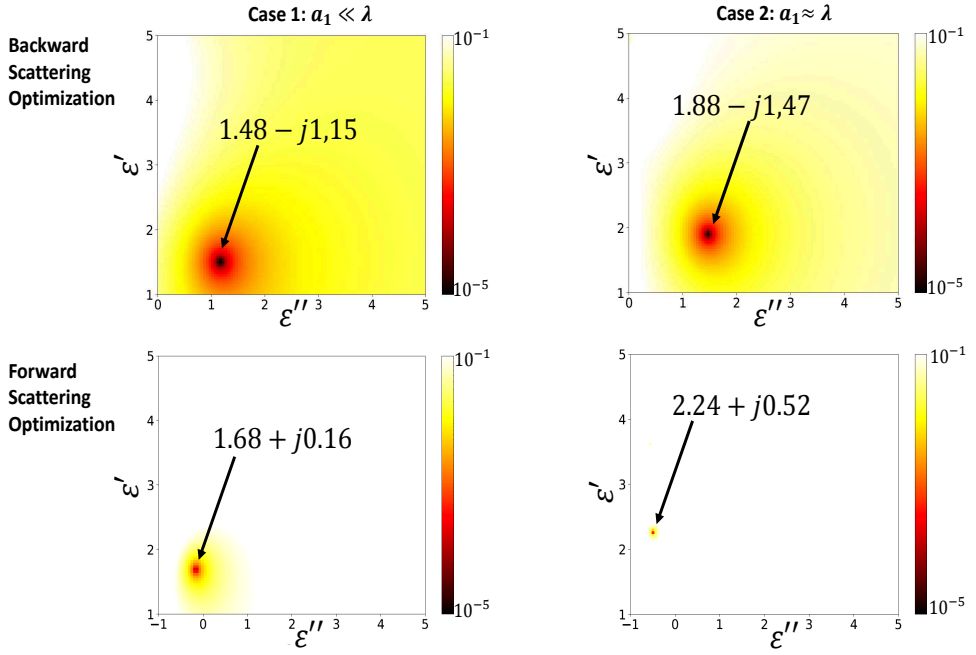

FIGURE 6.4: Colormap to find real and imaginary parts of the permittivity to have the minimum possible backward scattering and forward scattering at 3 GHz for the cases when $a_1 << \lambda$ and $a_1 \approx \lambda$. For $a_1 << \lambda$ and $a_1 \approx \lambda$, the radius of the PEC cylinder is of $\lambda/20$ and $\lambda/2$ respectively.

It can be observed from Figure 6.4 that for both cases of the cylinder's radius, the coating, passive ($\varepsilon_r = \varepsilon_r' - j\varepsilon_r''$) and very lossy in order to reduce the back scattering and must be active ($\varepsilon_r = \varepsilon_r' + j\varepsilon_r''$) for forward scattering reduction. Depending on the sign of the time dependence convention used, the imaginary part of the permittivity can be written with a plus or a minus sign. In our case, we consider a passive material to be lossy and an active material to be one with a gain. For the case when the cylinder's radius is very small ($\lambda/20$) compared to the wavelength, if the dielectric coating has a permittivity of $\varepsilon_r = 1.48 - j1.15$ the normalized linear back scattering width is as small as $3.37 * 10^{-6}$. When the coating has a permittivity of $\varepsilon_r = 1.68 + j0.16$, the normalized linear forward scattering is around

$0.9 * 10^{-3}$. When the cylinder's radius is comparable to the wavelength ($\lambda/2$), when the dielectric coating has a permittivity of $\varepsilon_r = 1.88 - j1.47$ the normalized linear back scattering is of $2.67 * 10^{-6}$ and when the coating has a permittivity of $\varepsilon_r = 2.24 + j0.52$ the normalized linear forward scattering is around $1.8 * 10^{-3}$.

The bi-static scattering width of the homogeneous coatings optimized for the reduction of back and forward scattering are calculated using Equations 6.2-6.10 and simulated using Comsol for the two cases (when $a_1 << \lambda$ and $a_1 \approx \lambda$). The scattered E fields are also illustrated in the figures below. Figure 6.5 represents results for the case when $a_1 << \lambda$ and Figure 6.6 represents results for the case when $a_1 \approx \lambda$.

For a cylinder whose radius is very small compared to the wavelength, it can be seen, from Figure 6.5, that the calculated normalized bi-static scattering widths for different dielectrics are in good agreement with their respective simulated Comsol results. A small deviation can be seen between simulated and calculated results of less than -50 dB and are considered as numerical errors. When a homogeneous $\lambda/5$ thick dielectric having a permittivity of $\varepsilon_r = 1.48 - j1.15$, optimized to reduce the back scattering (Coating 1: green curve), is coated around the $\lambda/20$ PEC cylinder (black curve), the normalized back scattering width is reduced and is as low as -90 dB. The normalized forward scattering width increases compared to a non-coated PEC cylinder but remains around -30 dB. When a $\lambda/5$ homogeneous dielectric having a permittivity of $\varepsilon_r = 1.68 + j0.16$, optimized to reduce the forward scattering (coating 2: red curve), is coated around the $\lambda/20$ PEC cylinder, the normalized forward scattering is reduced and is less than -50 dB but the normalized back scattering increases compared to a non-coated PEC cylinder but remains less than -30 dB. These results imply that a homogeneous passive dielectric (optimized for the reduction of back scattering) or a homogeneous active dielectric (optimized for the reduction of forward scattering) is enough to reduce the back, forward and total scattering of cylinders whose radius are very small compared to the wavelength. In both cases we can see that the E-polarized wave continue to propagate (shown by the white arrows pointing vectors) after the cylinder.

For a cylinder having a radius comparable to the wavelength, it can be seen from Figure 6.6, that when a $\lambda/5$ homogeneous dielectric having a permittivity of $\varepsilon_r = 1.88 - j1.47$, optimized to reduce the back scattering (coating 1: green curve), is coated around the $\lambda/2$ PEC cylinder (black curve), the normalized back scattering is reduced and is less than -60 dB. The normalized forward scattering increases compared to a non-coated PEC cylinder. When a $\lambda/5$ homogeneous dielectric having a permittivity of $\varepsilon_r = 2.24 + j0.52$, optimized to reduce the forward scattering (red curve), is coated around the $\lambda/20$ PEC cylinder, the

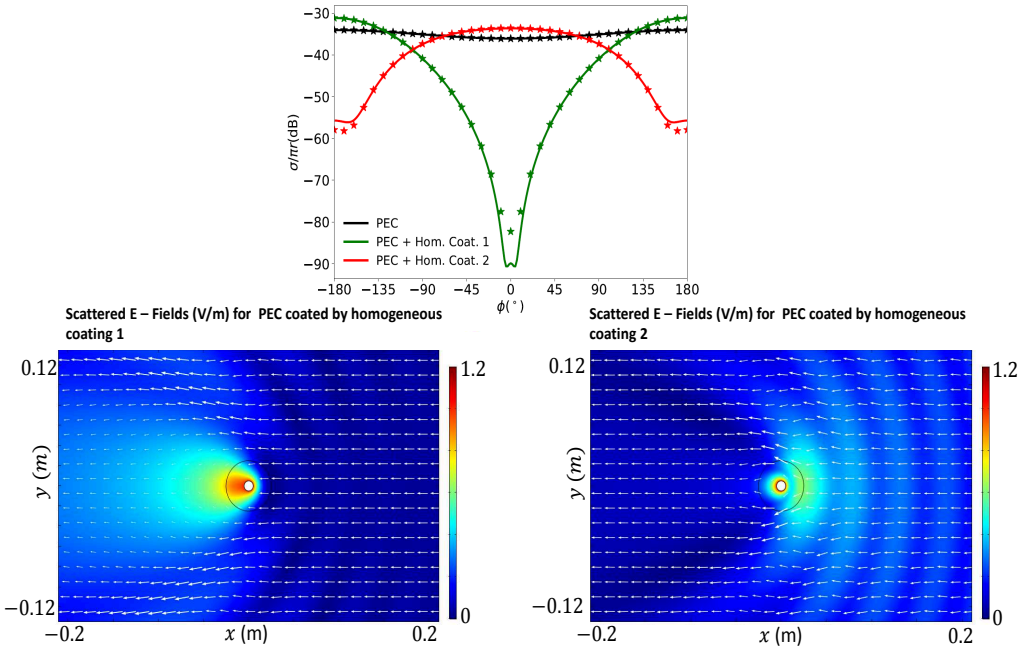

FIGURE 6.5: On top: Calculated (markers) and simulated (continuous curves) of the normalized bi-static scattering widths of a PEC cylinder having radius of $\lambda/20$ (black), of a PEC cylinder coated by a homogeneous dielectric optimized to reduce the back scattering (coating 1: green) and a PEC cylinder coated by homogeneous dielectric optimized to reduce the forward scattering (coating 2: red). The thickness of the homogeneous dielectric is of $\lambda/5$ for the two cases. On the bottom: On the LHS: Scattered E - fields of a PEC cylinder coated by a homogeneous dielectric optimized to reduce the back scattering. On the RHS: Scattered E - fields of PEC cylinder coated by a homogeneous dielectric optimized to reduce the forward scattering. An illumination of E polarized wave is considered. Simulations and calculations were done for 3 GHz.

normalized forward scattering is reduced and is less than -30 dB but the normalized back scattering increases compared to a non-coated PEC cylinder. These results imply that one single homogeneous passive dielectric optimized for the reduction of back scattering or one homogeneous active dielectric optimized for the reduction of forward scattering is not enough to reduce the total scattering of cylinders having a radius comparable to the wavelength. For both coatings, either a shadow zone or a strong back scattering is obtained. Hence a single dielectric coating is not enough to reduce the total scattering of a PEC cylinder whose radius is comparable to the wavelength. Two well optimized sectors (1 passive for back scattering reduction and 1 active for forward scattering reduction) can be used to reduce the total scattering but our challenge is this work is to reduce the total scattering of PEC cylinder whose radius is comparable to the wavelength by using sectors of passive materials.

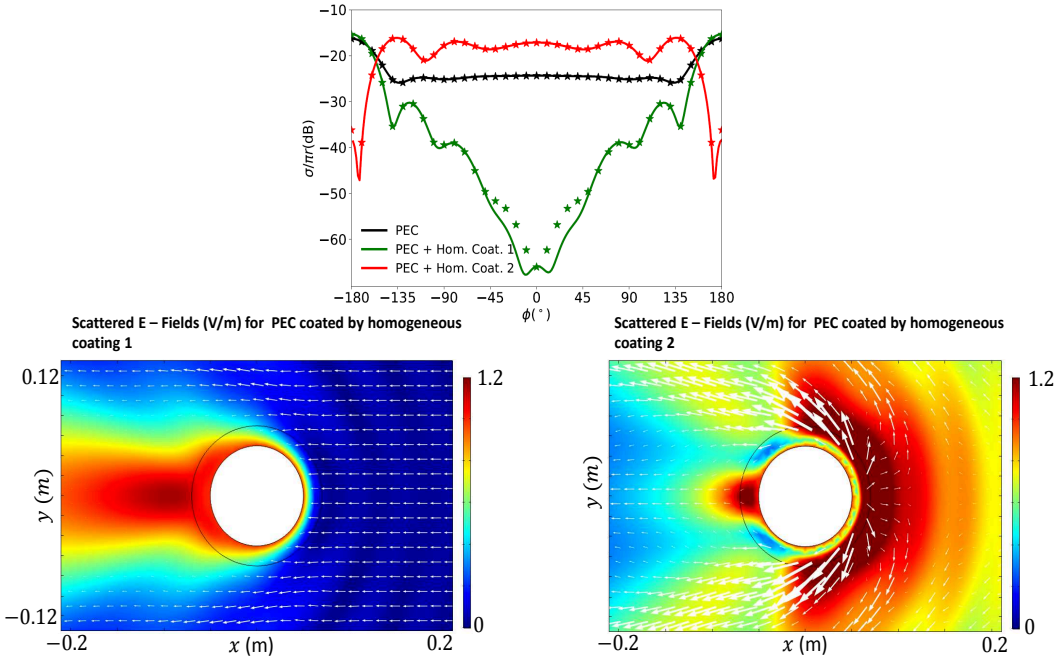

FIGURE 6.6: On top: Calculated (markers) and simulated (continuous curves) of the normalized bi-static scattering widths of a PEC cylinder having radius of $\lambda/2$ (black), of a PEC cylinder coated by a homogeneous dielectric optimized to reduce the back scattering (coating 1: green) and a PEC cylinder coated by homogeneous dielectric optimized to reduce the forward scattering (coating 2: red). The thickness of the homogeneous dielectric is of $\lambda/5$ for the two cases. On the bottom: On the LHS: Scattered E - fields of a PEC cylinder coated by a homogeneous dielectric optimized to reduce the back scattering. On the RHS: Scattered E - fields of PEC cylinder coated by a homogeneous dielectric optimized to reduce the forward scattering. An illumination of E polarized wave is considered. Simulations and calculations were done for 3 GHz.

Since we are interested in three positive linear quantities (σ_{Back}, $\sigma_{Forward}$ and σ_{Total}), in order to compare the different optimizations, data can be represented using triangles as illustrated in Figure 6.7 for the two homogeneous dielectrics optimized for reduction of back scattering and forward scattering. The two cases when $a_1 << \lambda$ and $a_1 \approx \lambda$ are presented. The scattering widths have been normalized with respect to the free space wavelength, λ_0. The total scattering width is the average scattering width with respect to $0 < \phi < 2\pi$.

The illustration of Figure 6.7 confirms our observations made previously for both cases ($a_1 << \lambda$ and $a_1 \approx \lambda$). When $a_1 << \lambda$, the normalized scattering widths (Back, forward, and total) are already small and is close to perfectly cloaked system. Back scattering and total scattering can be reduced using a homogeneous dielectric optimized for back

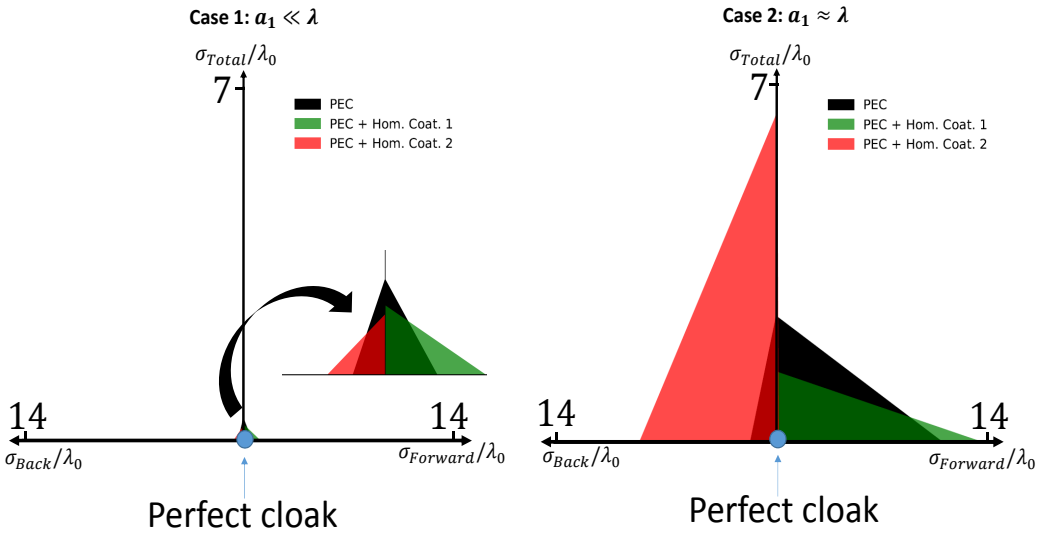

FIGURE 6.7: Triangular representation of σ_{Back}, $\sigma_{Forward}$ and σ_{Total}. The radius of the PEC cylinder (black triangles) is $a_1 = \lambda/20$ for Case 1, and $a_1 = \lambda/2$ for Case 2.

scattering reduction and forward scattering and total scattering can be reduced using a homogeneous dielectric optimized for forward scattering reduction. For the case when $a_1 \approx \lambda$, the normalized total, back and forward scattering widths are quite big. Using a homogeneous dielectric optimized for back scattering reduction reduces the back and forward scattering widths but the forward scattering is increased in this case. When a homogeneous dielectric optimized for forward scattering reduction is coated around the PEC cylinder, the forward scattering is reduced but the back and total scattering widths are increased. The objective in the following subsection is to see if, for a PEC cylinder whose radius is comparable to the wavelength, by using several optimized passive sectors (inhomogeneous coating) the back, forward and total scattering widths can be reduced. This implies that the triangles of the inhomogeneous coatings must be smaller than the triangles of the PEC and the PEC coated by homogeneous dielectrics.

6.3.2 Inhomogeneous coatings

6.3.2.1 Scenario 1: Two sectors

The first scenario using inhomogeneous coatings we consider for the reduction of σ_{Back}, $\sigma_{Forward}$ and σ_{Total} of a PEC cylinder whose radius is comparable to the wavelength is to use two sectors as illustrated in Figure 6.8. Sector 1 is a dielectric of thickness $h = \lambda/5$, having a relative permittivity $\varepsilon_1/\varepsilon_0$ and relative permeability of μ_1/μ_0 and Sector 2 is a dielectric of thickness $h = \lambda/5$, having a relative permittivity $\varepsilon_2/\varepsilon_0$ and relative permeability of μ_2/μ_0. Sector 1 is optimized using Equations 6.2-6.10 and considered

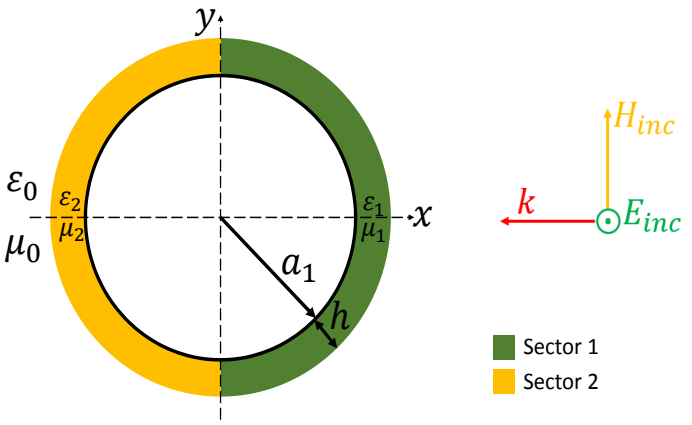

FIGURE 6.8: PEC cylinder having radius $a_1 = \lambda/2$ coated by two sectors having a thickness $h = \lambda/5$ illuminated by an E-polarized plane wave.

as a homogeneous cylinder for optimization of back scattering ($\phi = 0°$). Sector 2 is also optimized using Equations 6.2-6.10 and considered as a homogeneous cylinder for optimization of forward scattering ($\phi = 180°$). The total coating becomes inhomogeneous and of course the back, forward and total scattering will not be reduced systematically as the whole inhomogeneous system has not been solved and two homogeneous coatings have been optimized separately. The sudden break of impedance between the two sectors will also provoke scattering. For a PEC cylinder of radius $a_1 = \lambda/2$ and coating thickness of $h = \lambda/5$, the homogeneous dielectric optimized for back scattering reduction has a permittivity of $\varepsilon_{r1} = 1.88 - j1.47$ and the homogeneous dielectric optimized for forward scattering reduction has a permittivity of $\varepsilon_{r2} = 2.24 + j0.52$ as described in Section 6.3.1. As our challenge is to use passive materials only, Sector 2 is made lossless such that

$\varepsilon_{r2} = 2.24 - j0$. Non magnetic materials are used for both sectors meaning that only the permittivity (ε_r)is optimized and the permeability (μ_r) is fixed to 1. Having fixed Sector 2 as passive, three different cases can be studied. The first case is when Sector 1 is very lossy ($\varepsilon_{r1} = 1.88 - j1.47$), the second case is when Sector 1 is a little lossy ($\varepsilon_{r1} = 1.88 - j(1.47/2)$) which we will call intermediate and finally the third case when Sector 1 is not lossy at all ($\varepsilon_{r1} = 1.88 - j0$). The normalized bi-static scattering widths for the three cases are presented Figure 6.9 .

Table 6.1 below recapitulates the permittivity of the sectors for the different cases.

Case	Sector 1	Sector 2
PEC + Coat. Case 1	Lossy: $\varepsilon_{r1} = 1.88 - j1.47$	$\varepsilon_{r2} = 2.24 - j0$
PEC + Coat. Case 2	Intermediate: $\varepsilon_{r1} = 1.88 - j(1.47/2)$	$\varepsilon_{r2} = 2.24 - j0$
PEC + Coat. Case 3	Lossless: $\varepsilon_{r1} = 1.88 - j0$	$\varepsilon_{r2} = 2.24 - j0$

TABLE 6.1: Permittivty of the two sectors for the three inhomogeneous coatings. The materials presented in this table are not always realizable. In this case, the permittivity of the sectors can be fixed, and the thickness of the sectors must be optimized.

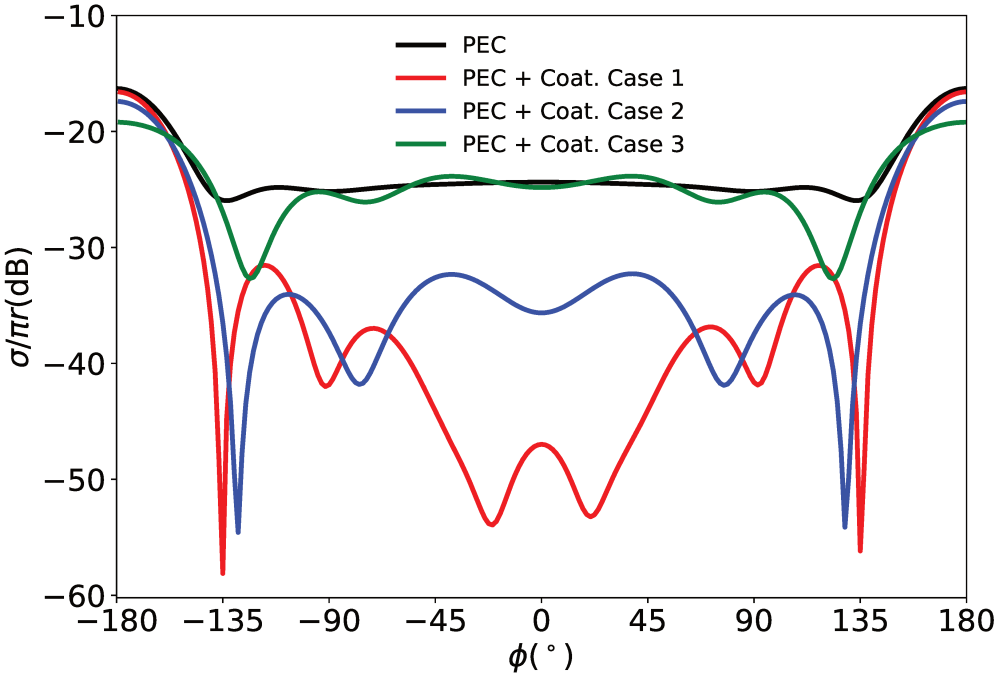

FIGURE 6.9: Bi-Static scattering for a PEC cylinder having radius $\lambda/2$ (black), the case when Sector 1 is lossy (red), the case when Sector 1 is not lossy (green) and the intermediate case (blue). Sector 2 is fixed in the three for the three cases. An illumination of E polarized wave is considered. Simulations and calculations were done for 3 GHz.

When Sector 1 is lossy (the value of permittivity obtained for reduction of back scattering) the back scattering width is reduced and the forward scattering is less than the bi-static scattering of the the PEC cylinder. When Sector 1 is lossless, the forward scattering width is reduced but the back scattering ripples around the back scattering of the PEC cylinder. It can be also observed that when Sector 1 is little lossy (intermediate case), both the back and forward scattering is reduced. In order to make further conclusions, the triangular plots of the 3 cases (Sector 1: Lossy, Intermediate, Lossless) are plotted along the two homogeneous coatings of Section 6.3.1 in Figure 6.10.

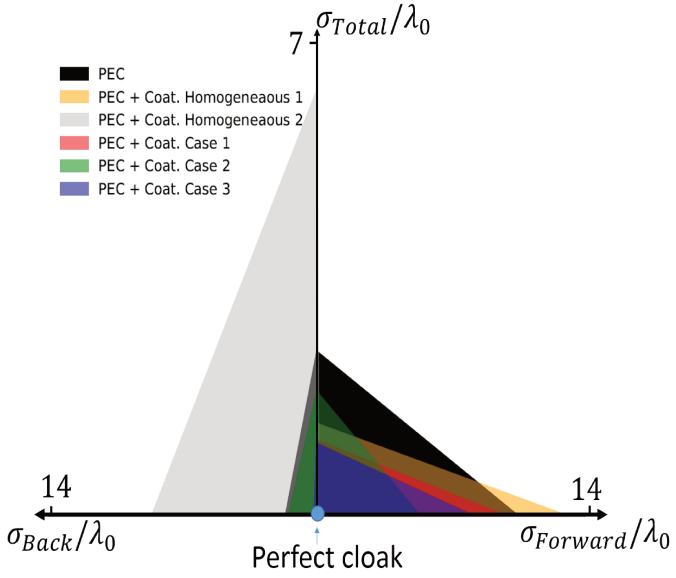

FIGURE 6.10: Triangular representation of σ_{Back}, $\sigma_{Forward}$ and σ_{Total} for a PEC cylinder having radius $a_1 = \lambda/2$, PEC coated with homogeneous coatings 1 and 2 optimized for back scattering and forward scattering reduction respectively as in Section 6.3.1 and the three cases of inhomogeneous coatings.

From Figure 6.10, we can observe that when Sector 1 is Lossy and little lossy (PEC + Coat. Case 1 and 2), their respective triangles are smaller than that of the PEC cylinder coated with homogeneous coating 1. For the case when the PEC cylinder is coated with the inhomogeneous intermediate coating (PEC + Coat. Case 2), the normalized forward scattering width is reduced by 58%, but the total scattering width is increased by 25% when compared to the scattering of the PEC cylinder coated by the homogeneous coating optimized to reduce back scattering (PEC + Coat. Homogeneous 1). The back scattering also is worsen compared to the homogeneous coating. When comparing the same inhomogeneous coating (PEC + Coat. Case 2) with the uncoated PEC, the normalized back scattering width is reduced by 10%, the normalized forward scattering width is reduced by 48% and the normalized total scattering width is reduced by 24%. Some important

conclusions can be made: Firstly, the forward scattering of the PEC cylinder can be reduced without using active materials. Using sectors of well optimized passive materials can reduce back, forward and total scattering. Secondly, is that in this scenario (2 sectors), Sector 1 must be a lossy material in order to reduce the back scattering. Finally if Sector 1 is lossless, the forward scattering is better than the lossy and intermediate case, but the back and total scattering is deteriorated. These results are very motivating and the study of the scenario when more than 2 sectors are coated around the cylinder becomes very promising.

6.3.2.2 Scenario 2: Four equal length $\lambda/5$ thick sectors

The second scenario using inhomogeneous coatings we consider for the reduction of σ_{Back}, $\sigma_{Forward}$ and σ_{Total} of a PEC cylinder whose radius is comparable to the wavelength is to used four sectors as illustrated in Figure 6.11. Sector 1 is a dielectric having a relative permittivity $\varepsilon_1/\varepsilon_0$ and relative permeability of μ_1/μ_0, Sectors 2 and 3 are a dielectric of thickness having a relative permittivity $\varepsilon_2/\varepsilon_0$ and relative permeability of μ_2/μ_0 and Sector 4 is a dielectric having a relative permittivity $\varepsilon_1/\varepsilon_0$ and relative permeability of μ_1/μ_0. All the sectors have a thickness of $h = \lambda/5$.

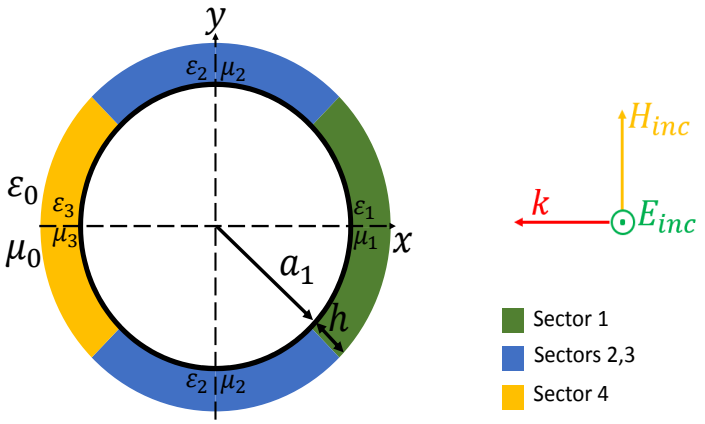

FIGURE 6.11: PEC cylinder having radius $a_1 = \lambda/2$ coated by 4 sectors dielectrics having a thickness $h = \lambda/5$ illuminated by an E-polarized plane wave.

As for the first scenario, Sector 1 is optimized using Equations 2.2-2.10 and considered as a homogeneous cylinder for optimization of back scattering ($\phi = 0°$). Sectors 2 and

3 are also optimized using Equations 6.2-6.10 and considered as a homogeneous cylinder for optimization of side scattering ($\phi = 90°$ and $\phi = -90°$). The cylinder being symmetrical with respect to the Y-Z axis, Sectors 2 and 3 will have the same properties. For a PEC cylinder of radius $a_1 = \lambda/2$ and coating thickness of $h = \lambda/5$, the homogeneous dielectric optimized for back scattering reduction has a permittivity of $\varepsilon_{r1} = 1.88 - j1.47$, the homogeneous dielectric optimized for the side scattering reduction has a permittivity of $\varepsilon_{r2} = 2.11 - j1.08$ and the homogeneous dielectric optimized for forward scattering reduction has a permittivity of $\varepsilon_{r3} = 2.24 + j0.52$. Thus $\varepsilon_{r1} = 1.88 - j1.47$ for Sector 1, $\varepsilon_{r2} = 2.11 - j1.08$ for Sectors 2 and 3 and $\varepsilon_{r3} = 2.24 + j0.52$ for Sector 4. As in scenario 1, Sector 4 is made lossless such that $\varepsilon_{r3} = 2.24 - j0$. Having fixed Sector 4 as passive and having a permittivity of $\varepsilon_{r3} = 2.24 - j0$, four different cases can be studied. The permittivity of the 4 cases of each sector is given in the Table 6.2 below.

Case	Sector 1	Sector 2 and 3	Sector 4
1	$1.88 - j1.47$	$2.11 - j1.08$	$2.24 - j0$
2	$1.88 - j(1.47/2)$	$2.11 - j(1.08/2)$	$2.24 - j0$
3	$1.88 - j0$	$2.11 - j0$	$2.24 - j0$
4	$1.88 - j1.23$	$2.11 - j0$	$2.24 - j0$

TABLE 6.2: Different cases of interest for the four sectors coating. The materials presented in this table are not always realizable. In this case, the permittivity of the sectors can be fixed, and the thickness of the sectors must be optimized.

Case 1 correspond to the exact values of permittivity of sectors calculated as homogeneous coatings for reduction of back, side and forward scattering. Sectors 1,2 and 3 are very lossy in this case. In Case 2, Sectors 1, 2 and 3 are made less lossy than Case 1. All sectors are lossless for Case 3 and only Sector 1 is allowed to have some losses in Case 4 and the other 3 sectors are made lossless. The bi-static scattering for the four cases are presented Figure 6.12 .

When Sectors 1, 2 and 3 are lossy (red curve) the back scattering width is reduced but the forward scattering is more than the bi-static scattering of the uncoated PEC cylinder. When Sectors 1,2 and 3 are lossless (green curve), the forward scattering width is reduced compared to the PEC cylinder but the back scattering width ripples around the back scattering of the PEC cylinder. For the intermediate case (blue curve) both back and forward scattering widths are reduced but the forward scattering remains very close to the forward scattering width of the PEC cylinder. One interesting case is when only Sector 1 has some losses and the other sectors are lossless (brown color). In this case both the back and forward scatterings are reduced compared to the PEC cylinder. The triangular plots of the four cases are plotted in Figure 6.13 and are also compared to the best case

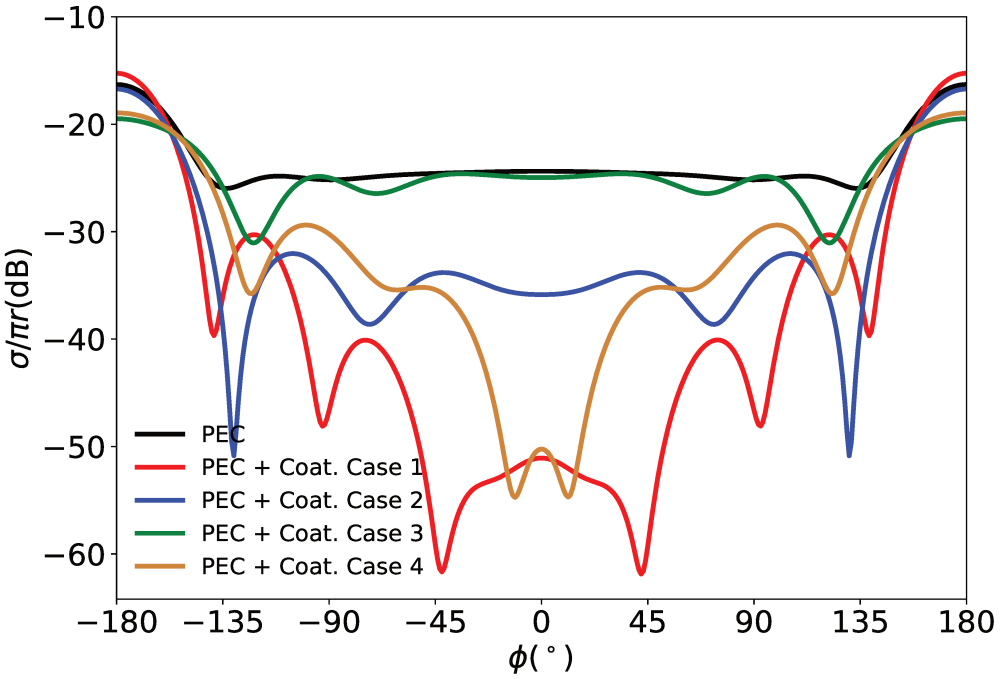

FIGURE 6.12: Bi-Static scattering for a PEC cylinder having radius $\lambda/2$ (black) and for the for different cases. An illumination of E polarized wave is considered. Simulations and calculations were done for 3 GHz.

of Scenario 1. We take the intermediate case of scenario 1 as its triangle is smaller than the other cases.

Between others, Case 4 is an extremely interesting case as it can be observed in Figure 6.13. The triangle of Case 4 is Smaller than the triangle of Cases 1,2,3 and also smaller than the best case of scenario 1. Compared to the homogeneous coat optimized to reduce back scattering (PEC + Coat. Homogeneous 1), the normalized total scattering width is reduced by 23 % and the forward scattering width is reduced by 56 %. The back scattering width remains close to 0 as for the homogeneous coating 1. Without using active materials, a very good reduction of back, forward and total scattering has been achieved. For Case 4, only Sector 1 is lossy and the other 3 sectors are lossless. Does that mean that the section to reduce the backscattering must be very small and very lossy? This scenario is studied in Section 6.3.2.4

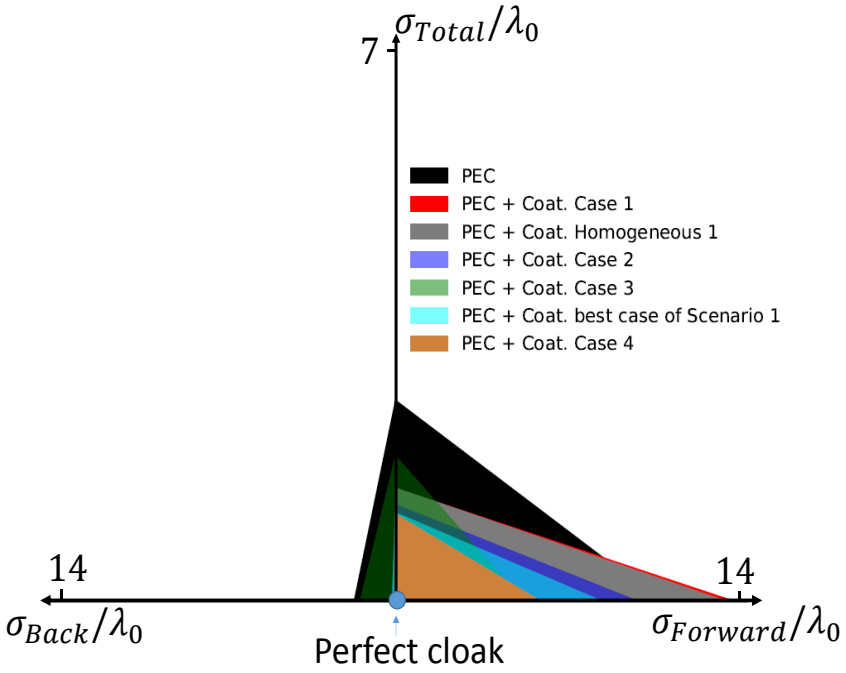

FIGURE 6.13: Triangular representation of σ_{Back}, $\sigma_{Forward}$ and σ_{Total} for a PEC cylinder having radius $a_1 = \lambda/2$, the PEC coated with the homogeneous coating optimized for back scattering reduction, four cases of scenario 2 and the best case of scenario 1.

6.3.2.3 Scenario 3: Software optimized four equal length sectors

In this scenario, the sector parameters (thickness, permittivity) have been optimized using Comsol for the objective being to obtain the minimum possible forward scattering and the same time the back scattering must be small. The parameters of the sectors for one interesting case obeying to this goal are presented in the Table 6.3.

h	Sector 1	Sector 2 and 3	Sector 4
$\lambda/5$	$1 - j0.5$	$2.67 - j0$	$1 - j0$

TABLE 6.3: Permittivity and thickness of the four optimized sectors. The materials presented in this table are not always realizable. In this case, the permittivity of the sectors can be fixed, and the thickness of the sectors must be optimized.

Only Sector 1 is lossy and the permittivity of the Sector 4 is equal to the permittivty of vacuum. It means that for the second case, only three sectors are used but still the forward scattering is reduced. The figures below depict the bi-static scattering of and the triangular plots of this scenario.

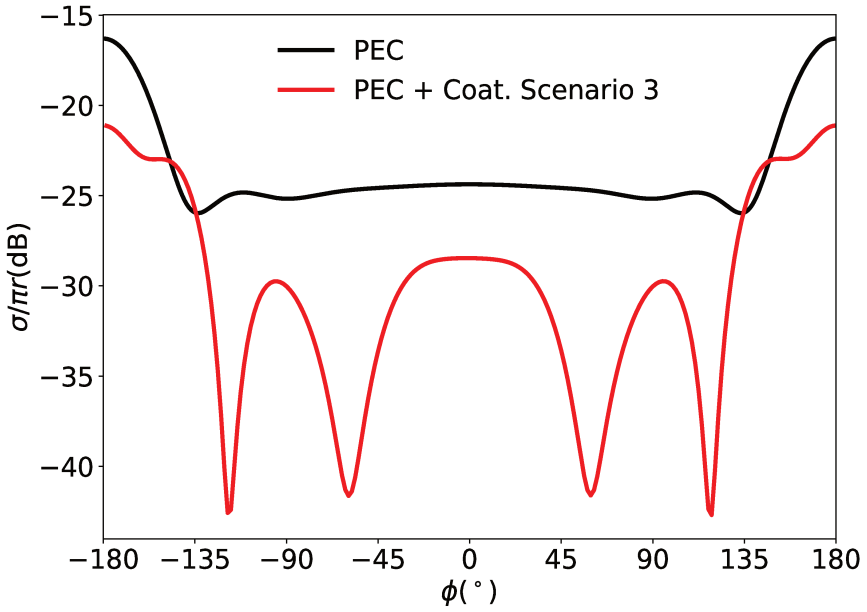

FIGURE 6.14: Bi-Static scattering for a PEC cylinder having radius $\lambda/2$ (black) and for Scenario 3 (red). An illumination of E polarized wave is considered. Simulations and calculations were done for 3 GHz.

The bi-static scattering of scenario 3 represented in Figure 6.14 obeys well to the optimization goal as a normalized forward scattering width of -20 dB (best so far) is obtained and the normalized back scattering width is also very small). Figure 6.15 represents the triangles of this scenario and is compared to the PEC cylinder and the best cases of scenario 1 (Intermediate case) and 2 (Case 4) .

It can be seen from Figure 6.15 that even if the back scattering reduction is not the best for scenario 3, the forward and total scattering are consequently reduced and are the best among all the cases. The normalized forward and total scattering widths have been decreased by 74% and 38% respectively when compared to the homogeneous coat optimized to reduce back scattering (PEC + Coat. Homogeneous 1). What is interesting in this case is that only Sector 1 is lossy and no sectors are used for the forward scattering reduction. The forward and total scattering have been consequently reduced with the use of passive materials.

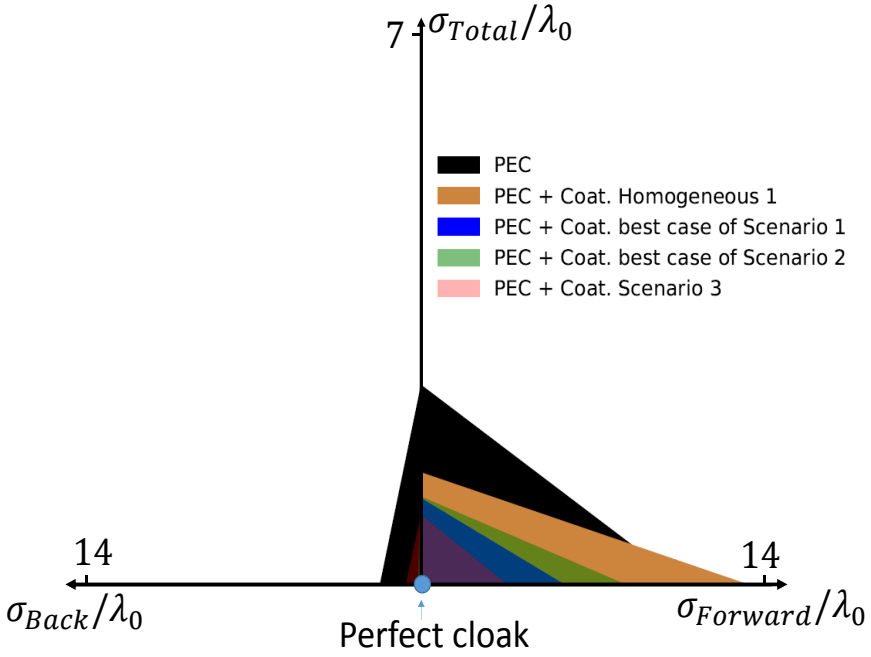

FIGURE 6.15: Triangular representation of σ_{Back}, $\sigma_{Forward}$ and σ_{Total} for a PEC cylinder having radius $a_1 = \lambda/2$, the PEC coated with the homogeneous coating optimized for back scattering reduction, scenario 3, and the best cases of Scenario 1 and 2.

6.3.2.4 Scenario 4: Software optimized 4 sectors with a very small sector for back scattering reduction

Previous results have shown that in order to reduce the forward scattering, only Sector 1 which is optimized for back scattering must be lossy. In scenario 4 sector 1 is made smaller than the other 3 sectors, as illustrated in Figure 6.16, and the sectors are optimized using Comsol. The same goal is given for the optimization as for Scenario 3. This thickness of the sectors are of $\lambda/5$ and their permittivities are given in Table 6.4.

Sector 1 has a sector angle of 20°, Sectors 2 and 3 have a sector angle of 125°, and Sector 4 has a sector angle of 90°. The optimized permittivites of each sectors are given below.

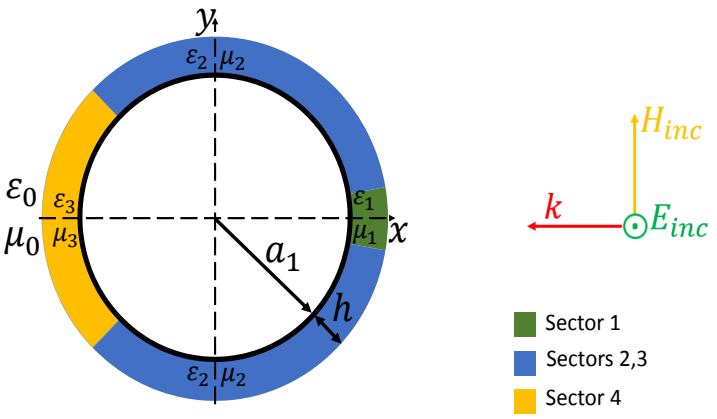

FIGURE 6.16: PEC cylinder having radius $a_1 = \lambda/2$ coated by 4 sectors dielectrics having a thickness $h = \lambda/5$ illuminated by an E-polarized plane wave.

h	Sector 1	Sector 2 and 3	Sector 4
$\lambda/5$	$9.687 - j12.2$	$2.4 - j0$	$1 - j0$

TABLE 6.4: Permittivity and thickness of the four optimized sectors. The materials presented in this table are not always realizable. In this case, the permittivity of the sectors can be fixed, and the thickness of the sectors must be optimized.

The bi-static scattering of scenario 4 is represented in Figure 6.17. It obeys well to the optimization goal as the normalized forward scattering width is less than -20 dB and the back scattering is also small.

Making Sector 1 very small and very lossy allow the forward scattering to be reduced further as shown in Figure 6.17 . Figure 6.18 represents the triangles of this scenario and is compared to the uncoated PEC cylinder, the cylinder coated by the homogeneous coating 1 and the best cases of Scenarios 1 (Intermediate case), 2 (Case 4) and 3.

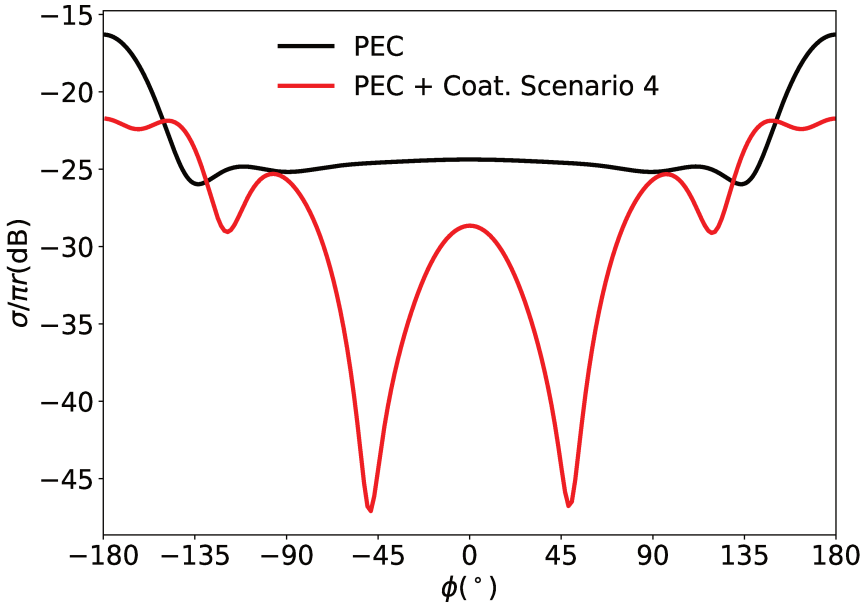

FIGURE 6.17: Bi-Static scattering for a PEC cylinder having radius $\lambda/2$ (black) and for Scenario 4 (red). An illumination of E polarized wave is considered. Simulations and calculations were done for 3 GHz.

Although the forward scattering is reduced when compared to the other scenarios and the back scattering is approximately the same as in Scenario 3, the total scattering is not reduced as the side scattering reduction of Scenario 3 is better than that of Scenario 4. But this scenario validates our strategy of making the sector optimized for back scattering reduction small and very lossy to reduce the forward scattering. From this point, we can think of an inhomogeneous coating made of very small sectors in order to have more parameters to optimize for the reduction of back, forward and total scatterings.

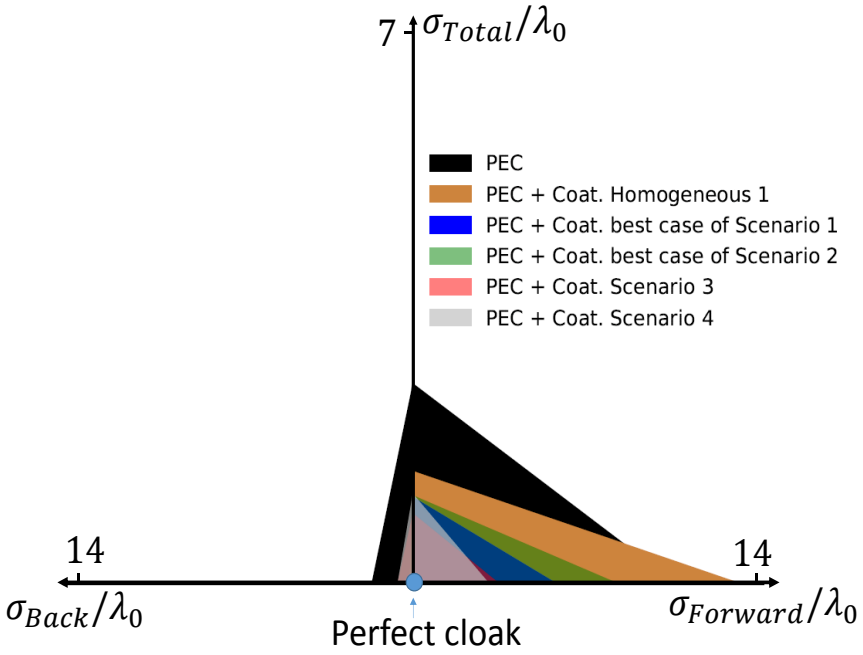

FIGURE 6.18: Triangular representation of σ_{Back}, $\sigma_{Forward}$ and σ_{Total} for a PEC cylinder having radius $a_1 = \lambda/2$,the PEC coated with the homogeneous coating optimized for back scattering reduction, scenario 4 and the best cases of scenarios 1, 2 and 3.

6.3.2.5 Scenario 5: Software optimized 16 equal length sectors

Results of Scenario 4 showed that while making only the sector optimized for back scattering reduction lossy and very small in length, the forward scattering can be reduced. In scenario 3, the side scattering is bigger compared to the other scenarios. In order to reduce the side scattering and decrease the total scattering, the PEC cylinder can be coated by several optimized small sectors. Figure depicts 16 sectors coated around the PEC and optimized using Comsol having an objective to obtain the minimum possible forward scattering and the back scattering must be also very small. The thickness of the sectors are of $\lambda/5$ and their permittivities are given in Table .

In this case also, the sections optimized for the reduction of forward scattering have a permittivity equal to that of vacuum. In fact, we have noticed for scenarios 3, 4 and this scenario that the sector optimized for forward scattering reduction must be a near zero epsilon material or vacuum. The bi-static scattering of scenario 5 is represented in Figure 6.20. It can be observed that the back scattering is very low and that the forward

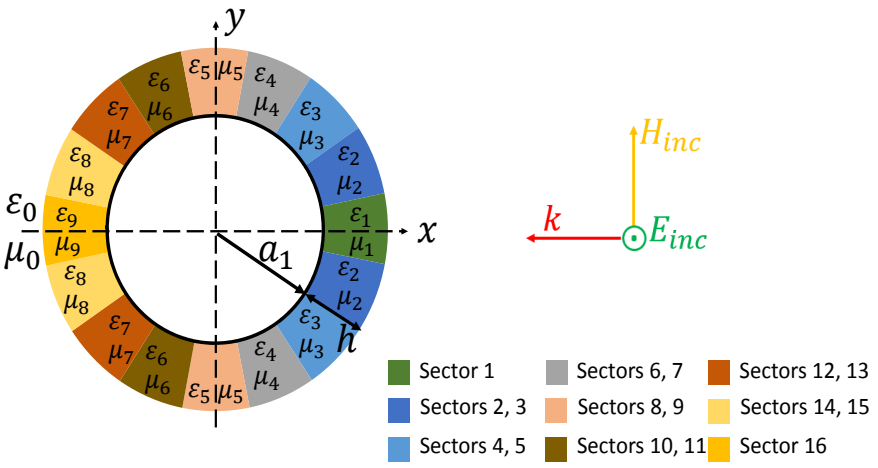

FIGURE 6.19: PEC cylinder having radius $a_1 = \lambda/2$ coated by 16 sectors dielectrics having a thickness $h = \lambda/5$ illuminated by an E-polarized plane wave.

Sector	ϵ_r
1	$9.8 - j12.31$
2, 3	$1.3 - j0$
4, 5	$1.8 - j0$
6, 7	$2.7 - j0$
8, 9	$2.8 - j0$
10, 11	$2.6 - j0$
12, 13	$1.9 - j0$
14, 15	$1 - j0$
16	$1 - j0$

TABLE 6.5: Permittivity and thickness of the 16 optimized sectors. The materials presented in this table are not always realizable. In this case, the permittivity of the sectors can be fixed, and the thickness of the sectors must be optimized.

scattering reduction with this scenario is the best obtained while comparing to all the presented scenarios.

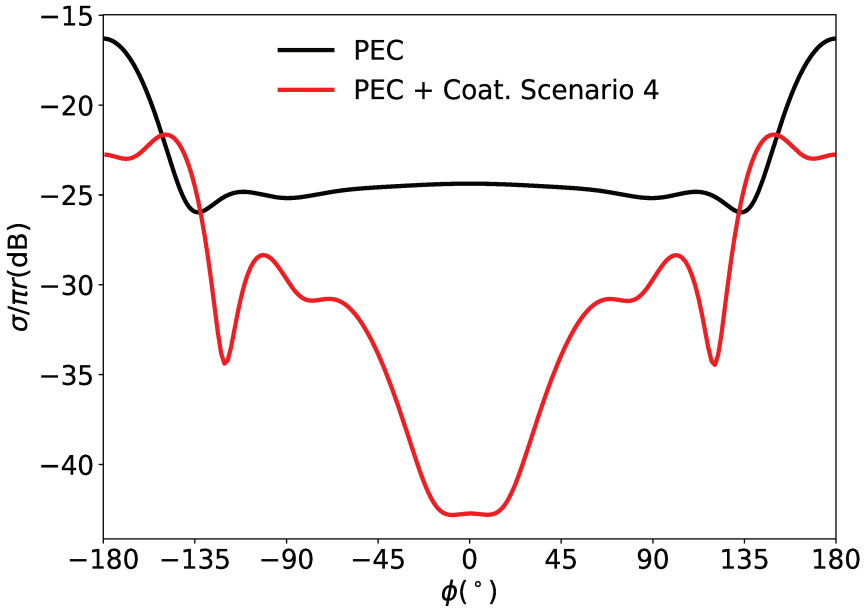

FIGURE 6.20: Bi-Static scattering for a PEC cylinder having radius $\lambda/2$ (black) and for Scenario 5 (red). An illumination of E polarized wave is considered. Simulations and calculations were done for 3 GHz.

The triangle of scenario 5 is the smallest when compared to the triangles of the other scenarios. The total scattering have been reduced compared to scenario 5 even if the forward scattering has also been reduced. This is because fourteen small sectors have been optimized in order to reduce the side scattering compared to scenario 3 where only two sectors were used for the side scattering reduction. For the case when the PEC cylinder is coated with the 16 optimized sectors, the normalized forward scattering width is reduced by 80%, the total scattering width is reduced by 82% when compared to the scattering of the PEC cylinder coated by the homogeneous coating optimized to reduce back scattering (PEC + Coat. Homogeneous 1). The back scattering is also very small as the homogeneous coating. When comparing the same inhomogeneous coating of 16 sectors with the uncoated PEC, the normalized forward scattering width is reduced by 78% and the normalized total scattering width is reduced by 65%.

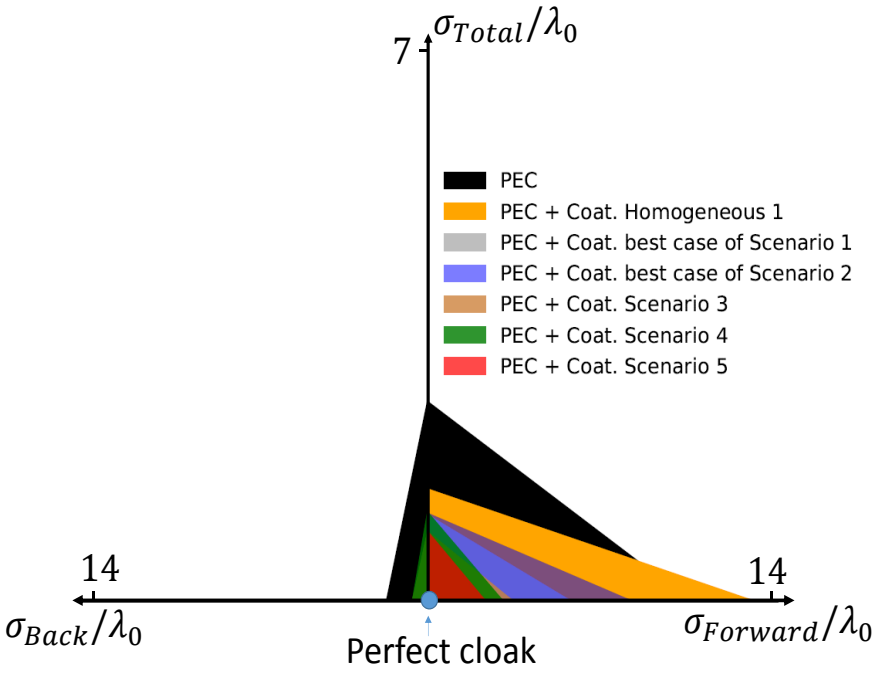

FIGURE 6.21: Triangular representation of σ_{Back}, $\sigma_{Forward}$ and σ_{Total} for a PEC cylinder having radius $a_1 = \lambda/2$, scenario 4 and the best cases of scenarios 1, 2 and 3.

6.3.2.6 Frequency dependency of the coated cylinders

The PEC cylinder having radius $\lambda/2$, coated with the two presented homogeneous coatings and the coated with the inhomogeneous coatings of Scenarios 1-5 have been simulated at 1, 2 and 3 GHz in order to see the frequency dependency of the coatings and presented in Figure 6.22.

The dotted green, black and red dotted lines have been plotted in order to delimit the frequency dependency of the uncoated PEC cylinder and the case when it is coated by the two homogeneous coatings. Firstly, it can be observed that the homogeneous active coating (Coat. 2) has the best forward scattering width reduction between 1 - 3 GHz but the total and back scatterings are even worst than the uncoated PEC cylinder. It can also be observed than the back, total of forward scattering widths of the PEC cylinder coated by the inhomogeneous coatings (all the inhomogeneous coatings) have been reduced at 1, 2 and 3 GHz when compared to the uncoated PEC cylinder. As an example, for Scenario 5, the back scattering width is reduced by 41% at 1 GHz, 96% at 2 and more than 99% at 3 GHz. For the same scenario, the forward scattering width is reduced by 2% at 1 GHz,

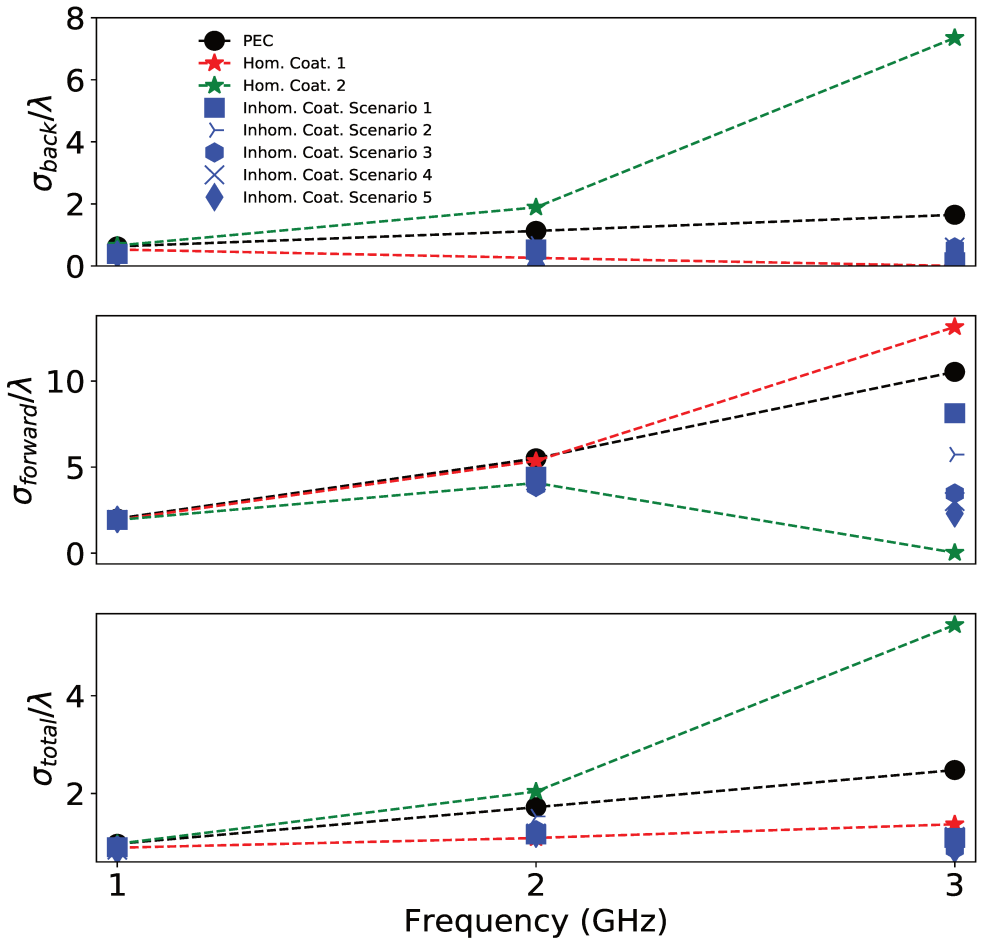

FIGURE 6.22: Frequency dependency of scattering of a PEC cylinder having radius $a_1 = \lambda/2$ and the PEC cylinder coated with homogeneous and inhomogeneous coatings. On top: The normalized back scattering width is presented. In the middle: The normalized forward scattering width is shown and on the normalized total scattering width is shown on the bottom. An illumination of E polarized wave is considered in all the cases. Simulations have been done at 1, 2 and 3 GHz.

26% at 2 GHz, and 78% at 3 GHz. The total scattering width is reduced by 14% at 1 GHz, 32% at 2 GHz and 65% at 3 GHz.

6.3.2.7 Oblique incidences on the coated cylinders

The case when the cylinder is illuminated by an oblique E- field is illustrated in Figure 6.23.

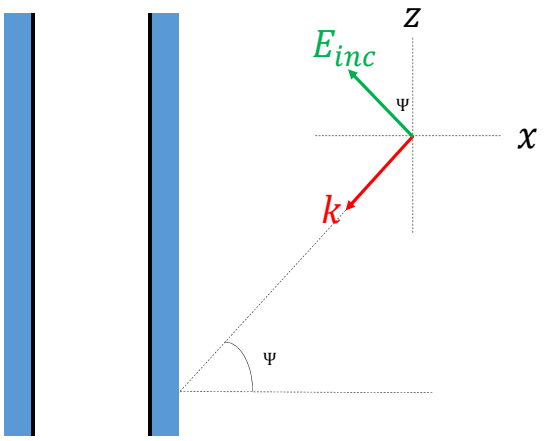

FIGURE 6.23: Cylinder illuminated by an oblique E-polarized plane wave.

In this case the E-field has the x and z components ($E_x = E_0 sin(\psi) e^{jk_0(xcos(\psi)-zsin(\psi))}$ and $E_z = E_0 cos(\psi) e^{jk_0(xcos(\psi)-zsin(\psi))}$). The normalized scattering widths for 10°, 30° and 50° of incidences simulated at 3 GHz is represented in Figure 6.24 for the PEC coated with the two homogeneous coatings and for the PEC coated with coatings of scenarios 1-5.

It can be observed from Figure 6.24, that for oblique incidences of until 50°, the reduction of forward scattering widths of the PEC cylinder coated by inhomogeneous coatings (scenarios 1-5) is better than when the PEC cylinder is coated by the homogeneous coating optimized to reduce back scattering reduction (Hom1). Also, the reduction of back scattering widths of the PEC cylinder coated by inhomogeneous coatings is better than when the PEC cylinder is coated by the homogeneous coating optimized to reduce forward scattering reduction (Hom2). In some cases, 30° of incidence for example when the PEC cylinder is coated with coatings of Scenario 2 and 5, both back and forward scattering reduction are better than the two homogeneous coatings.

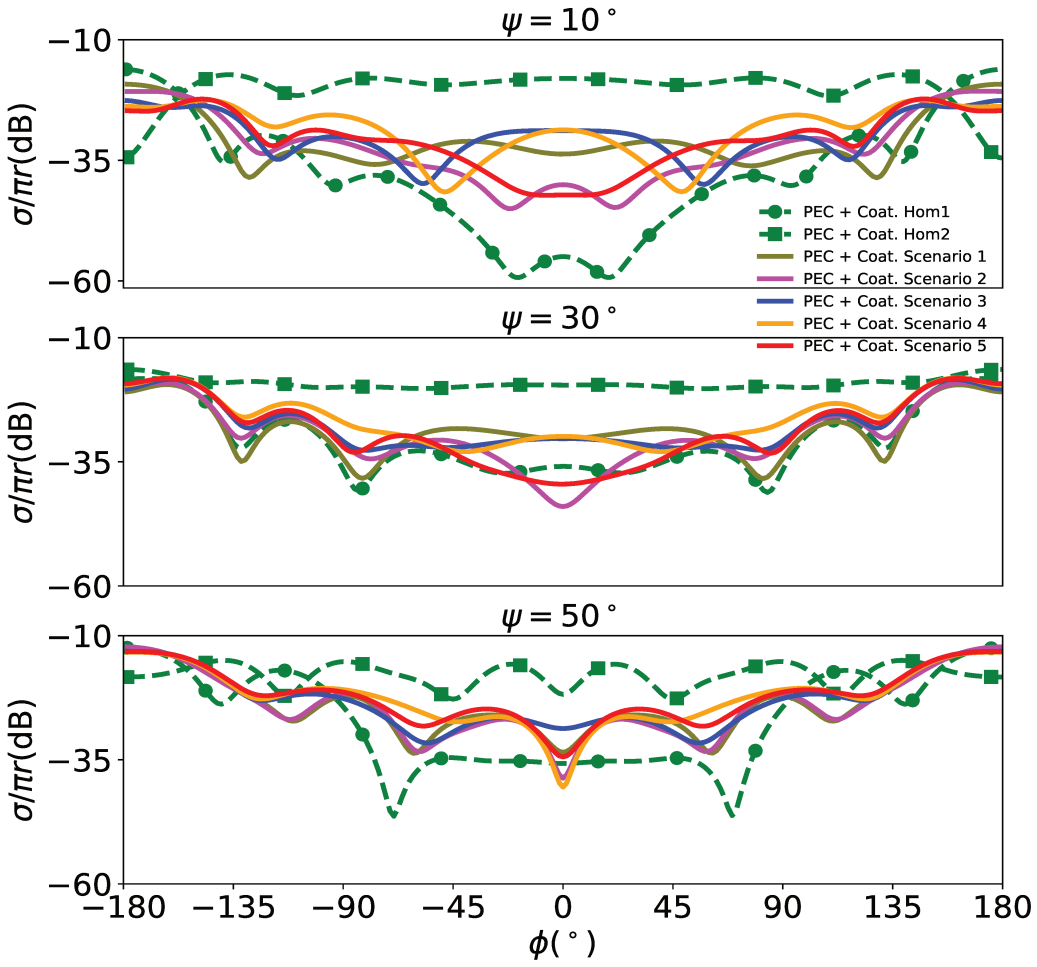

FIGURE 6.24: Normalized scattering widths under oblique incidences of a PEC cylinder having radius $a_1 = \lambda/2$ coated with homogeneous and inhomogeneous coatings of thickness $\lambda/5$. Simulations have been done at 3 GHz.

6.4 Conclusion

It has been shown in this work that coating a perfectly conducting cylinder whose radius is comparable with the wavelength, with small sectors of dielectrics (inhomogeneous coating), the scattering in all directions from a metallic cylinder can be drastically reduced without using active materials. It has been shown that for the case when the PEC cylinder is coated with the 16 optimized sectors, the normalized forward scattering width is reduced by 80%, the total scattering width is reduced by 82% when compared to the scattering of the PEC cylinder coated by the homogeneous coating optimized to reduce back scattering

(PEC + Coat. Homogeneous 1). The back scattering is also very small as the homogeneous coating. When comparing the same inhomogeneous coating of 16 sectors with the uncoated PEC, the normalized forward scattering width is reduced by 78% and the normalized total scattering width is reduced by 65%. For the 16 sectors coating, it has also been shown the broadband back scattering reduction can be achieved as the back scattering width is reduced by 41% at 1 GHz, 96% at 2 and more than 99% at 3 GHz when compared to the uncoated PEC cylinder. Further work of optimization can be done in order to reduce back, forward and total scatterings for a broadband frequency range. It has also been shown that for some scenarios, the back forward and total scattering reductions are better the homogeneous coatings. For all the inhomogeneous coatings, the thickness of each sectors had been fixed to $\lambda/5$ and their permittivities were optimized. In some cases, the values of the permittivities make the dielectrics complicated to implement or fabricate. In this case, as the thickness and permittivity are complementary, the permittivity of the sectors can be fixed and the optimization must be done with the thickness of the sectors.

Chapter 7

GENERAL CONCLUSION AND FUTURE WORKS

The works presented in this thesis is a fruit of 3 years of research on how to reduce electromagnetic interference in radomes of military vessels where several antennas of the X-band are mounted close to each other as described in Chapter 1. One of the main issues is the reflection towards source antennas due to metallic ducts. By using internal studies made by the systems department of CMN, it has been shown that the metallic ducts can cause EMC problems inside radomes such as path loss, and detection of wrong targets. The most logical solution is to use commercial Radar Absorbing Materials (RAM) in order to eliminate reflections. Most of the time, commercial RAM are very expensive and they do not cover the required frequency range. Other studies (not shown in this thesis) have shown that the metallic ducts can cause saturation of antenna and radars, false echoes and shadow zones. The objective of this thesis was to propose solutions to face EMC problems caused by the reflexion of EW towards the sources. In order to reduce reflection of EW, radar absorbers are studied and designed. The frequency range of interest is the 1 - 10 GHz band.

In Chapter 2, we have presented two conventional flat radar absorbers: Magneto-dielectric and resistive sheet based absorbers. For magneto-dieletric radar absorbers, using a magnetic material, the imaginary part of its permeability must de frequency dispersive and must be much bigger than its real part in the whole working frequency range for absorption. Such materials are realizable but the absorption frequency range is limited. Moreover magnetic materials are very expensive. If non magnetic materials are used, by proper optimization of the permittivity, extremely broadband absorption can be obtained.

The main drawback of this type of absorber is that dielectrics having the exact required permittivity are not always commercially available and also due to their $\lambda/4$ thicknesses, they are generally bulky and heavy. Concerning resistive based absorbers, by taking the example of a Salisbury screen, it has been shown that by fixing the permittivity of the dielectric and the thickness at $\lambda_m/4$, broadband absorption can be obtained. Such absorbers (Jaumann, Salisbury screen) are known to be bulky. For these reasons, we have opted to work with MM and FSS based radar absorbers. Due to their exceptional electromagnetic properties, thin and broadband absorbers can be realized. Next, in Chapter 2, a very brief description, some applications and three examples of MM based absorbers are described. It has also been described in Chapter 2 how by using MM or FSS, perfect absorption can be obtained. Proper resonating shapes and dimensions of FSS can provide required real and imaginary parts of surface impedance for absorption in a given frequency band. Also, FSS can be optimized such that broadband absorption is obtained for wide oblique incidence. Furthermore, these features can be obtained by using thin dielectrics. Apart from optimizing the resonant elements, in order to enlarge FSS based radar absorbers' bandwidth, two common techniques used, consist of incorporating resonating elements working at nearby frequencies by arranging then on the same plane or by using multilayers. Both techniques can lead to a drop in the absorption (sometimes $S_{11} >$ -10 dB) at certain frequencies in the bandwidth. Using several elements on the same plane is very difficult to implement due to the lack of space in a small unit cell and coupling between different elements can be difficult to understand and interprete. Moreover, using different resonating elements on a single unit cell can lead to an asymmetrical design and hence degrading the performance considerably for oblique incidences and different polarizations. By following the same reasoning a multilayer structure can considerably increase the total height of the absorber. For all these reasons, designing thin broadband radar absorbers with easily available dielectrics especially for low frequencies (VHF/UHF) and the gigahertz regime (radio frequency and microwave) is very complicated and is still a challenging subject. We have also given a brief description on RCS measurements and described the theoretical to real thickness ratio to judge the performance of an absorber.

Concerning the third Chapter, our work published in Progress In Electromagnetics Research C and entitled 'Theoretical Analysis for Systematic Design of Flexible Broadband Radar Absorbers Using the Least-Square Method' has been presented in detail. In this chapter, a simple but powerful analytical tool to design broadband flexible radar absorbers for any frequency band using the TLM is presented. Firstly, the expressions to calculate the required real and imaginary parts of impedances for broadband absorptions for any dielectric permittivity and thickness are given. The real part of the required impedance

has been associated to a resistance and the imaginary part has been associated to an inductor and a capacitor in series. A simple matrix formulation is used to get the values of L and C that fits the required imaginary part of the impedance at the lower and upper limits of the frequency band. We have shown that broadband absorption can be achieved by increasing the value of the resistance in the TLM. Finally, once all the parameters of the TLM model found, two physical model approaches, using square arrays to design the absorber are described. The first approach consists of using printed metallic square arrays on a grounded dielectric substrate. As for the first approach, the dimensions of the arrays and the unit cell will give the required imaginary part of impedance. The real part of the impedance is obtained by including lumped resistors in the arms of the square arrays. The second approach consists of using resistive sheets patterned as square arrays deposited on top of a grounded dielectric. The dimensions of the arrays and the unit cell will give the required imaginary part of impedance. The required real part of impedance is given by the resistance value of the resistive films. In both cases the square arrays being symmetrical, broadband absorptions for both linearly polarized TE and TM modes are obtained. Also the proposed absorbers achieve as high as 88% for the 90% absorption rate band to center frequency ratio and a theoretical to real thickness ratio of 69.5% making the proposed design strategy extremely interesting.The monostatic RCS of the proposed strcuture has also been simulated at some frequencies in the absorption band. It has been shown that the RCS reduces considerably with the absorber when compared to a metallic plate. When only the metallic plate is considered the monostatic co-polarization RCS for normal icidence is of -13.4 dBm^2, -12.8 dBm^2, -11.5 dBm^2, -8.7 dBm^2, -7.3 dBm^2 and -6.6 dBm^2 at 3, 4, 5, 6, 7 and 8 GHz respectively. When the proposed grounded absorber is considered, the monostatic co-polarization RCS at normal incidence reduces to -19.6 dBm^2, -23.3 dBm^2, -23.1 dBm^2, -30 dBm^2, -26.4 dBm^2, -13.4 dBm^2 for 3, 4, 5, 6, 7 and 8 GHz respectively. The cross-polarization RCS of the metallic plate with and without the radar absorber have also been simulated, and in both cases, the cross-polarization RCS is found to be very small (around -100 dB).The radar absorbers presented in this work have not been fabricated yet. Future works are ongoing on the fabrication of such radar absorbers. The absorption as well as the monostatic RCS must be measured. Moreover, we are working on lumped inductive and capacitive elements between the square patches for the tunability of the frequency band. Until now, the required surface impedance have been designed using an RLC circuit model. Losses are obtained mainly with the resistor (of the corcuit model) and the bandwidth is mainly fixed with the the inductor and the capacitor. The design of radar absorbers using the TLM is simple and powerful but, the litterature provides us, the equivalent circuit model of simple resonating elements.

Therefore, if the absorption bandwidth is to be broadened using more complex resonating elements, the design of radar absorbers using the TLM method can become very complicated. Well optimized resonating elements of MM or FSS (without the use of lumped elements) can provide electric and magnetic resonances such that the impedance of the structure matches with the impedance of air in a broad frequency range. In Chapter 4, such a work is presented.

Our work entitled 'A co-polarization broadband radar absorber for RCS reduction' published in mdpi Materials journal is described in Chapter 4. It is based on a single layer low profile radar absorber exhibiting more than 90% of absorption in the whole band of 5.6 GHz to 9.1 GHz. The proposed structure consists of an Underlined U Shape Resonator (UUSR) deposited on a grounded dielectric and we have shown the main lines of the methodology for designing radar absorber. After providing detailed absorption results for normal and oblique incidences for both TE and TM modes, we have discussed the absorption mechanism by studying a simple TLM and the distribution of electric and magnetic fields. A prototype of the absorber was fabricated and measurement results are in good agreement with numerical results. Due to the proposed original UUSR resonating element, a theoretical to real thickness ratio of 61% is obtained making the proposed UUSR very competitive and useful for future works. One very important limitation of the proposed absorber (when the full structure is configured normally) is that the absorber is not suitable for cross polarization absorption due to the shape of the UUSR. Depending on applications, not achieving cross-polarization absorption is more or less critical. It has been shown by simulation results that when whole structre is configured in a 'chessboard' manner, the cross polarization issue can be overcome and both co and cross polarization RCS can considerably be reduced. The RCS has been calculated for the three near unity absorption peak frequencies and it has been shown that the proposed structure considerably reduces the RCS when compared to a planar reference metallic plate. When only the reference metallic plate is considered the monostatic co-polarization RCS for normal incidence is of 0 dBm^2, 1.7 dBm^2 and 3.6 dBm^2 at 5.87, 7.16, and 8.82 GHz respectively. When the normally arranged grounded full structure absorber is considered, the RCS monostatic co-polarization at normal incidence reduces to reduces to -11.3 dBm^2, -13.6 dBm^2 and -10.9 dBm^2 for 5.87, 7.16, and 8.82 GHz respectively. In this case the cross-polarization RCS with the radar absorber is quite big. When the structure is arranged in a 'chessboard' configuration the co-polarization RCS of the radar absorber is reduced when compared to a metallic plate and the most noticable result is the cross-polarization RCS which is very low when compared to the normally arranged full structure. The 'chessboard' configuration of the full structure has not been fabricated. In the near future we

would like to fabricate the 'chessboard' configured structure and measure its monostatic RCS. In the aim of broadening the absorption bandwidth, a dual layer radar absorber, is presented in Chapter 5.

Our work on a thin dual-layer broadband radar absorber based on FSS achieving at least 89.7% of absorption in the whole band of 4.8 GHz–11.1 GHz which has been published in Nature Scientific Reports and entitled 'A dual layer broadband radar absorber to minimize electromagnetic interference in radomes' is described in Chapter 5. The absorber is composed of two layers separated with an optimized air gap of thickness, $g = 1.5$ mm. The first FR4 layer is backed with a ground plane to prevent transmission. On top of the first layer, a half-moon-shaped resonator (HMSR) is deposited. A ring-shaped resonator (RSR) is deposited on top of the second FR4 layer. We have first given the methology for designing the radar absorber. After providing detailed absorption results for normal and oblique incidences for both TE and TM modes, the absorption mechanism of our structure was described by studying the power loss density, the induced electrical and magnetic fields. Next, a parametric study complimented our work to show the coupling between the two layers and the effects that the air gap thickness has on the absorption. Another parametric study was done to give some optimized thicknesses of the two substrates and the air gap. Eventually after fabricating the structure and analyzing it, the experimental results proved to be in alignment with the numerical results. The experimental results are very promising and our design can be used to tackle EMI for civil and military applications. A theoretical to real thickness ratio of 80% is obtained making the structure very interesting. As in our work in chapter 4, due to the 45° rotation of the HMSR, cross polarization absorption is not achieved. It has been shown by simulation results that when the first layer of the whole structre is configured in a 'chessboard' manner, the cross-polarization issue can be overcome and the the RCS can considerably be reduced. The RCS has been calculated for the three near unity absorption peak frequencies and it has been shown that the proposed structure considerably reduces the RCS when compared to a planar conducting plate. When only the metallic plate is considered the monostatic co-polarization RCS for normal incidence is of -1.3 dBm^2, 0.62 dBm^2 and 4.9 dBm^2 at 5.17 GHz, 6.16 GHz and 10 GHz GHz respectively. When the normally full structure absorber whith the normally arranged first layer is considered, the monostatic co-polarization RCS at normal incidence reduces to reduces to -15.5 dBm^2, -20.5dBm^2 and -20.6 dBm^2 for 5.17 GHz, 6.16 GHz and 10 GHz respectively. In this case the cross-polarization RCS with the radar absorber is quite big. When the structure is arranged in a'chessboard' configuration the co-polarization RCS of the radar absorber is reduced when compared to a metallic plate and the most noticable result is the cross-polarization RCS which is very low when compared to the normally

arranged full structure. We have shown in this chapter that using more than one layer can increase the absorption bandwidth and if the resonating element is well optimzed, the thickness of the radar absorber can be made very close to the theoretical thickness. As for the single layer in Chapter 4, the 'chessboard' configuration of the full structure has not been fabricated. In the near future we would like to fabricate the 'chessboard' configured structure and measure its monostatic RCS.

We have also given the theoretical to real thickess ratio of our designed absorbers. The table below is a comparison of the theoretical to real thickness ratio of our absorbers and we compare them with some other absorbers.

Radar absorber	**Frequency** (GHz)	**Theoretical thickness,** t_T	**Real thickness,** t_R	(t_T/t_R)***100**
[70]	5 - 25	2.55 mm	3.65 mm	69.86 %
[110]	6 - 19	3.43 mm	4.36 mm	78.57 %
[111]	4 - 15	1.206 mm	1.54 mm	78.31 %
[112]	4 - 8	1.237 mm	1.6 mm	77.31 %
[113]	40 - 134	0.294 mm	1 mm	29.4 %
[114]	6- 18	1.64 mm	2.22 mm	73.78 %
$\lambda/4$ Magneto-dielectric	1 - 20	12.6 mm	25 mm	50.4 %
Salisbury screen	1 - 10	3.43 mm	15 mm	22.8%
This work (Chapter 3)	2.5 - 9	5.57 mm	8 mm	69.5%
This work (Chapter 4)	5 - 10	1.95 mm	3.2 mm	61%
This work (Chapter 5)	4 - 12	4.16 mm	5.2 mm	80%

TABLE 7.1: Comparison of broadband radar absorbers. It is important to note that column two contains the frequency range in which the reflexion coefficients were integrated (Chapter 2) and not the -10 dB frequency range.

It can be seen from Table 7.1 that the Salisbury screen presented in Chapter 2 has a very low theoretical to real thickness ratio due to its $\lambda/4$ thickness. With our single layer radar absorbers presented in Chapter 3 and 4, a theoretical to real thickness ratio of 69.5% and 61% is obtained respectively. When our design of two layers of radar absorber is presented, a theoretical to real thickness ratio of 80% is achieved making it the best among the presented performances.

In Chapter 2, 3, 4 and 5 planar radar absorbers have been presented. In the case of a cylindrical target, the radius of the target must be very big when compared to the free space wavelength if planar radar absorbers are to be used. If the cylindrical target's radius is comparable or smaller compared to the wevelength, then radar absorbers designed for planar targets are not suitable. When a metallic cylindrical body is illuminated by an EW, the former will scatter EW in all directions around the body. The amplitudes

of the scattered fields depend on the radius of the cylindrical body. Depending on the applications, the scattered EW can be more or less critical. It has been shown in this work that coating a perfectly conducting cylinder whose radius is comparable with the wavelength, with small sectors of dielectrics (inhomogeneous coating), the scattering in all directions from a metallic cylinder can be drastically reduced without using active materials. It has been shown that for the case when the PEC cylinder is coated with the 16 optimized sectors, the normalized forward scattering width is reduced by 80%, the total scattering width is reduced by 82% when compared to the scattering of the PEC cylinder coated by the homogeneous coating optimized to reduce back scattering (PEC + Coat. Homogeneous 1). The back scattering is also very small as the homogeneous coating. When comparing the same inhomogeneous coating of 16 sectors with the uncoated PEC, the normalized forward scattering width is reduced by 78% and the normalized total scattering width is reduced by 65%. For the 16 sectors coating, it has also been shown the broadband back scattering reduction can be achieved as the back scattering width is reduced by 41% at 1 GHz, 96% at 2 and more than 99% at 3 GHz when compared to the uncoated PEC cylinder. Further work of optimization can be done in order to reduce back, forward and total scatterings for a broadband frequency range. It has also been shown that for some scenarios, the back forward and total scattering reductions are better the homogeneous coatings. For all the inhomogeneous coatings, the thickness of each sectors had been fixed to $\lambda/5$ and their permittivities were optimized. In some cases, the values of the permittivities make the dielectrics complicated to implement or fabricate. In this case, as the thickness and permittivity are complementary, the permittivity of the sectors can be fixed and the optimization must be done with the thickness of the sectors. This work is purely theoretical for the time being. Our short term challenge is to develop a prototype of sectored diecetrics using 3D printing technology.

All the radar absorbers presented in this thesis have not been measured in military boats. The next step is to make measurements directly on the radomes of boats.

Appendix A

Résumé en francais

Les travaux de recherche présentés dans cette thèse concernent la réduction des interférences électromagnétiques entre équipements radars dans les radômes de navires militaires lorsque plusieurs antennes de la bande X sont montées proches les unes des autres (voir Figure A.1). La Figure A.1 présente un schéma d'un radôme comprennant l'ensemble des équipements HF des radars et les goulottes métalliques.

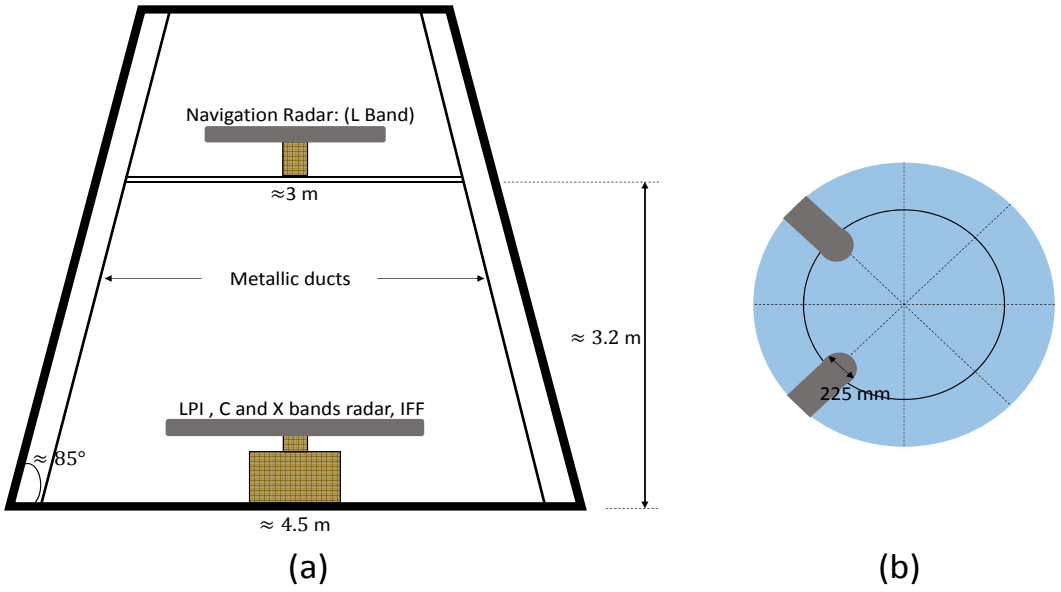

FIGURE A.1: (a) Vue de profil de la représentation d'un radôme. (b) Vue de haut du radôme.

La société Constructions Mécaniques de Normandie (CMN) et le laboratoire LEME de l'Université Paris Nanterre ont décidé de mettre en commun leurs compétences respectives pour concevoir des structures absorbantes radar large bande, ultra-minces, de faible encombrement et coûts afin de réduire les problèmes de Compatibilité Electromagnétique (CEM) à l'intérieur des radomes des navires militaires. Le laboratoire LEME a une grande expérience sur la conception des métamatériaux (MM) et les Surfaces Sélectives en Fréquences (FSS) pour l'absorption radar, la suppression des ondes de surface, dans les structures planaires et la conception des antennes à faible épaisseur ('low profile' et sublongueur d'ondes) à base de métamatériaux. Les CMN sont une société de construction navale et ont construit plus de 700 navires hautement sophistiqués pour la marine en aluminium, acier et matériaux composites avancés. La problématique de CEM est présente non seulement dans les équipements électroniques mais également pour la furtivité et la sécurité. L'innovation dans des matériaux plus minces et légers et donc une priorité de l'entreprise. Dans ce cadre, les travaux de cette thèse sont orientés vers l'étude des problèmes de CEM dans les radômes de navires militaires et des dispositifs de radars large bande pour les applications de la défense. Les travaux de thèse rentrent dans le cadre d'un projet ANRT (CIFRE) entre les deux entités. Les travaux portent sur les interférences électromagnétiques dans les équipements électroniques. C'est un sujet important et stratégique et la recherche de solutions novatrices est d'actualité.

L'un des principaux problèmes à résoudre concerne la réflexion vers les antennes sources due aux conduits métalliques comme illustré dans la Figure A.1. L'ensemble des câbles d'alimentations RF sont gainés dans des goulottes métalliques qui constituent des obstacles. En utilisant des études internes réalisées par département systèmes de CMN, il a été démontré que les conduits métalliques peuvent causer des problèmes de CEM à l'intérieur des radômes, tels que la perte de portée et la détection de 'fausses' cibles. La solution la plus logique consiste à utiliser des absorbants radars commerciaux afin d'éliminer les réflexions. La plupart du temps, les absorbants radars commmerciaux coûtent très cher et ne couvrent pas la bande de fréquences requise. D'autres études (non présentées dans cette thèse) ont montré que les conduits métalliques peuvent saturer les antennes et les radars, ainsi que les faux échos et les zones d'ombres. L'objectif de cette thèse est de proposer des solutions pour faire face aux problèmes de CEM causés par la réflexion de ondes électromagnétiques vers la source. Il s'agit de conçevoir des structures innovantes à base de métamatériaux et des surfaces sélectives en fréquences permettant de réduire les réflexions vers la source. Egalement, il s'agit de conçevoir des structures nouvelles entièrement diélectrique destinées à des cibles cylindrinques permettant de réduire le rayonnement total. La gamme de fréquences considérée est la bande 1 - 10 GHz. Le chapitre

1 porte sur l'enseble de ces apects.

Dans le chapitre 2, nous avons présenté deux absorbants radars planaires conventionnels; Un absorbant radar magnéto-diélectrique et un absorbant radar à base de films résistifs. Pour les absorbants magnéto-diélectriques utilisant un matériau magnétique, la partie imaginaire de la perméabilité du matériau doit être dispersive en fréquence et suffisament élevée dans la bande de fréquence concernée. De tels matériaux sont réalisables mais la plage de fréquence de leur absorption est limitée. De plus, les matériaux magnétiques sont très coûteux. Si des matériaux non magnétiques sont utilisés, une optimisation appropriée de la permittivité, également dispersive en fréquence, permet dans certaine condition d'obtenir une absorption très large bande. Les substrats ayant la permittivité exacte requise sont souvent non disponibles dans le commerce et qu'en raison de leur épaisseur, ils sont généralement volumineux et lourds. Les absorbants à base de films résistifs, en prenant l'exemple d'un absorbant simple couche de Salisburry, il a été démontré qu'en fixant la permittivité du diélectrique et l'épaisseur à $\lambda_m/4$, on peut obtenir une absorption large bande comme démontre la Figure A.2. En faisant varier la résistivité/carrée du film résistif on peut faire varier le taux d'absorption ($> 90\%$).

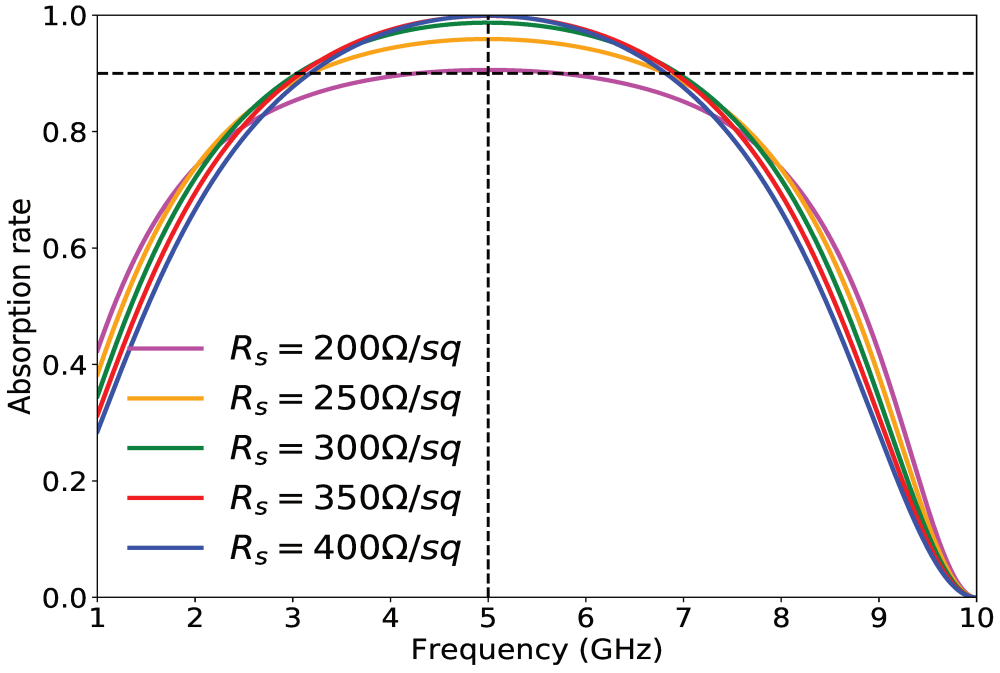

FIGURE A.2: Taux d'absorption en fonction de la fréquence d'un Salisbury screen pour différente valeur de feuille résistive.

De tels absorbants (Jaumann, Salisbury Screen) sont connus pour être volumineux. Pour ces raisons, nous avons choisi d'étudier des absorbants à base de métamatériaux (MM) et des Surfaces Sélectives en Fréquences (FSS). Les propriétés électromagnétiques exceptionnelles des MM permettent de concevoir des nouvelles structures simples ou multi couches absorbantes large bande. A ce titre, le chapitre 2 présente quelques exemples d'absorbants à base de métamatériaux ainsi qu'une bibliographie sur les applications de ces matériaux. Les formes et les dimensions appropriées des résonateurs FSS développées permettent, après optimisation, de fournir les impédances de surface réelles ($\mathrm{Re}(Z_s)$) et imaginaires ($\mathrm{Im}(Z_s)$) requises pour une absorption dans une bande de fréquences donnée. Pour d'autres applications, l'optimisation des structures (FSS) doit peut se faire non seulement pour la bande passante mais également pour la couverture des incidences obliques. Afin d'élargir la bande d'absorption des absorbants radars basés sur le FSS, il est important d'optimiser les résonateurs et les techniques d'asscociation de ces résonateurs (couplages électromagnétiques) . Les deux techniques couramment utilisées consistent à incorporer des résonateurs travaillant à des fréquences proches en les disposant sur la même couche ou en les disposant en multicouches. Cependant, les deux techniques peuvent entraîner une baisse de l'absorption (parfois $S_{11} > -10$ dB) à certaines fréquences à l'intérieur de la bande concernée. L'utilisation de plusieurs éléments sur le même plan est très difficile à mettre en œuvre en raison du manque d'espace dans une petite cellule unitaire et le couplage entre différents éléments peut être difficile à optimiser. De plus, l'utilisation de différents résonateurs sur une même unité de cellule peut conduire à une conception asymétrique et donc à une dégradation considérable des performances pour les incidences obliques et les différentes polarisations. En suivant le même raisonnement, une structure multicouche peut elle aussi augmenter considérablement l'épaisseur de l'absorbant. Pour toutes ces raisons, la conception d'absorbants radars fins large bande avec des diélectriques facilement disponibles dans le commerce reste très compliquée. Dans ce chapitre nous avons également donné une description de la mesure monostatique de la Signature Equivalante Radar (SER) et décrit comment on peut utiliser le rapport entre l'épaisseur théorique (limite de Rozanov) et l'épaisseur réelle d'un absorbant pour juger de sa performance.

Les travaux présentés dans le troisième chapitre porte sur la conception systématique des absorbants radars large bande. Ils ont fait l'objet d'une publication dans le journal Progress In Electromagnetics Research C et intitulé 'Theoretical Analysis for Systematic Design of Flexible Broadband Radar Absorbers Using the Least-Square Method'. En effet, un outil analytique simple mais puissant pour la conception systématique des absorbants radars flexibles large bande est présenté. D'abord, les expressions permettant de calculer

les impédances réelles et imaginaires des FSS requises pour une absorption large bande en fonction de la permittivité et de l'épaisseur d'un diélectrique sur plan de masse sont données. On utilise le modèle de ligne de transmission (TLM) d'un absorbant radar pour associer la partie réelle de l'impédance requise à une résistance (élément discret) et sa partie imaginaire à une inductance et à un condensateur en série (élément discret). La Figure A.3 présente un absorbant radar est son modèle TLM équivalant. L'ensemble doit réaliser une adaptation à l'impédance de l'air; une partie réelle adaptée à 377 Ω et une partie imaginaire nulle. Nous avons montré qu'une absorption des ondes électromagnétiques large bande peut être obtenue en augmentant la valeur de la résistance dans le modèle de ligne de transmission (TLM).

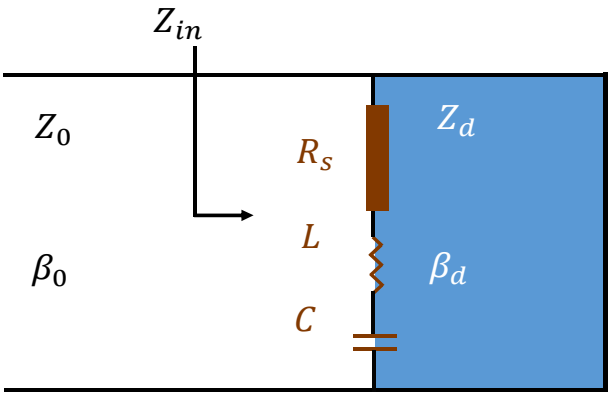

FIGURE A.3: TLM d'un absorbant radar.

Une formulation matricielle simple est utilisée pour obtenir les valeurs de L et C qui correspondent à la partie imaginaire requise de l'impédance aux limites inférieure et supérieure de la bande de fréquence étudiée. Une fois que tous les paramètres du TLM ont été déterminés, nous avons utilisé deux approches de modèle physique de patchs carrés pour concevoir des absorbants efficient. La première approche consiste à utiliser des patchs carrées métalliques imprimées sur un substrat diélectrique placé sur plan de masse (voir Figure A.4(b)). Les dimensions des patchs carrés et de la cellule unitaire donneront la partie imaginaire d'impédance requise. La partie réelle de l'impédance est obtenue en incluant des résistances (élément discret) dans les réseaux carrés. La deuxième, consiste à utiliser des films résistifs conçus comme des patchs carrés périodiques (voir Figure A.4(a)). Les dimensions des patchs carrés et de la cellule unitaire donneront la partie imaginaire d'impédance requise. La partie réelle requise de l'impédance est donnée par la valeur de résistance des films résistifs.

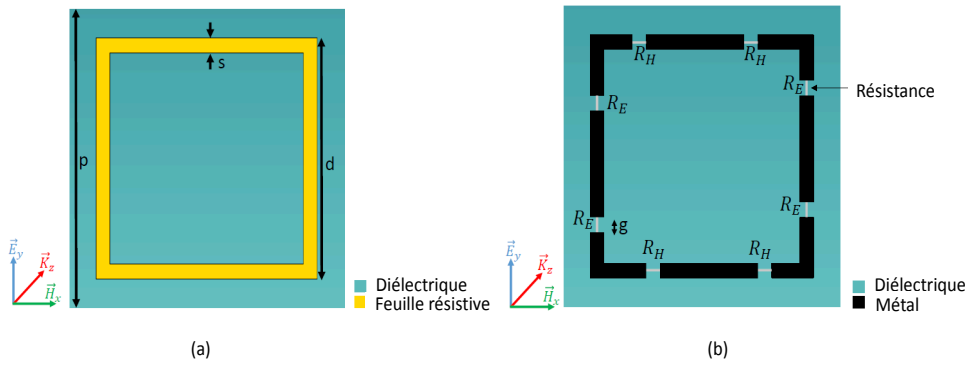

FIGURE A.4: (a) Vue de haut de l'absorbant radar dont les patchs carrés sont à base de feuille résistive. (b) Vue de haut de l'absorbant radar dont les patchs carrés sont à base de métal sur lequel on intègre des résistances.

Dans les deux cas, les réseaux carrés étant symétriques, on obtient des absorptions large bande pour les modes TE et TM. La bande d'absorption relative par rapport au centre de la bande atteint 88% pour une absorption de supérieure à 90%. Le ratio d'épaisseur théorique (limite de Rozanov) et réel est de 69,5%, ce qui rend la stratégie de conception proposée extrêmement intéressante. Les résulats du taux d'absorption en fonction de la fréquence sont présentés dans la Figure A.5 pour les modes TE et TM pour des incidences de 0 - 20°.

Dans ce chapitre la Signature Equivalante Radar (SER) monostatique de la structure proposée a également été simulée à certaines fréquences dans la bande d'absorption. Il a été démontré que la SER est considérablement réduite par rapport à une plaque métallique de même dimensions. Lorsque seule la plaque métallique est considérée, la SER monostatique en polarisation principale (co-polarisation) et pour une incidence normale est de -13.4 dBm^2, -12.8 dBm^2, -11.5 dBm^2, -8.7 dBm^2, -7.3 dBm^2 et -6.6 dBm^2 à 3, 4, 5, 6, 7 et 8 GHz, respectivement. Lorsque l'absorbant proposé est caractérisé, la signature équivalante radar monostatique en polarisation principale à incidence normale est réduite à -19.6 dBm^2, -23.3 dBm^2, -23.1 dBm^2, -30 dBm^2, -26.4 dBm^2, -13.4 dBm^2 pour 3, 4, 5, 6, 7 et 8 GHz, respectivement. Ces résultats de la signature équivalante radar monostatique sont présentés dans Figure A.6.

Le tableau A.1 récapitule les valeurs des simulations de signature équivalante radar monostatique en polarisation principale et polarisation croisée à incidence normale de la plaque métallique et de l'absorbant.

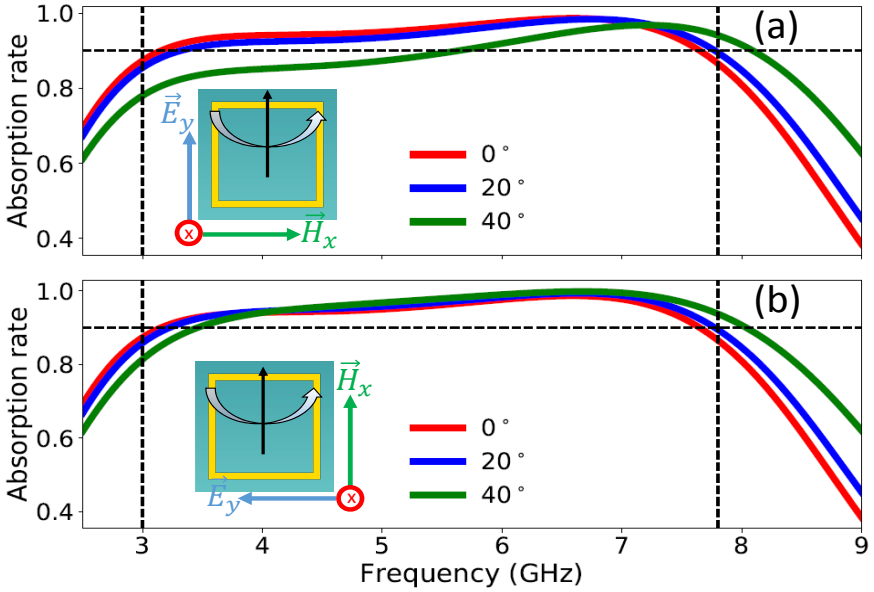

FIGURE A.5: Taux d'absorption en fonction de la fréquence pour des incidences 0 - 40°. (a) Polarisation TE. (b) Polarisation TM.

Objet	SER en polarisation principale à 3, 4, 5, 6, 7 et 8 GHz en (dBm^2)	SER en polarisation croisée à 3, 4, 5, 6, 7 et 8 GHz en (dBm^2)
Plaque métallique	-13.4, -12.8, -11.5, -8.7 , -7.3 et -6.6	≈ -90
Absorbant radar	-19.6, -23.3, -23.1, -30 , -26.4 et -13.4	≈ -90 ≈ -90

TABLE A.1: Récapitulatif des valeurs de signature équivalante radar.

La méthode de conception développée dans le Chapitre 3 est un outil puissant basé sur le modèle TLM avec un circuit résonant de type RLC. Les structures ainsi développées ne peuvent être que de formes géométriques 'simples' pour lesquelles la littérature scientifique donne des schémas électriques équivalents. Avec de telles structures, on recherche deux résonances distinctes et on optimise le tout pour couvrir toute la bande entre ces deux fréquences. Egalement, nous travaillons sur des éléments inductifs et capacitifs localisés entre les patchs carrés pour modifier électriquement la bande de fréquence d'absorption. Afin d'élargir la bande d'absorption, en continuant à utiliser des résonateurs, on doit rechercher des cellules ayant des résonances électriques et magnétiques multiples. Les structures et leurs couplages électromagnétiques avec le substrat diélectrique et intercouche, sont alors plus complexes et leur modéisation par le modèle TLM devient plus délicat, voire trop

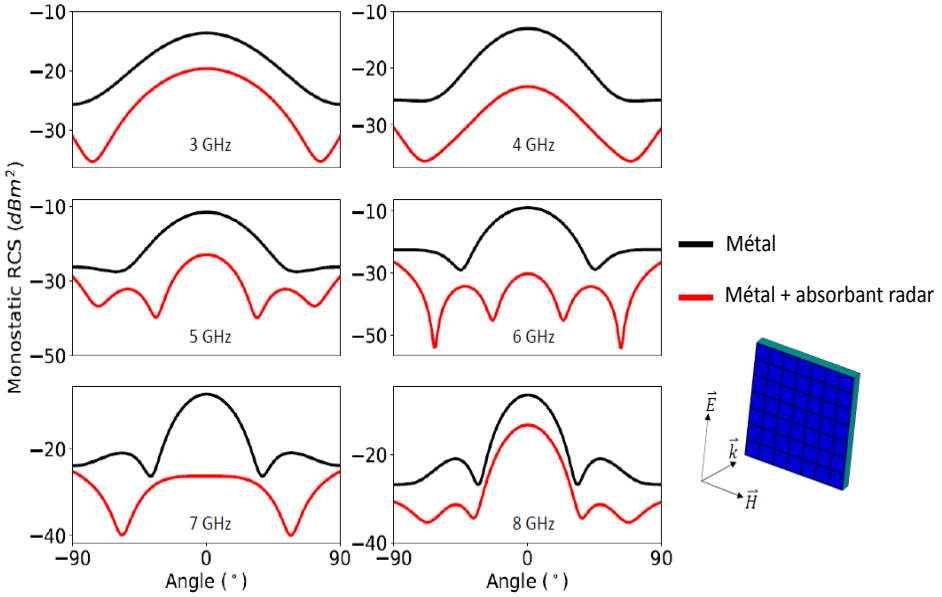

FIGURE A.6: SER du métal (noir) et de l'absorbant radar (rouge) à 3, 4, 5, 6, 7 et 8 GHz.

approximatif. La recherche de structures ayant de multiple résonances devra être faite par des simulations électromagnétiques 3D qui permettront de trouver des multiples couplages à travers des optisations. Ces travaux feront l'objet des Chapitres 4 et 5 suivants.

Les travaux du Chapitre 4 ont fait l'objet d'une publication intitulé 'A co-polarization broadband radar absorber for RCS reduction' publié dans le journal mdpi Materials. Nous développons une structure Métal-Isolant-Métal (MIM) avec une couche FSS unique. La structure présente une absorption en polarisation principale (co-polar) supérieure à 90% dans toute la bande de 5,6 GHz à 9,1 GHz. La structure proposée consiste en un résonateur en forme de U souligné (UUSR) déposé sur un diélectrique de 3.2 mm doublé par un plan de masse métallique. On utilise le substrat diéléctrique FR4 ayant une permittivité relative de $\epsilon = 3.92$ et de perte diélectrique $delta = 0.0025$ est utilisé pour le diélectrique. Les cellules unitaires sont agencées en périodes de 15 mm. Une image de la cellule élémentaire est présentée dans Figure A.7.

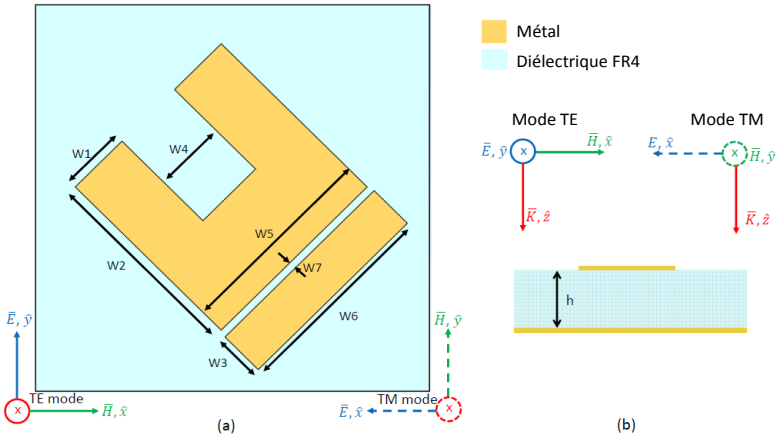

FIGURE A.7: (a) Vue du haut de la cellule élémentaire. (b) Vue de profil de la cellule élémentaire.

Dans un premier temps nous avons décrit la méthodologie de conception mise en place afin d'arriver à la structure finale. Nous avons discuté du mécanisme d'absorption en analysant la distribution des champs électriques et magnétiques. Un prototype de l'absorbant a été fabriqué et caractériser en chambre anéchoique Boris Vian. Les résultats des mesures sont en bon accord avec les résultats numériques comme on peut le l'observer dans la Figure A.8.

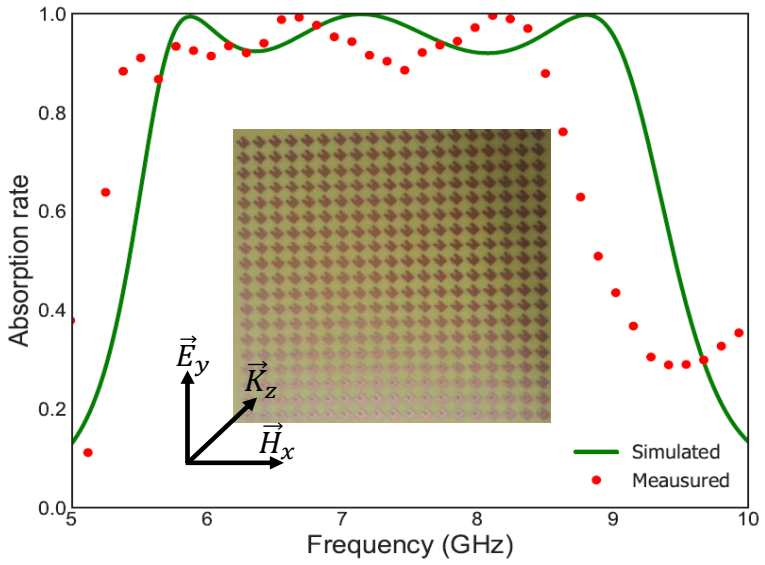

FIGURE A.8: Le taux d'absorption simulé (en vert) et mesuré (en rouge) d'un champ linéaire polarisé verticalement.

La structure MIM UUSR proposée a une épaisseur réel de 3.2 mm. Le ratio d'épaisseur théorique et réel (limite de Rozanov) et de 61%. Ce score est meilleur par rapport aux nombreuses structures publiées dans la littérture scientifique (Voir Tableau A.4). Une limitation importante de l'absorbant proposé est l'absorption en polarisation croisée qui est très faible liée de la rotation du UUSR de 45° et la périodicité de la structure. L'absorption en polarisation croisée reste très faible. L'absorption en polarisation principale reste dans ce cas élevé comme on peut l'observer dans la Figure Figure A.9.

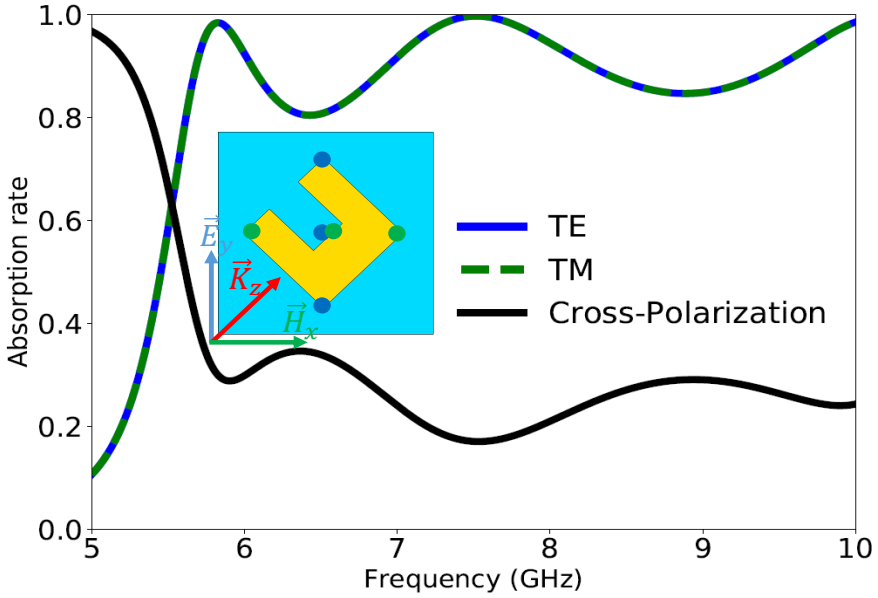

FIGURE A.9: Taux d'absorption en fonction de la fréquence pour les modes TE et TM et en polarisation croisée.

Les résultats de la simulation ont montré que, lorsque toute la structure est configurée non plus en réseau périodique mais suivant une configuration 'échiquier' ou 'damier', (voir Figure A.10(a)) le problème d'absorption en polarisation croisée peut être résolu. La signature équivalante radar a été simulée pour les trois fréquences de pic d'absorption et il a été démontré que la structure 'échiquier' réduit considérablement la signature équivalante radar en polarisation principale par rapport à une plaque métallique. Egalement la réduction de la signature équivalante radar en polarisation croisée est meilleure quand la structure finale est agencée en 'échiquier' que périodiquement. Lorsque seule la plaque métallique est considérée, la signature radar monostatique en polarisation principale pour une incidence normale est de 0 dBm^2, 1.7 dBm^2 et 3.6 dBm^2 à 5.87, 7.16 et 8.82 GHz, respectivement. Lorsque l'absorbant proposé (agencée en 'échiquier') est considéré, la signature radar monostatique à incidence normale diminue à -7.1 dBm^2, -2.9 dBm^2, -1.1 dBm^2 à 5.87, 7.16 et 8.82 GHz respectivement. Ces résultats de la signature équivalante radar monostatique sont présentés dans la Figure A.10(b).

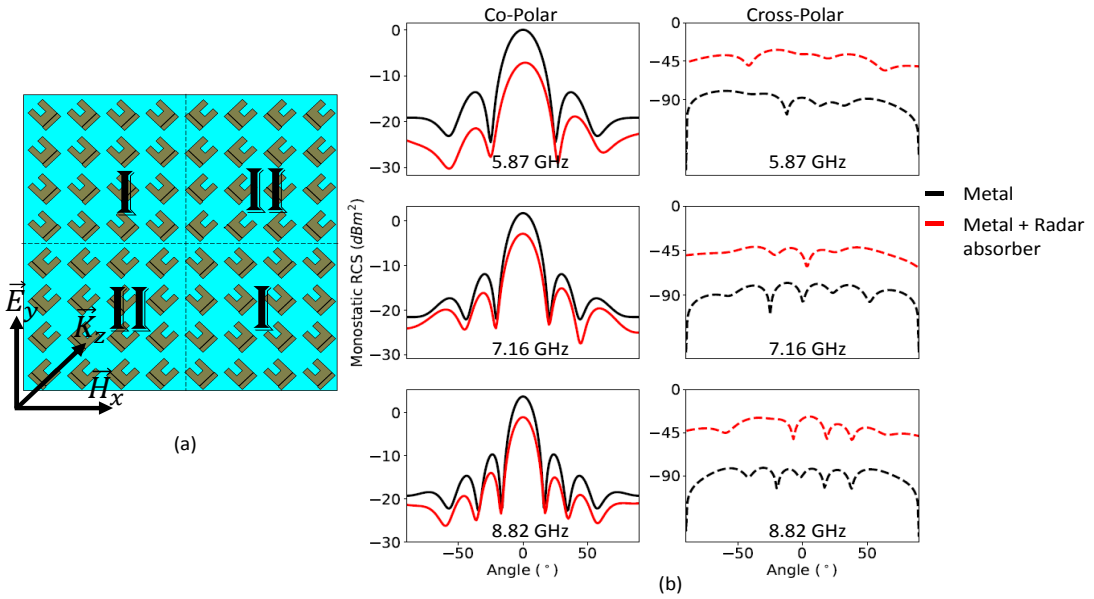

FIGURE A.10: (a)La structure complète agencée en 'échiquier'. (b) La signature équivalante radar monostatic à 5.87, 7.16 et 8.82 GHz d'une plaque métallique et de l'absorbant radar de mêmes dimensions. La première colonne représente la signature équivalante radar en polarisation principale et la deuxième colonne représente la signature radar en polarisation croisée.

Le tableau A.2 récapitule les valeurs des simulations de signature radar monostatique en polarisation principale et polarisation croisée à incidence normale de la plaque métallique et de l'absorbant.

Objet	SER en polarisation principale à 5.87, 7.16, et 8.82 GHz en (dBm^2)	SER en poalisation-croiséel à 5.87, 7.16, et 8.82 GHz en (dBm^2)
Plaque métallique	0, 1.7 et 3.6	≈ -90
Structure agncée périodiquement	11.3, -13.6 et -10.9	-2.27, 0 et 0
Structure agncée en 'échiquier'	-7.1, -2.9 et -1.1	-36.1, -59.5 et -28.3

TABLE A.2: Récapitulatif des valeurs de signature radar.

La configuration "échiquier" ou 'damier' de la structure sont en cours de fabriquation et les résultats de mesures seront présentés ultérieurement. Le Chapitre 5 présente les travaux sur la conception, optimisation, et caractérisation éxperimantale double couche (double MIM). L'objectif étant toujours l'élargissement de la bande d'absorption.

Les travaux sur cet absorbant double couche radar ultra-large bande montre que l'on peut atteindre au moins 89% d'absorption dans toute la bande de 4,8 GHz à 11,1 GHz. Ces travaux ont été publiés dans Nature Scientific Reports sous le titre de 'A dual layer broadband radar absorber to minimize electromagnetic interference in radomes' et sont décrites dans le chapitre 5. La cellule unitaire de l'absorbant à double couche proposée est présentée à la Figure A.11.

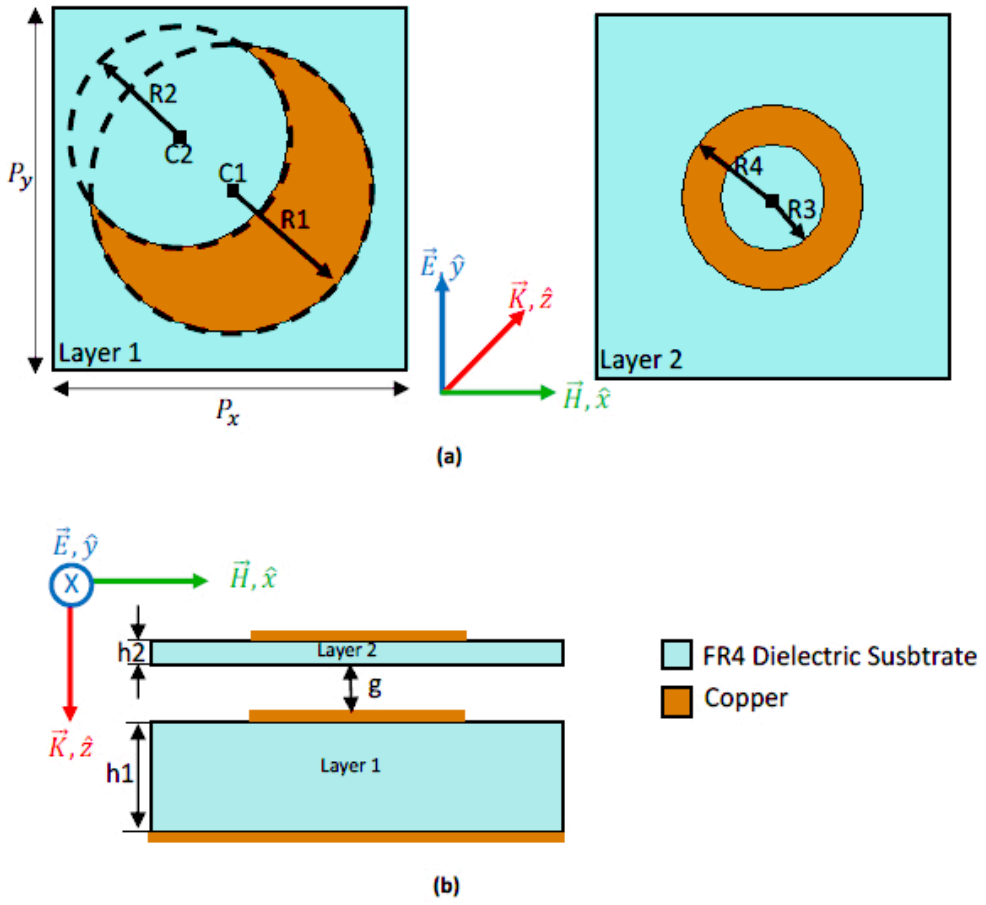

FIGURE A.11: (a) Vue du haut de la cellule élémentaire de la première couche avec le HMSR à gauche. Vue du haut de la cellule élémentaire de la deuxième couche avec le RSR à droite. (b) Vue de profil de la cellule élémentaire de l'ensemble de la structure.

L'absorbant est composé de deux couches séparées d'air d'une épaisseur de, g = 1.5 mm. Du FR4 ayant une permittivité relative de $\epsilon = 4.2$ et de perte diélectrique $delta = 0.018$ est utilisé pour les deux substrats diélectriques. La première couche de FR4, dont l'épaisseur, $h1$, est égale à 3.2 mm, est doublée d'un plan de masse pour empêcher la transmission. Sur la première couche, un résonateur en forme de demi-lune (HMSR) est déposé. Un résonateur en forme d'anneau (RSR) est déposé sur la deuxième couche de FR4 qui a une épaisseur, $h2$, égale à 0.5 mm. Les cellules unitaires (HMSR et RSR)

sont agencées périodiquements de période 13.75 mm. Dans un premier temps nous avons décrit la méthodologie afin d'arriver à la structure finale. Le mécanisme d'absorption de la structure a d'abord été décrit en étudiant la contribution de chaque couche, puis en observant la densité de perte de puissance, la distribution des champs électriques et magnétiques dans la structure. Ensuite, une étude paramétrique sur l'épaisseur du gap d'air entre les deux couches a complété les travaux pour mettre en évidence le couplage électriques et magnétiques. Dans cette partie, les impédances éffectives ont également été étudiées et utilisées pour comprendre les phénomènes physiques. Une autre étude paramétrique a été réalisée pour donner des épaisseurs optimisées des deux diélectriques et de l'épaisseur de l'air. Finalement, après avoir fabriqué et analysé la structure, les résultats mesurés se sont avérés très proches des résultats numériques comme on peut l'observer dans Figure A.12.

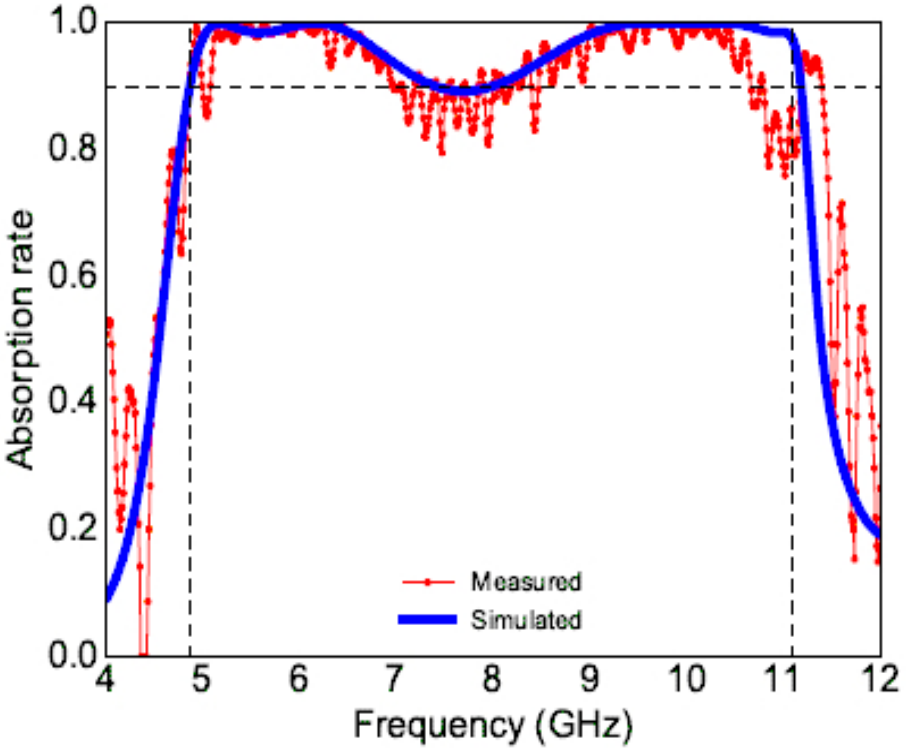

FIGURE A.12: Taux d'absorption en fonction de la fréquence. La courbe rouge représente les résultats de mesures et la courbe bleue représente les résultats de simulations.

La Figure A.13(a) représente une photo de la première couche, la Figure A.13(b) concerne la deuxième couche. La Figure A.13(c) est une photo de la structure entière est une photo de la campagne de mesure en chambre anéchoïque est présentée en A.13(d).

Les résultats expérimentaux sont très prometteurs et notre conception peut être utilisée pour traiter des problèmes de CEM pour des applications civiles et militaires. Un ratio

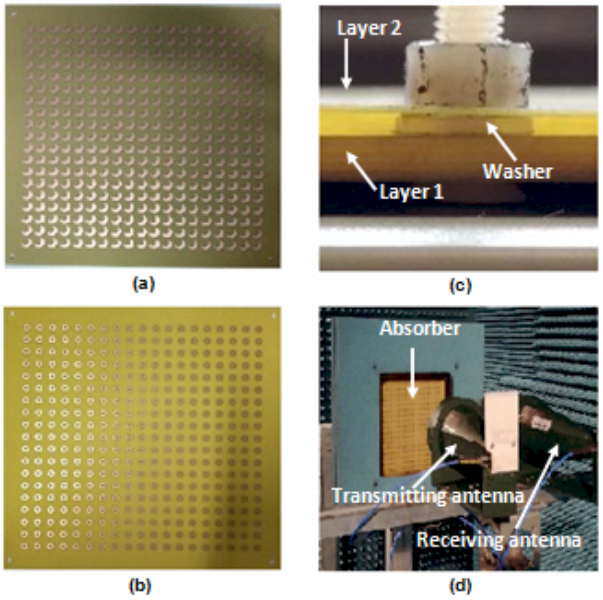

FIGURE A.13: (a) Vue du haut de la première couche. (b) Vue du haut de la deuxième couche. (c) Vue de profil de la structure complète. (d) Mesures en chambre anéchoïque.

d'épaisseur théorique et réel de 80% est obtenu, ce qui rend la structure très intéressante. Comme les travaux du chapitre 4, en raison de la rotation de 45% du HMSR, l'absorption en polarisation croisée est négligeable. Egalement, comme dans le chapitre 4, les résultats de la simulation ont également montré que, lorsque la première couche de la structure est configurée de manière'échiquier' ou 'damier', (voir Figure A.14(a)) le problème d'absorption en polarisation croisée peut être résolu et la signature radar peut être réduite de façon considérable. La signature équivalante radar a été simulée pour les trois fréquences de pic d'absorption et il a été démontré que la structure 'échiquier' réduit considérablement la signature équivalante radar en polarisation principale par rapport à une plaque métallique. Egalement la réduction de la signature équivalante radar en polarisation croisée est meilleure quand la structure finale est agencée en 'échiquier' que périodiquement. Lorsque seule la plaque métallique est considérée, la signature équivalante radar monostatique en polarisation principale pour une incidence normale est de -1.3 dBm^2, 0.67 dBm^2 et 4.9 dBm^2 à 5.17, 6.16 et 10 GHz, respectivement. Lorsque l'absorbant proposé (la première couche agencée en 'échiquier') est considéré, la signature équivalante radar monostatique à incidence normale diminue à -19.1 dBm^2, -8.2 dBm^2, -8.1 dBm^2 à 5.17, 6.16 et 10 GHz respectivement. Ces résultats de la signature équivalante radar monostatique sont présentés dans la Figure A.14(b).

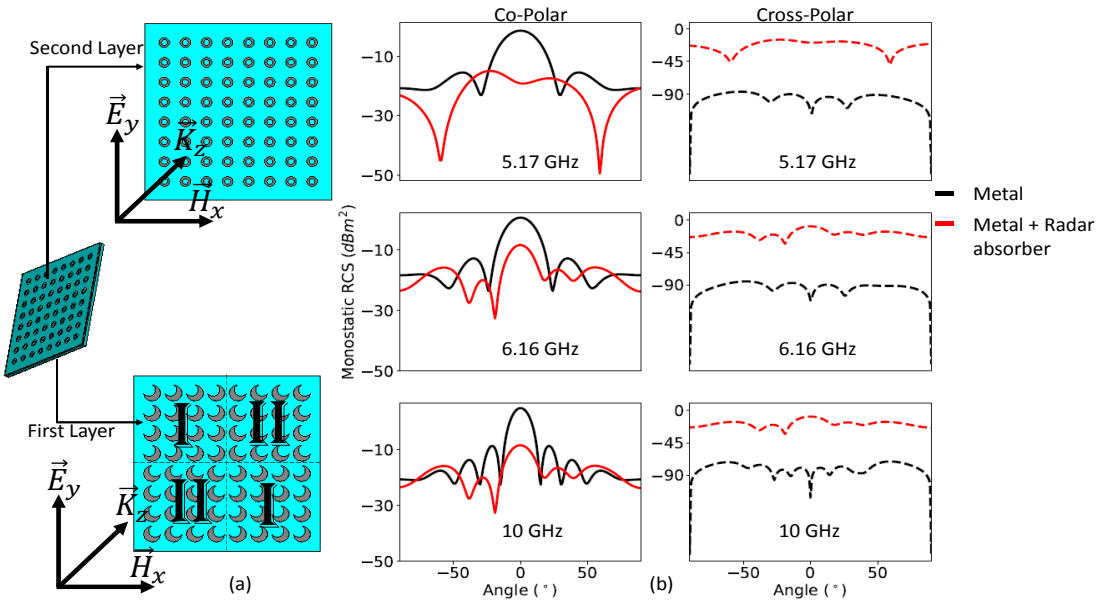

FIGURE A.14: (a)La structure complète dont la premère couche est agencée en 'échiquier'. (b) La signature équivalante radar monostatic à 5.17, 6.16 et 10 GHz d'une plaque métallique et de l'absorbant radar de mêmes dimensions. La première colonne représente la signature équivalante radar en polarisation principale et la deuxième colonne représente la signature équivalante radar en polarisation croisée.

Le tableau A.3 récapitule les valeurs des simulations de signature équivalante radar monostatique en polarisation principale et polarisation croisée à incidence normale de la plaque métallique et de l'absorbant.

Objet	SER en polarisation principale à 5.17, 6.16, et 10 GHz en (dBm^2)	SER en poalisation-croiséel à 5.17, 6.16, et 10 GHz en (dBm^2)
Plaque métallique	-1.3, 0.62 et 4.9	≈ -90
Structure agncée périodiquement	15.5, 20.5 et -16.6	-1.8, 0 et 3.2
Structure agncée en 'échiquier'	-19.1, -8.2 et -8.1	-20.2, -9.18 et -8.3

TABLE A.3: Récapitulatif des valeurs de signature équivalante radar.

Nous avons montré dans ce chapitre que l'utilisation de plusieurs couches peut augmenter la largeur de bande d'absorption. Si l'élément résonant est bien optimisé, l'épaisseur de l'absorbant radar peut être très proche de l'épaisseur théorique. Comme pour la couche unique du chapitre 4, la configuration en 'échiquier' de la structure complète est en cours de fabrication. Dans un avenir proche, nous aimerions caractériser éxpérimentalement la structure configurée en 'échiquier' et mesurer sa signature équivalante radar.

Nous avons également comparé la performance sur le rapport des épaisseurs (ratio d'épaisseur théorique et réel) de nos absorbants à d'autres absorbants de la littérature scientifique. Le tableau A.4 donne les résultats de cette comparaison. L'absorbant radar présenté dans le Chapitre 5 a la meilleur performance.

Absorbant radar	**Fréquence** (GHz)	**Epaisseur théorique,** t_T	**Epaisseur réel,** t_R	(t_T/t_R)***100**
[70]	5 - 25	2.55 mm	3.65 mm	69.86 %
[110]	6 - 19	3.43 mm	4.36 mm	78.57 %
[111]	4 - 15	1.206 mm	1.54 mm	78.31 %
[112]	4 - 8	1.237 mm	1.6 mm	77.31 %
[113]	40 - 134	0.294 mm	1 mm	29.4 %
[114]	6- 18	1.64 mm	2.22 mm	73.78 %
$\lambda/4$ Magneto-dielectrique	1 - 20	12.6 mm	25 mm	50.4 %
Salisbury screen	1 - 10	3.43 mm	15 mm	22.8%
Nos travaux (Chapitre 3)	2.5 - 9	5.57 mm	8 mm	69.5%
Nos travaux (Chapitre 4)	5 - 10	1.95 mm	3.2 mm	61%
Nos travaux (Chapitre 5)	4 - 12	4.16 mm	5.2 mm	80%

TABLE A.4: Comparaison des absorbants larges bandes.

A ce niveau de nos travaux, on peut voir que les structures développées sont toutes planaires. Il est possible de les conformer avec des rayons de courbure faibles à cause de la réponse angulaire étudiée dans les chapitres 2, 3, 4 et 5. Dans le cas d'une cible cylindrique, le rayon de la cible doit être très grand par rapport à la longueur d'onde de l'espace libre si l'on souhaite utiliser des absorbants radars planairs conformés. Si le rayon de la cible cylindrique est comparable ou inférieur à la longueur d'onde de fonctionnement, les absorbants radars conçus pour les cibles planairs ne conviennent plus. Lorsqu'un corps cylindrique métallique est illuminé par une onde électromagnétique (EM), celle-ci le rayonnera (réflexions, diffractions) dans toutes les directions autour du corps. Les amplitudes des champs rayonnés dépendent du rayon du corps cylindrique comme on peut le voir sur la Figure A.15. La Figure A.15 montre les SER bistatiques normalisés pour trois cas de cylindres métalliques illuminés par une onde EM plane. On peut voir que le cylindre de très grand rayon par rapport à la longueur d'onde réfléchit toute la puissance émise.

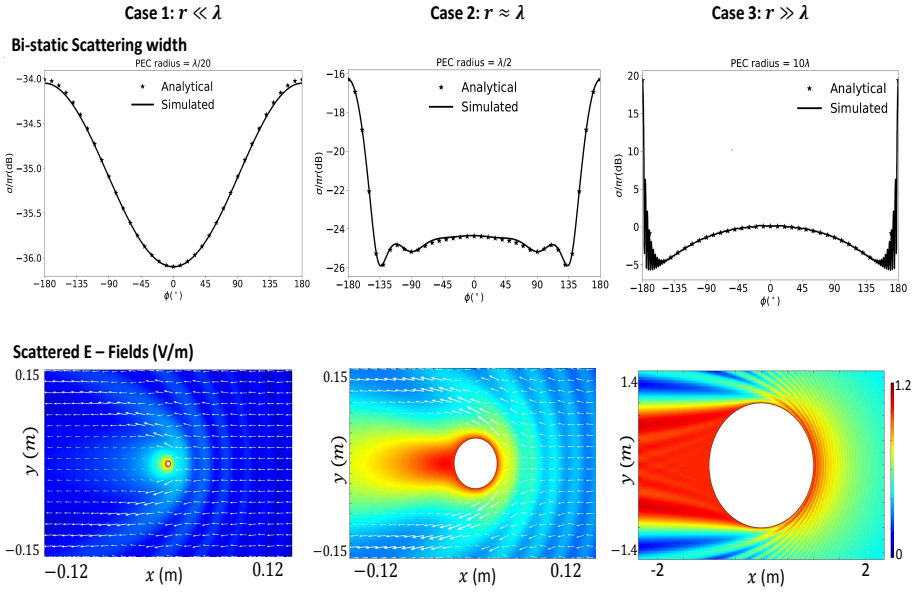

FIGURE A.15: Rayonnement d'un cylindre métallique lorsque celui ci est illuminé par une onde électromagnétique. Le cas où le champs E est parallèle à la hauteur du cylindre est considéré. Trois cas sont présenté: (1) lorsque le rayon du cylindre est très petite par rapport à la longueur d'onde. (2) Lorsque le rayon du cylindre est compable à la longueur d'onde. (3) Lorsque le rayon du cylindre est très grand par rapport à la longueur d'onde.

Selon les applications, les champs EM dispersés peuvent être plus ou moins critiques. Dans le Chapitre 6, une étude théorique complète sur l'utilisation des dielectriques sectoriels (revêtement non homogène) pour couvrir l'absorption d'une cible cylindrique. Cette étude montre que le revêtement avec des secteurs de diélectriques (revêtement non homogène) placé autour d'un cylindre parfaitement conducteur de rayon est comparable à λ, permet de réduire considérablement le rayonnement sans l'utilisation des matériaux actifs. Le rayonnement normalisé vers l'avant peut être réduit de 80% dans le cas où le cylindre métallique est revêtu de 16 secteurs optimisés (Voir Figure A.16). Dans ce cas, le rayonnement totale (moyenne du rayonnement dans toutes les directions) est réduit de 82% par rapport au rayonnement du cylindre métallique revêtu par le revêtement homogène optimisé pour réduire les réflexions.

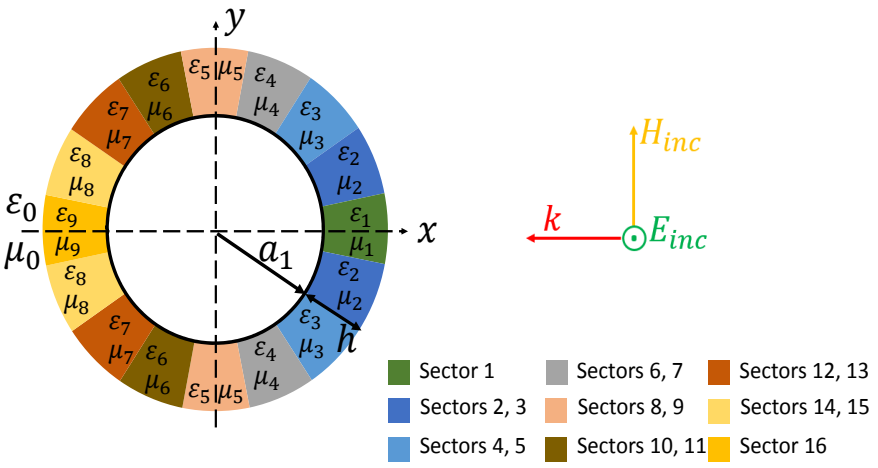

FIGURE A.16: Un cylindre métallique de rayon $a_1 = \lambda/2$ entouré de 16 secteurs de diélectrique ayant une épaisseur de $h = \lambda/5$, illuminé par une onde polarisée verticalement.

Les résultats de simulation de la signature équivalante radar bistatique d'un cylindre métallique et lorsque celui-ci est entouré d'un revêtement inhommogène de 16 secteurs sont présentés dans la Figure A.17.

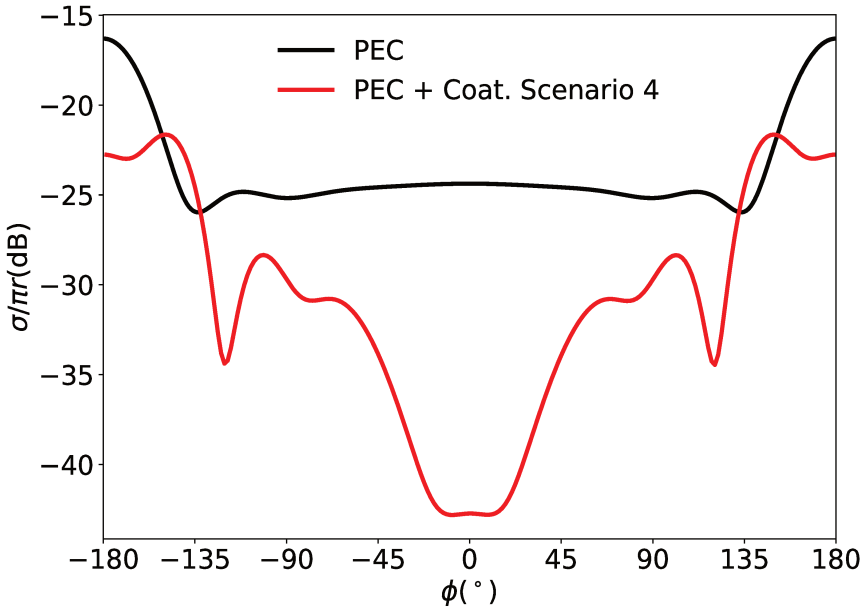

FIGURE A.17: Signature équivalante radar bistatique normalisée d'un cylindre métallique de rayon $\lambda/2$ (en noire) and avec le revêtement de 16 secteurs (en rouge). Les simulations ont été réalisés à 3 GHz.

Les résultats de la signature équivalante radar bistatic normalisée peuvent également être présentés sous forme triangulaire (Figure A.18). En abscisse $x > 0$, on présente le rayonnement vers l'avant, en abscisse $x < 0$ on présente la réflexion. En ordonnée $y > 0$, le rayonnement total est présenté. Cette présentation permet, en un coup d'oeil de pouvoir comparer plus facilement les différentes composantes du rayonnement (arrière, avant, total). Il sera également facile de comparer les différents revêtements entres eux et d'avoir une idée si elles se rapprochent d'un système de cloaking (invisibilité).

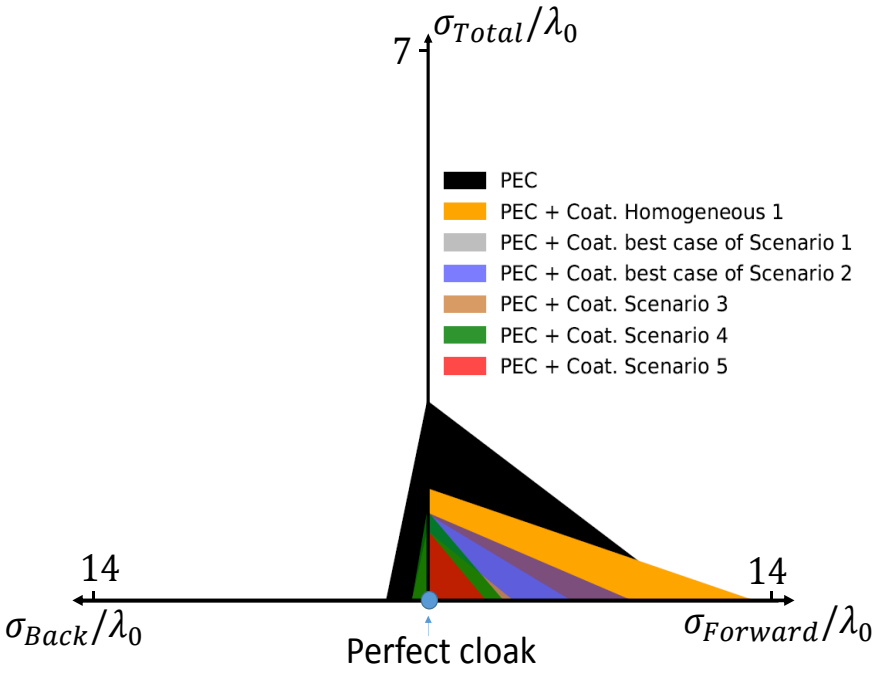

FIGURE A.18: Représentation triangulaire du rayonnement vers la source (σ_{Back}), rayonnement vers l'avant ($\sigma_{Forward}$) et le rayonnement total (σ_{Total}) pour un cylindre métallique, et quand il est couvert par plusieurs scénarios de revêtements.

Pour le développement de ce concept, nous travaillons sur des bandes étroites. Un travail d'optimisation supplémentaire peut être effectué afin de réduire la réflexion, le rayonnement vers l'avant et le rayonnement total pour une gamme de fréquences plus large bande. Pour nos études, l'épaisseur de chaque secteurs est fixée à $\lambda/5$ et nous recherchons par optimisation les permittivités complexes associées. Cependant, dans certains cas, les valeurs des permittivités complexes obtenues sont non disponibles facilement dans le commerce. Dans ce cas, nous revenons sur la méthode de conception pour fixer la permittivité et donc optimiser les épaisseurs des différentes secteurs.

La prochaine étape consiste à réaliser un prototype de ce nouveau dispositif et de le tester en chambre anéchoïque. La validation des résultats de mesures de ce dispositif sera un résultat remarquable des travaux de cette thèse. Notons qu'à plus long terme il sera intéressant de tester tous les absorbants dévelopés, en environement réel dans les navires du constructeur CMN.

Appendix B

Publications

- **Publications in journals**

  - Beeharry, Thtreswar, Kamardine Selemani, and Habiba Hafdallah Ouslimani. 'Theoretical Analysis for Systematic Design of Flexible Broadband Radar Absorbers Using the Least-Square Method.' Progress In Electromagnetics Research 87 (2018): 175-186.

  - Beeharry, Thtreswar, et al. 'A Co-Polarization Broadband Radar Absorber for RCS Reduction.' Materials 11.9 (2018): 1668.

  - Beeharry, Thtreswar, et al. 'A dual layer broadband radar absorber to minimize electromagnetic interference in radomes.' Scientific reports 8.1 (2018): 382.

- **Publications in conferences**

  - Thtreswar Beeharry, Riad Yahiaoui, Kamardine Selemani, Habiba Ouslimani. 'Broadband radar absorbers based on periodic structures', IEEE CAMA, Sweden, 2018.

  - Thtreswar Beeharry, Riad Yahiaoui, Kamardine Selemani, Habiba Ouslimani. 'A Broadband Metamaterial Based Radar Absorber', IEEE EUCAP, London, 2018.

- Yahiaoui, R., Beeharry, T., Burokur, S. N., Grassin, P., Ouslimani, H. H. (2017, March). 'Metasurfaces with positive reflection phase gradients for broadband directive emission', IEEE EUCAP, 2017, Paris.

- Yahiaoui, Riad, Habiba Hafdallah Ouslimani, and Thtreswar Beeharry. "Broadband cavity antennas with highly directive emissions." IEEE CAMA, 2016, New York.

Bibliography

[1] Serdukov, A., Semchenko, Igor, Tertyakov, S., et al. Electromagnetics of bi-anisotropic materials-Theory and Application. Gordon and Breach science publishers, 2001.

[2] Varadan, V. K., Varadan, V. V., Ma, Y., Hall, W. F. (1986). Design of ferrite-impregnated plastics (PVC) as microwave absorbers. IEEE transactions on microwave theory and techniques, 34(2), 251-258.

[3] Salisbury, W. W. (1952). U.S. Patent No. 2,599,944. Washington, DC: U.S. Patent and Trademark Office.

[4] Fante, R. L.,Mccormack, M. T. (1988). Reflection properties of the Salisbury screen. IEEE transactions on antennas and propagation, 36(10), 1443-1454.

[5] Chambers, B. (1994). Optimum design of a Salisbury screen radar absorber. Electronics Letters, 30(16), 1353-1354.

[6] Munk, B. A., Munk, P., Pryor, J. (2007). On designing Jaumann and circuit analog absorbers (CA absorbers) for oblique angle of incidence. IEEE Transactions on Antennas and Propagation, 55(1), 186-193.

[7] Du Toit, L. J. (1994). The design of Jauman absorbers. IEEE Antennas and Propagation Magazine, 36(6), 17-25.

[8] Munk, B. A., Munk, P.,Pryor, J. (2007). On designing Jaumann and circuit analog absorbers (CA absorbers) for oblique angle of incidence. IEEE Transactions on Antennas and Propagation, 55(1), 186-193.

[9] https://www.imperial.ac.uk/electrical-engineering/research/optical-and-semiconductor-devices/research/rf-metamaterials/

[10] Grbic, Anthony et Eleftheriades, George V. Experimental verification of backward-wave radiation from a negative refractive index metamaterial. Journal of Applied Physics, 2002, vol. 92, no 10, p. 5930-5935.

[11] Smith, D. R., Pendry, J. B., Wiltshire, M. C. (2004). Metamaterials and negative refractive index. Science, 305(5685), 788-792.

[12] Dolling, G., Enkrich, C., Wegener, M., Soukoulis, C. M., Linden, S. (2006). Low-loss negative-index metamaterial at telecommunication wavelengths. Optics letters, 31(12), 1800-1802.

[13] Valentine, Jason, Zhang, Shuang, Zentgraf, Thomas, et al. Three-dimensional optical metamaterial with a negative refractive index. nature, 2008, vol. 455, no 7211, p. 376.

[14] Hao, Jiaming, Yuan, Yu, Ran, Lixin, et al. Manipulating electromagnetic wave polarizations by anisotropic metamaterials. Physical review letters, 2007, vol. 99, no 6, p. 063908.

[15] Kabishin, A. V., Evans, P., Pastkovsky, S., et al. Plasmonic nanorod metamaterials for biosensing. Nature materials, 2009, vol. 8, no 11, p. 867.

[16] Soukoulis, Costas M. et Wegener, Martin. Past achievements and future challenges in the development of three-dimensional photonic metamaterials. Nature Photonics, 2011, vol. 5, no 9, p. 523.

[17] Poddubny, Alexander, Iorish, Ivan, Belov, Pavel, et al. Hyperbolic metamaterials. Nature Photonics, 2013, vol. 7, no 12, p. 948.

[18] Nicholls, Luke H., Rodriguez-Fortuno, Francisco J., Nasir, Mazhar E., et al. Ultrafast synthesis and switching of light polarization in nonlinear anisotropic metamaterials. Nature Photonics, 2017, vol. 11, no 10, p. 628.

[19] Zhang, S., Park, Y. S., Li, J., Lu, X., Zhang, W., Zhang, X. (2009). Negative refractive index in chiral metamaterials. Physical review letters, 102(2), 023901.

[20] Plum, E., Zhou, J., Dong, J., Fedotov, V. A., Koschny, T., Soukoulis, C. M., Zheludev, N. I. (2009). Metamaterial with negative index due to chirality. Physical Review B, 79(3), 035407.

[21] Plum, E. (2010). Chirality and metamaterials (Doctoral dissertation, University of Southampton).

[22] Zhao, Y., Askarpour, A. N., Sun, L., Shi, J., Li, X., Alu, A. (2017). Chirality detection of enantiomers using twisted optical metamaterials. Nature communications, 8, 14180.

[23] LI, Wei, Coppens, Zachary J., Besteiro, Lucas V., et al. Circularly polarized light detection with hot electrons in chiral plasmonic metamaterials. Nature communications, 2015, vol. 6, p. 8379.

[24] Schurig, D., Mock, J. J., Justice, B. J., Cummer, S. A., Pendry, J. B., Starr, A. F., Smith, D. R. (2006). Metamaterial electromagnetic cloak at microwave frequencies. Science, 314(5801), 977-980.

[25] Sihvola, A. (2007). Metamaterials in electromagnetics. Metamaterials, 1(1), 2-11.

[26] Gu, J., Singh, R., Liu, X., Zhang, X., Ma, Y., Zhang, S., . Taylor, A. J. (2012). Active control of electromagnetically induced transparency analogue in terahertz metamaterials. Nature communications, 3, 1151.

[27] Young, K. L., Ross, M. B., Blaber, M. G., Rycenga, M., Jones, M. R., Zhang, C., . Mirkin, C. A. (2014). Using DNA to design plasmonic metamaterials with tunable optical properties. Advanced Materials, 26(4), 653-659.

[28] Evlyukhin, A. B., Novikov, S. M., Zywietz, U., Eriksen, R. L., Reinhardt, C., Bozhevolnyi, S. I., Chichkov, B. N. (2012). Demonstration of magnetic dipole resonances of dielectric nanospheres in the visible region. Nano letters, 12(7), 3749-3755.

[29] Kuznetsov, A. I., Miroshnichenko, A. E., Fu, Y. H., Zhang, J., Luk'Yanchuk, B. (2012). Magnetic light. Scientific reports, 2, 492.

[30] Monticone, F., Alù, A. (2014). The quest for optical magnetism: from split-ring resonators to plasmonic nanoparticles and nanoclusters. Journal of Materials Chemistry C, 2(43), 9059-9072.

[31] Verre, R., Yang, Z. J., Shegai, T., Kall, M. (2015). Optical magnetism and plasmonic Fano resonances in metal–insulator–metal oligomers. Nano letters, 15(3), 1952-1958.

[32] Hao, J., Yuan, Y., Ran, L., Jiang, T., Kong, J. A., Chan, C. T., Zhou, L. (2007). Manipulating electromagnetic wave polarizations by anisotropic metamaterials. Physical review letters, 99(6), 063908.

[33] Grady, N. K., Heyes, J. E., Chowdhury, D. R., Zeng, Y., Reiten, M. T., Azad, A. K., . Chen, H. T. (2013). Terahertz metamaterials for linear polarization conversion and anomalous refraction. Science, 1235399.

[34] Chen, H., Chan, C. T. (2007). Acoustic cloaking in three dimensions using acoustic metamaterials. Applied physics letters, 91(18), 183518.

[35] Pfeiffer, C., Grbic, A. (2013). Metamaterial Huygens' surfaces: tailoring wave fronts with reflectionless sheets. Physical review letters, 110(19), 197401.

[36] Metz, C. (2005). U.S. Patent No. 6,958,729. Washington, DC: U.S. Patent and Trademark Office.

[37] Tretyakov, S. A., Ermutlu, M. (2005). Modeling of patch antennas partially loaded with dispersive backward-wave materials. IEEE Antennas and Wireless Propagation Letters, 4(1), 266-269.

[38] Tran, C. M., Hafdallah-Ouslimani, H., Zhou, L., Priou, A. C., Teillet, H., Daden, J. Y., Ourir, A. (2010). High impedance surfaces based antennas for high data rate communications at 40 GHz. Progress In Electromagnetics Research, 13, 217-229.

[39] Ourir, A., Ouslimani, H. H. (2011). Negative refractive index in symmetric cut-wire pair metamaterial. Applied Physics Letters, 98(11), 113505.

[40] Johnson, M. C., Brunton, S. L., Kundtz, N. B., Kutz, J. N. (2015). Sidelobe canceling for reconfigurable holographic metamaterial antenna. IEEE Transactions on Antennas and Propagation, 63(4), 1881-1886.

[41] Brookner, E. (2017). Metamaterial advances for radar and communications.

[42] Tretyakov, S. A., Maslovski, S. I. (2003). Thin absorbing structure for all incidence angles based on the use of a high-impedance surface. Microwave and Optical Technology Letters, 38(3), 175-178.

[43] Watts, C. M., Liu, X., Padilla, W. J. (2012). Metamaterial electromagnetic wave absorbers. Advanced materials, 24(23), OP98-OP120.

[44] Landy, N. I., Sajuyigbe, S., Mock, J. J., Smith, D. R., Padilla, W. J. (2008). Perfect metamaterial absorber. Physical review letters, 100(20), 207402.

[45] Tao, H., Bingham, C. M., Strikwerda, A. C., Pilon, D., Shrekenhamer, D., Landy, N. I., Averitt, R. D. (2008). Highly flexible wide angle of incidence terahertz metamaterial absorber: Design, fabrication, and characterization. physical review B, 78(24), 241103.

[46] Beeharry, T., Yahiaoui, R., Selemani, K., Ouslimani, H. H. (2018). A dual layer broadband radar absorber to minimize electromagnetic interference in radomes. Scientific reports, 8(1), 382.

[47] Beeharry, T., Yahiaoui, R., Selemani, K., Ouslimani, H. H. A Co-Polarization Broadband Radar Absorber for RCS Reduction. Materials 2018, 11(9).

[48] Fang, N., Zhang, X. (2002). Imaging properties of a metamaterial superlens. In Nanotechnology, 2002. IEEE-NANO 2002. Proceedings of the 2002 2nd IEEE Conference on (pp. 225-228). IEEE.

[49] Zhang, X., Liu, Z. (2008). Superlenses to overcome the diffraction limit. Nature materials, 7(6), 435.

[50] Wong, Z. J., Wang, Y., O'Brien, K., Rho, J., Yin, X., Zhang, S.,. Zhang, X. (2017). Optical and acoustic metamaterials: superlens, negative refractive index and invisibility cloak. Journal of Optics, 19(8), 084007.

[51] Tretyakov, S., Alitalo, P., Luukkonen, O., Simovski, C. (2009). Broadband electromagnetic cloaking of long cylindrical objects. Physical review letters, 103(10), 103905.

[52] Monti, A., Soric, J. C., Alù, A., Toscano, A., Bilotti, F. (2015). Anisotropic mantle cloaks for TM and TE scattering reduction. IEEE Transactions on Antennas and Propagation, 63(4), 1775-1788.

[53] Ni, X., Wong, Z. J., Mrejen, M., Wang, Y., Zhang, X. (2015). An ultrathin invisibility skin cloak for visible light. Science, 349(6254), 1310-1314.

[54] Sounas, D. L., Fleury, R., Alù, A. (2015). Unidirectional cloaking based on metasurfaces with balanced loss and gain. Physical Review Applied, 4(1), 014005.

[55] Werner, D. H., Kwon, D. H. (2015). Transformation electromagnetics and metamaterials. Springer.

[56] Pendry, J., Smith, D., Schurig, D. (2017). U.S. Patent No. 9,677,856. Washington, DC: U.S. Patent and Trademark Office.

[57] Munk, B. A. (2005). Frequency selective surfaces: theory and design. John Wiley and Sons.

[58] Sievenpiper, D. F. (2012). U.S. Patent No. 8,339,320. Washington, DC: U.S. Patent and Trademark Office.

[59] Ade, P. A., Pisano, G., Tucker, C.,and Weaver, S. (2006, June). A review of metal mesh filters. In Millimeter and Submillimeter Detectors and Instrumentation for Astronomy III (Vol. 6275, p. 62750U). International Society for Optics and Photonics.

[60] Monorchio, A., Manara, G., Serra, U., Marola, G., and Pagana, E. (2005). Design of waveguide filters by using genetically optimized frequency selective surfaces. IEEE Microwave and Wireless Components Letters, 15(6), 407-409.

[61] Sarabandi, K., and Behdad, N. (2007). A frequency selective surface with miniaturized elements. IEEE Transactions on Antennas and Propagation, 55(5), 1239-1245.

[62] Zabri, S. N., Cahill, R., Schuchinsky, A. (2015). Compact FSS absorber design using resistively loaded quadruple hexagonal loops for bandwidth enhancement. Electronics Letters, 51(2), 162-164.

[63] Wang, H., Kong, P., Cheng, W., Bao, W., Yu, X., Miao, L., and Jiang, J. (2016). Broadband tunability of polarization-insensitive absorber based on frequency selective surface. Scientific reports, 6, 23081.

[64] Ghosh, S., Srivastava, K. V. (2015). An equivalent circuit model of FSS-based metamaterial absorber using coupled line theory. IEEE Antennas and Wireless Propagation Letters, 14, 511-514.

[65] Wang, M., Huang, C., Pu, M., and Luo, X. (2015). Reducing side lobe level of antenna using frequency selective surface superstrate. Microwave and Optical Technology Letters, 57(8), 1971-1975.

[66] Stefanelli, R., Trinchero, D. (2010, April). Reduction of electromagnetic interference by means of frequency selective devices. In Telecommunications (ICT), 2010 IEEE 17th International Conference on (pp. 239-243). IEEE.

[67] Costa, F., Genovesi, S., Monorchio, A., Manara, G. (2014). Low-cost metamaterial absorbers for sub-GHz wireless systems. IEEE Antennas and Wireless Propagation Letters, 13, 27-30.

[68] Wang, X. C., Díaz-Rubio, A., Sneck, A., Alastalo, A., Mäkelä, T., Ala-Laurinaho, J.,. Tretyakov, S. A. (2018). Systematic design of printable metasurfaces: Validation through reverse-offset printed millimeter-wave absorbers. IEEE Transactions on Antennas and Propagation, 66(3), 1340-1351.

[69] Wang, N., Tong, J., Zhou, W., Jiang, W., Li, J., Dong, X., & Hu, S. (2015). Novel quadruple-band microwave metamaterial absorber. IEEE Photonics Journal, 7(1), 1-6.

[70] Xiong, H., Hong, J. S., Luo, C. M., & Zhong, L. L. (2013). An ultrathin and broadband metamaterial absorber using multi-layer structures. Journal of Applied Physics, 114(6), 064109.

[71] Grant, J., Ma, Y., Saha, S., Khalid, A. Cumming, D. R. Polarization insensitive, broadband terahertz metamaterial absorber. Opt.letters 36, 3476–3478 (2011).

[72] Sood, D. Tripathi, C. C. Broadband ultrathin low-profile metamaterial microwave absorber. Appl. Phys. A 122, 332 (2016).

[73] Langley, R. J. Parker, E. A. Double-square frequency-selective surfaces and their equivalent circuit. Electron. Lett. 19, 675–677 (1983).

[74] Jing, L. et al. Chiral metamirrors for broadband spin-selective absorption. Appl. Phys. Lett. 110, 231103 (2017).

[75] Chakravarty, S., Mittra, R. Williams, N. R. Application of a microgenetic algorithm (mga) to the design of broadband microwave absorbers using multiple frequency selective surface screens buried in dielectrics. IEEE Transactions on Antennas Propag. 50, 284–296 (2002).

[76] Park, K.-Y., Lee, S.-E., Kim, C.-G. Han, J.-H. Fabrication and electromagnetic characteristics of electromagnetic wave absorbing sandwich structures. Compos. science technology 66, 576–584 (2006).

[77] Ghosh, S., Bhattacharyya, S. Srivastava, K. V. Design, characterisation and fabrication of a broadband polarisation-insensitive multi-layer circuit analogue absorber. IET Microwaves, Antennas and Propag. 10, 850–855 (2016).

[78] Osipov, A. V., Tretyakov, S. A. (2017). Modern Electromagnetic Scattering Theory with Applications. John Wiley and Sons.

[79] Rozanov, K. N. Ultimate thickness to bandwidth ratio of radar absorbers. IEEE Transactions on Antennas Propag. 48, 1230–1234 (2000).

[80] Costa, F., Monorchio, A., & Manara, G. (2014). An overview of equivalent circuit modeling techniques of frequency selective surfaces and metasurfaces. Appl. Comput. Electromagn. Soc. J., 29(12), 960-976.

[81] Kern, D. J., & Werner, D. H. (2003). A genetic algorithm approach to the design of ultra-thin electromagnetic bandgap absorbers. Microwave and Optical Technology Letters, 38(1), 61-64.

[82] Jiang, Z. H., Yun, S., Toor, F., Werner, D. H., & Mayer, T. S. (2011). Conformal dual-band near-perfectly absorbing mid-infrared metamaterial coating. ACS nano, 5(6), 4641-4647.

[83] Jafar-Zanjani, S., Inampudi, S., & Mosallaei, H. (2018). Adaptive Genetic Algorithm for Optical Metasurfaces Design. Scientific reports, 8(1), 11040.

[84] Beeharry, T., Selemani, K., & Ouslimani, H. H. (2018). Theoretical Analysis for Systematic Design of Flexible Broadband Radar Absorbers Using the Least-Square Method. Progress In Electromagnetics Research, 87, 175-186.

[85] Lee, Dongju, et al. Optimal parameter retrieval for metamaterial absorbers using the least-square method for wide incidence angle insensitivity. Applied optics 56.16 (2017): 4670-4674.

[86] D. Singh, A. Kumar, S. Meena, and V. Agarwala, "Analysis of frequency selective surfaces for radar absorbing materials," Prog. In Electromagn. Res. 38, 297–314 (2012).

[87] F. Costa, S. Genovesi, A. Monorchio, and G. Manara, "A circuit-based model for the interpretation of perfect metamaterial absorbers," IEEE Transactions on Antennas Propag. 61, 1201–1209 (2013).

[88] 25. R. J. Langley and E. A. Parker, "Equivalent circuit model for arrays of square loops," Electron. Lett. 18, 294–296 (1982).

[89] X. Chen, T. M. Grzegorczyk, B.-I. Wu, J. Pacheco Jr, and J. A. Kong, "Robust method to retrieve the constitutive effective parameters of metamaterials," Phys. Rev. E 70, 016608 (2004).

[90] Jiang, Wen, Yu Xue, and Shu-Xi Gong. "Polarization conversion metasurface for broadband radar cross section reduction." Progress In Electromagnetics Research 62 (2016): 9-15.

[91] Hakla, N., S. Ghosh, and K. V. Srivastava. "Design of low-profile broadband capacitive circuit absorber." Electronics Letters 52.22 (2016): 1825-1826.

[92] Ramkumar, Madhu A., and Chandrika Sudhendra. "Novel Ultra Wide Band Polarisation Independent Capacitive Jaumann Radar Absorber." Defence Science Journal 68.1 (2018).

[93] Han, Ye, and Wenquan Che. "Low-profile broadband absorbers based on capacitive surfaces." IEEE Antennas and Wireless Propagation Letters 16 (2017): 74-78.

[94] Kim, Y. J., Hwang, J. S., Khuyen, B. X., Tung, B. S., Kim, K. W., Rhee, J. Y., ... & Lee, Y. (2018). Flexible ultrathin metamaterial absorber for wide frequency band, based on conductive fibers. Science and Technology of Advanced Materials.

[95] Grant, J., Ma, Y., Saha, S., Khalid, A., & Cumming, D. R. (2011). Polarization insensitive, broadband terahertz metamaterial absorber. Optics letters, 36(17), 3476-3478.

[96] Jing, L., Wang, Z., Yang, Y., Zheng, B., Liu, Y., & Chen, H. (2017). Chiral metamirrors for broadband spin-selective absorption. Applied Physics Letters, 110(23), 231103.

[97] Chakravarty, S., Mittra, R., & Williams, N. R. (2002). Application of a microgenetic algorithm (MGA) to the design of broadband microwave absorbers using multiple frequency selective surface screens buried in dielectrics. IEEE Transactions on antennas and propagation, 50(3), 284-296.

[98] Ghosh, S., Bhattacharyya, S., & Srivastava, K. V. (2016). Design, characterisation and fabrication of a broadband polarisation-insensitive multi-layer circuit analogue absorber. IET Microwaves, Antennas & Propagation, 10(8), 850-855.

[99] Cong, L. L., Cao, X. Y., Song, T., Gao, J., & Lan, J. X. (2018). Angular-and Polarization-insensitive Ultrathin Double-layered Metamaterial Absorber for Ultra-wideband Application. Scientific reports, 8(1), 9627.

[100] Chen, H., Wang, Z., Zhang, R., Wang, H., Lin, S., Yu, F., & Moser, H. O. (2014). A meta-substrate to enhance the bandwidth of metamaterials. Scientific reports, 4, 5264.

[101] Schurig, D., Mock, J. J., Justice, B. J., Cummer, S. A., Pendry, J. B., Starr, A. F., Smith, D. R. (2006). Metamaterial electromagnetic cloak at microwave frequencies. Science, 314(5801), 977-980.

[102] Valentine, J., Li, J., Zentgraf, T., Bartal, G., Zhang, X. (2009). An optical cloak made of dielectrics. Nature materials, 8(7), 568.

[103] Chen, H., Wu, B. I., Zhang, B., Kong, J. A. (2007). Electromagnetic wave interactions with a metamaterial cloak. Physical Review Letters, 99(6), 063903.

[104] Alitalo, P., Tretyakov, S. (2009). Electromagnetic cloaking with metamaterials. Materials today, 12(3), 22-29.

[105] Alitalo, P., Tretyakov, S. A. (2011). Broadband electromagnetic cloaking realized with transmission-line and waveguiding structures. Proceedings of the IEEE, 99(10), 1646-1659.

[106] Tretyakov, S., Alitalo, P., Luukkonen, O., Simovski, C. (2009). Broadband electromagnetic cloaking of long cylindrical objects. Physical review letters, 103(10), 103905.

[107] Francesco Monticone and Andrea Alù, "Invisibility exposed: physical bounds on passive cloaking," Optica 3, 718-724 (2016)

[108] Sounas, D. L., Fleury, R., Alù, A. (2015). Unidirectional cloaking based on metasurfaces with balanced loss and gain. Physical Review Applied, 4(1), 014005.

[109] Selvanayagam, M., Eleftheriades, G. V. (2013). Experimental demonstration of active electromagnetic cloaking. Physical review X, 3(4), 041011.

[110] Long, C., Yin, S., Wang, W., Li, W., Zhu, J., & Guan, J. (2016). Broadening the absorption bandwidth of metamaterial absorbers by transverse magnetic harmonics of 210 mode. Scientific reports, 6, 21431.

[111] Sood, D., & Tripathi, C. C. (2015). A wideband ultrathin low profile metamaterial microwave absorber. Microwave and Optical Technology Letters, 57(12), 2723-2728.

[112] Sood, D., & Tripathi, C. C. (2015). A wideband wide-angle ultra-thin metamaterial microwave absorber. Progress In Electromagnetics Research, 44, 39-46.

[113] Ling, X., Xiao, Z., Zheng, X., Tang, J., & Xu, K. (2016). Ultra-broadband metamaterial absorber based on the structure of resistive films. Journal of ElEctromagnEtic WavEs and applications, 30(17), 2325-2333.

[114] Yang, Z., Luo, F., Zhou, W., Jia, H., & Zhu, D. (2017). Design of a thin and broadband microwave absorber using double layer frequency selective surface. Journal of Alloys and Compounds, 699, 534-539.